

Synthesis of Polymerized C₆₀ Bulk and Film in Three Dimensions by Irradiating Free-Electron Laser

Nobuyuki IWATA, Shingo ANDO, Ryo NOKARIYA, and Hiroshi YAMAMOTO

Department of Electronics and Computer Science, College of Science and Technology, Nihon University,
7-24-1 Narashinodai, Funabashi, Chiba 274-8501, Japan

(Received April 16, 2007; revised July 14, 2007; accepted July 31, 2007; published online February 15, 2008)

Pressed C₆₀ powder was polymerized with free-electron laser (FEL) irradiation. Brightened grains were synthesized in part at the sample surface, the Raman spectrum of which indicated the polymerization. It was noted that polymerization occurred as a result of irradiating a third harmonic FEL at 500 nm with an extremely low energy density of 2.6 μJ/(pulse·cm²). The polymerization is considered to be due to the micropulse width less than one ps forming the 20 μs macropulse of the FEL. Irradiating FEL during film growth, at 200 °C in particular, promoted the polymerization, as demonstrated by the Raman spectrum. The X-ray diffraction showed an oriented hcp structure with the relationship that the [0001] direction of the film was normal to the surface. However, Bragg reflection peaks did not shift in the film grown with FEL irradiation. These results indicate that the polymerized structure is a two-dimensional (2D) rhombohedron in the film plane. We expect that the (0001) surface of the oriented film will be suitable for a 2D polymerized rhombohedron and that migration energy will contribute to polymerization at an elevated temperature. [DOI: 10.1143/JJAP.47.1412]

KEYWORDS: C₆₀, free-electron laser, FEL, polymerization, Ag(2) mode, Raman spectrum, rhombohedral structure

1. Introduction

Polymerization processes for C₆₀ molecules have been developed for photo-, electron-beam-, pressure-, and plasma-induced methods. Among them, a crystalline three-dimensional (3D) C₆₀ polymer can be obtained at 15 GPa and approximately 650 °C from a two-dimensional (2D) polymer; however, the 2D polymer remains in part and includes a graphite like amorphous phase.¹⁾ The aim of our study is to develop a novel photopolymerization process for C₆₀ molecules and synthesize an amorphous 3D C₆₀ polymer on the bulk scale for various applications. We expect the features of the polymer to be a hardness level higher than that of diamond, flexibility, and lightness.²⁾ We chose a free-electron laser (FEL) as a light source, which has unique features: a tunable wavelength in the infrared range, and a 20 μs macropulse containing several hundred micropulses with a pulse width less than 1 ps.³⁾ The FEL was generated at the Laboratory for Electron Beam Research and Application (LEBRA) Institute of Quantum Science, Nihon University. In previous reports, the wavelength dependence of polymerization degree was discussed for a pressed C₆₀ powder, in which a 450–500 nm wavelength is most efficient for polymerization.^{4,5)} However, the polymerization takes place at the sample surface owing to the absorption. In this report, because the FEL was irradiated onto the pressed C₆₀ powder surface directly, apparently polymerized grains were visible in optical microscopy. In addition, films were deposited with FEL irradiation during growth to achieve bulk polymerization. Interestingly, polymerized films were observed.

2. Experimental Procedure

C₆₀ powder was pressed at 600 MPa in a vacuum, *ca.* 10⁻⁶ Torr. The pressed C₆₀ powder, called the bulk sample, was removed, immediately set on a tungsten heater, and annealed at 130 °C for 30 min in a vacuum. In Table I, the sample names and preparation conditions are summarized. The FEL with a frequency of 2 Hz was irradiated onto the bulk sample surface through a quartz window after annealing without exposure to air. Normally, the FEL includes

Table I. Sample names and experimental conditions for synthesizing bulk materials.

	Wavelength of irradiated FEL (nm)	Irradiation time (h)	Energy density [mJ/(pulse·cm ²)]
Sample.B0	As-pressed	—	—
Sample.B1	500	1	6.8
Sample.B2	500	2	8.4
Sample.B3	500	4	10
Sample.B4	500	4	578

Table II. Sample names and experimental conditions for thin films.

	Substrate temperature (°C)	Wavelength of irradiated FEL (nm)	Energy density [mJ/(pulse·cm ²)]
Sample.F1	40	—	—
Sample.F2	40	1350	4.36
Sample.F3	200	—	—
Sample.F4	200	1350	4.18

harmonics; therefore, only the third harmonic at 500 nm was obtained through a band-pass filter. The energy densities listed in the table are of the fundamental wave, not of harmonics. In sample.B4, the FEL energy density was increased with a condenser lens. The energy density of the third harmonics was less than 2.6 μJ/(pulse·cm²) owing to the lower limitation of the power meter.

In Table II, the growth conditions of C₆₀ films are summarized. C₆₀ powder was evaporated onto a cleaved mica substrate, which was attached to a Cu foil to maintain a thermal equivalent on the substrate surface. Film growth was carried out for 30 min with the FEL irradiation perpendicular to the substrate surface at *ca.* 10⁻⁷ Torr. The irradiated 1350 nm FEL includes a third harmonic at 450 nm. It is noted that no significant difference has been observed when irradiating pressed C₆₀ specimens with a fundamental FEL including harmonics and with only the third harmonic.⁶⁾

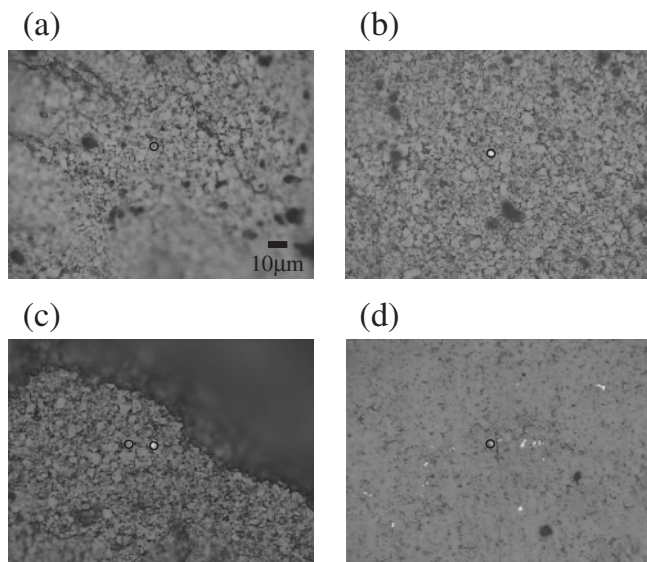


Fig. 1. Optical microscopy images of (a) sample_B0, as-pressed specimen; (b) sample_B1, 500 nm FEL irradiation for 1 h; (c) sample_B3, irradiation for 4 h; (d) sample_B4, 500 nm condensed FEL irradiation for 4 h. A scale bar is shown in the bottom right of (a). The circle in each image is the area used for micro-Raman experiments. Polymerized white grains can clearly be seen in (b)–(d).

All the specimens were evaluated using micro-Raman scattering (Kaiser HoloLab5000R Modular Research Microprobe System) and a second harmonic excitation yttrium aluminum garnet (YAG) laser, 532 nm. The image of the area for micro-Raman analysis was obtained using an optical microscope. The excitation power was from 0.18 to 0.40 mW to prevent polymerization. The surface of films was investigated by scanning probe microscopy (SII SPI3800N-SPA400) in a dynamic force microscope (DFM) mode, and X-ray diffraction (XRD; Rigaku RAD-C) analysis was carried out.

3. Results and Discussion

Optical microscopy images of the pressed C_{60} powder are shown in Figs. 1(a) sample_B0, 1(b) sample_B1, 1(c) sample_B4, and 1(d) sample_B5. The area indicated by a circle in the figures is for detecting the micro-Raman spectrum. All of the surfaces were packed with the tens-of- μm grains. After irradiating the FEL, as shown in Figs. 1(b)–1(d), white grains of approximately $5\ \mu\text{m}\phi$ appeared. The white grains brightened as a result of reflecting the light of the optical microscope. The white grain density increased as the energy density of the FEL increased, as shown in Fig. 1(d). Figure 2 shows the Raman spectra of sample_B3 detected from the white grains (solid line) and another area approximately $12\ \mu\text{m}$ away from the white grain (dotted line), indicated by the circles in Fig. 1(c). Intensity is normalized with the peak of an Ag(2) vibrational mode. In addition to the intrinsic Ag(2) mode, Raman spectrum detected from the white grain showed softened Ag(2)-derived modes typically at 1460 , 1454 , and $1447\ \text{cm}^{-1}$, indicated by arrows. The asymmetric peak at approximately $1470\ \text{cm}^{-1}$ in the dotted line was the sum of the peaks at 1470 and $1464\ \text{cm}^{-1}$. The Raman spectrum-like dotted line in Fig. 2, showing a tail toward the low-energy

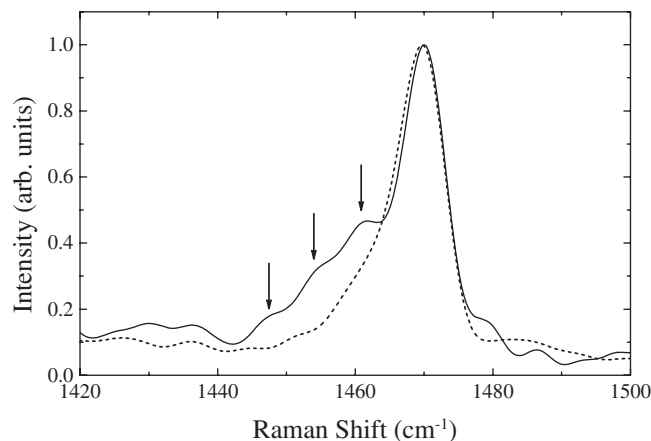


Fig. 2. The Raman spectra of sample_B3 are shown. The spectra of the solid and dotted lines, respectively, were detected at the white area and *ca.* $12\ \mu\text{m}$ away from the area in Fig. 1(c). In the solid line, in addition to the intrinsic Ag(2) mode, typical peaks at 1460 , 1454 , and $1447\ \text{cm}^{-1}$ appeared. In the dotted line, a tail toward a lower wavenumber was observed.

side, was observed for all of the surfaces except for the white grain. In both specimens, the intrinsic Ag(2) mode remained.

Irradiating the FEL resulted in the formation of C_{60} polymers, demonstrated by the appearance of additional peaks at 1460 , 1454 , and $1447\ \text{cm}^{-1}$, in particular in the white grains. The peaks at 1460 and $1454\ \text{cm}^{-1}$ are typical peaks for photopolymers and the peak at $1447\ \text{cm}^{-1}$ is observed in photopolymers and rhombohedral-type polymers.⁷⁾ However, the polymerization took place around the sample surface owing to the remnant of the intrinsic Ag(2) peak at approximately $1470\ \text{cm}^{-1}$. The penetration depth of the FEL was expected to be shallower than that of the excitation laser in the Raman experiment.

In Fig. 3 all the Raman spectra are shown. The excitation laser energy was calibrated to be $1467\ \text{cm}^{-1}$ for the Ag(2) mode using the as-pressed bulk specimen. A symmetric Ag(2) mode peak was observed in an as-pressed specimen, (a) sample_B0. The Raman spectra illustrated in Figs. 3(b)–3(e) were all obtained from the white grains found in Figs. 1(b)–1(d). As shown in Fig. 3(b), sample_B1, and Fig. 3(c), sample_B2, different Raman spectra were observed, even though the spectra were detected for similar white grains. Reproducibility was not confirmed. By increasing irradiation time and/or energy density, the same Raman spectrum with a typical photopolymerized peak at $1460\ \text{cm}^{-1}$ was obtained at all white grains, indicated by the dotted line.

Figure 4 shows the XRD spectra of sample_B0 (dotted line) and sample_B3 (solid line). Apparently all the Bragg reflections shifted toward a value higher than 2θ in sample_B3 compared with those of sample_B0, indicating the compression of lattice spacing.

From the results mentioned above, polymerization took place at the sample surface, particularly at the white grains. Polymerization was promoted by increasing irradiation time and energy density. In general, photopolymerization occurs at a moderate optical flux higher than $5\ \text{W}/\text{cm}^2$ and the degree of polymerization depends on the irradiation time on

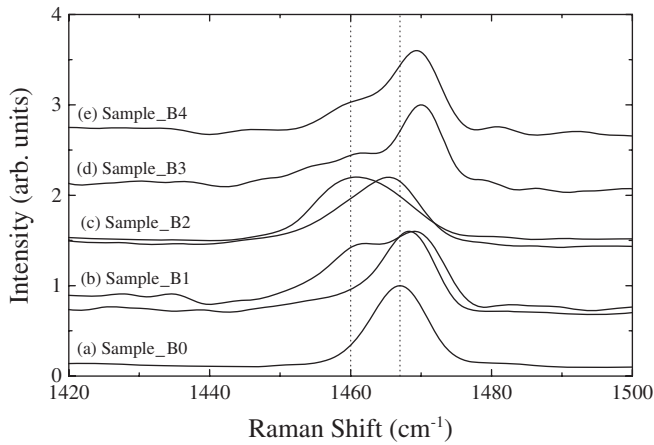


Fig. 3. The Raman spectra of all the specimens are shown. In (b), sample_B1, and (c), sample_B2, although the spectra were detected from similar white grains, reproducibility was not obtained. In (d), sample_B3, and (e), sample_B4, at all white grains, the same Raman spectrum was observed with the additional peak at 1460 cm^{-1} , which is typical for C_{60} photopolymers.

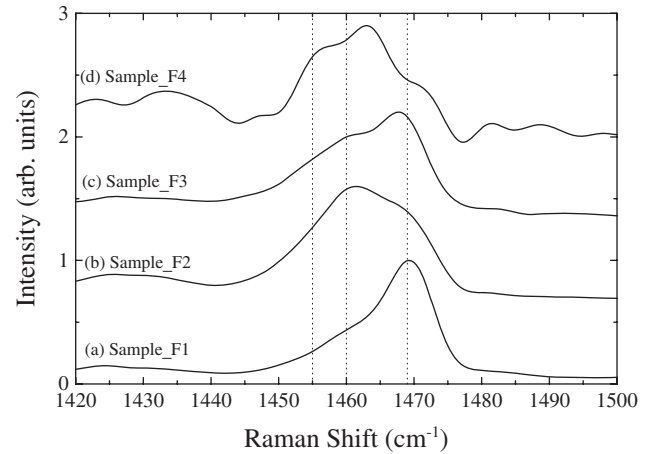


Fig. 5. Raman spectra of C_{60} films grown at (a) 40°C , sample_F1; (b) 40°C with 1350 nm FEL irradiation during growth, sample_F2; (c) 200°C , sample_F3; and (d) 200°C with 1350 nm FEL, sample_F4. Even at the low substrate temperature, the peak at 1460 cm^{-1} appeared in (a). As-growing films with the FEL irradiation polymerization phase were dominant in (b) and (d). At 200°C with 1350 nm FEL irradiation, a peak at 1455 cm^{-1} can clearly be seen.

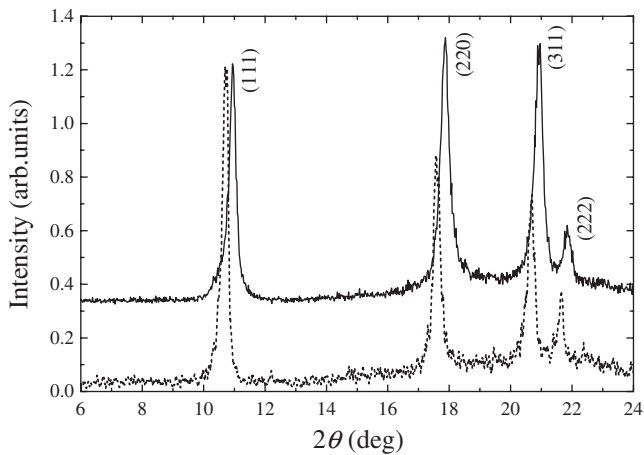


Fig. 4. The XRD results of sample_B0 (dotted line) and sample_B3 (solid line) are shown. Bragg reflections for the fcc structure can clearly be observed and indexed. With FEL irradiation, it was found that the specimen was compressed.

the order of hundreds of hours.⁷⁻⁹ Considering the macropulse width ($20\mu\text{s}$) of the FEL, the third FEL harmonic is 0.13 W/cm^2 at most. It is expected that one of the features of FEL, namely, the extremely small micropulse width, prevents the laser power from diffusing to the underlayer as phonons. Therefore, the power concentrates and is used to promote a phototransformation. In addition, all the areas, except for the white one, showed a tail toward the lower wavenumber in Fig. 2 (dotted line), which indicate that the areas act as a precursor to white grains.

In Fig. 5, the Raman spectra of the films are shown. The excitation energy was calibrated to be 1469 cm^{-1} for the intrinsic $\text{Ag}(2)$ mode. At 40°C , for (a) sample_F1, an additional peak at approximately 1460 cm^{-1} appeared. Because a thin film was deposited with FEL irradiation at 40°C for (b) sample_F2, the peak value at 1460 cm^{-1} became higher than that of the original $\text{Ag}(2)$ peak, which seldom occurs in bulk samples. At 200°C , for (c) sample_F3, peaks at not only 1460 cm^{-1} but also 1455 cm^{-1} appeared.

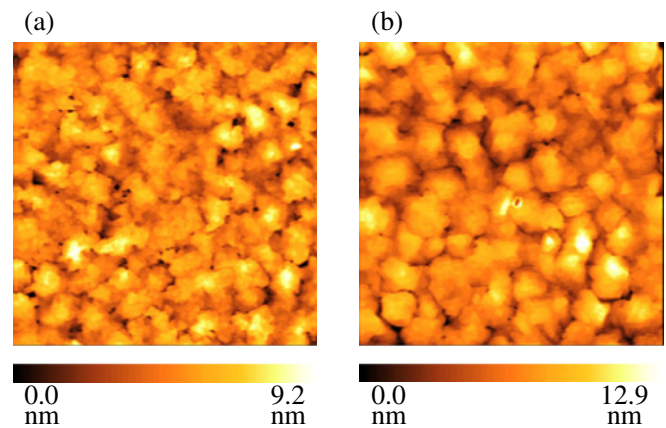


Fig. 6. (Color online) Surface images of (a) sample_F3 and (b) sample_F4 are shown. Although the number of nucleation sites was the same, the grain height in (b) was higher than that in (a), giving rise to a rougher surface. FEL irradiation is expected to enhance the polymerization, and, as a result, the migration length in the film (b) became shorter than that in (a). In (a), the surface showed the presence of grains on a flat surface, which was composed of coalesced grains, whereas in (b), grain boundaries can clearly be observed.

With FEL irradiation at 200°C for (d) sample_F4, the dominant peak was not 1469 cm^{-1} and a robust downshift was observed at approximately 1455 cm^{-1} .

Figure 6 shows the $5\mu\text{m}^2$ surface images of the films grown at 200°C (a) without FEL irradiation and (b) with irradiation. Steps and a terrace structure can clearly be seen in Fig. 6(a) with facets. The shapes of the grains were triangular and/or hexagonal. Grains growing around the nucleation site, the density of which was *ca.* $400 \times 400\ \mu\text{m}^{-2}$, coalesced with adjacent grains and then became a flat surface with an average surface roughness (R_a) of 1.03 nm . With irradiation in Fig. 6(b) for sample_F4, the density of the nucleation site was almost the same, but coalescence did not occur to a large extent compared with that in the case of sample_F3, giving rise to a larger grain height and rougher

surface with an R_a of 1.59 nm. Grain boundaries were clearly observed. The FEL-irradiated film surface is approximately the same as that of a film grown at an *ca.* 50° lower substrate temperature without FEL irradiation.¹⁰ The XRD spectrum of the film grown at 200 °C showed (000n) ($n = 2, 4, 6$) Bragg reflections and the result indicated a hexagonal closed packed (hcp) structure, which was the same as that shown in a previous report.¹⁰ The [0001] direction was normal to the substrate surface. However, no peak shift was observed in the film with FEL irradiation, indicating that polymerization did not occur along the direction normal to the surface.

The Raman spectra showed the polymerization, whereas the XRD result did not, in the film. A plausible interpretation of this inconsistency is the synthesis of 2D rhombohedral polymerization in the film plane at 200 °C. As shown in Figs. 5 and 6, elevated substrate temperature and FEL irradiation promoted the polymerization. By increasing the substrate temperature, the oriented film with the hcp structure showed the (0001) plane on the film surface during growth. In high-temperature high-pressure (HTHP) synthesis processes for polymers, rhombohedral (R), tetragonal (T), and orthorhombic (O) polymerized phases are reported.⁷ The (0001) surface is expected to be suitable for the synthesis of a R polymerized phase owing to the packing structure of C₆₀ molecules. Considering the results of polymerization in the film grown at 40 and 200 °C without FEL irradiation and that growth was promoted at 200 °C, as shown in Figs. 5(a) and 5(c), it is reasonable to conclude that migration energy contributes to polymerization. When the migrating molecules incorporate in a kink or a step, the migration energy is expected to transfer to the energy for polymerization. Polymerized molecules were not easily released and showed limited migration; consequently, the surface became rough. From the results of the Raman spectra, polymerization was promoted in the film by irradiating the FEL during growth.

4. Conclusions

We propose a novel photopolymerization process with the FEL irradiation of pressed C₆₀ powder and films to synthesize 3D amorphous C₆₀ polymers for application to a novel hard, light, and tough material. White grains in optical microscopy showed the polymerized Raman spec-

trum with additional peaks at 1460, 1454, and 1447 cm⁻¹. Reproducibility for the grains was improved by increasing the irradiation time, and the white-grain density was increased with condensed FEL irradiation. The mechanism of the polymerization with low power FEL irradiation is considered to be an extremely sharp micropulse. As irradiating the FEL during film growth caused downshifting, the Ag(2)-derived mode became dominant, in particular, when grown at 200 °C. No changes in Bragg reflections along the perpendicular to the surface exhibited nonpolymerization along the direction. The expected polymer structure was a 2D rhombohedron in the plane. The peak appearance at 1455 cm⁻¹ in the film grown at 200 °C with FEL irradiation was lower than the typical photopolymer peak at 1460 cm⁻¹, indicating the strong correlation between adjacent C₆₀ molecules in the plane.

Acknowledgments

This work was partially supported by the “Academic Frontier” Project for Private Universities: matching fund subsidy from Ministry of Education, Culture, Sports, Science and Technology (MEXT), 2000–2007. The authors are grateful for the financial support of an Interdisciplinary General Joint Research Grant (Nihon University).

- 1) S. Yamanaka and A. Syouji: *Kotai Butsuri* **41** (2006) 407 [in Japanese].
- 2) V. Blank, M. Popov, G. Pivovarov, N. Lovova, K. Gogolinsky, and V. Reshetov: *Diamond Relat. Mater.* **7** (1998) 427.
- 3) Y. Hayakawa, I. Sato, K. Hayakawa, T. Tanaka, K. Yokoyama, K. Kanno, T. Sakai, K. Ishiwata, K. Nakao, and E. Hashimoto: *Nucl. Instrum. Methods Phys. Res., Sect. A* **507** (2003) 404.
- 4) H. Yamamoto, N. Iwata, R. Hashimoto, and S. Ando: *Appl. Surf. Sci.* **253** (2007) 7977.
- 5) S. Ando, R. Nokariya, R. Koyaizu, N. Iwata, and H. Yamamoto: to be published in *Trans. Mater. Res. Soc. Jpn.* (2007).
- 6) N. Iwata and H. Yamamoto: private communication.
- 7) P. C. Eklund and A. M. Rao eds.: *Fullerene Polymers and Fullerene Polymer Composites* (Springer, Berlin, 1999) Chaps. 1 and 4.
- 8) A. M. Rao, P. Zhou, K.-A. Wang, G. T. Hager, J. M. Holden, Y. Wang, W. T. Lee, X.-X. Bi, P. C. Eklund, D. S. Cornett, M. A. Duncan, and I. J. Amster: *Science* **259** (1993) 955.
- 9) J. Onoe and K. Takeuchi: *Phys. Rev. Lett.* **79** (1997) 2987.
- 10) N. Iwata, A. Kinjo, H. Okuyama, and H. Yamamoto: *Jpn. J. Appl. Phys.* **44** (2005) 617.

Photon-assisted synthesis of C₆₀ polymers by laser irradiation

Hiroshi Yamamoto^{*}, Nobuyuki Iwata, Ryoji Hashimoto, Shingo Ando

College of Science and Technology, Nihon University, 7-24-1 Narashinodai, Funabashi-shi, Chiba 274-8501, Japan

Available online 2 March 2007

Abstract

The harmonics of a free electron laser (FEL) were irradiated in vacuum to surfaces of compressed C₆₀ and a mixture of C₆₀ and I₂. The power and frequency of the fundamental FEL macro-pulse were *ca.* 0.5 mJ/pulse and 2 Hz, respectively. The irradiation time was 120–180 min. After irradiation of FEL with a typical wavelength of 450 or 345 nm, the Raman peak of Ag(2)-derived vibration mode of C₆₀ shifted to the lower-energy side. The Raman peak shift of the mixture powder sample was greater than that of pure C₆₀. Furthermore, changes of the crystalline structure indicated that various intermolecular combinations occurred by irradiation. These results strongly suggest that three-dimensional polymerization of C₆₀ was promoted by laser irradiation and the effect of photon-assisted hole-doping from iodine atoms to C₆₀ molecules.

© 2007 Elsevier B.V. All rights reserved.

Keywords: C₆₀; Polymerization; Free electron laser (FEL); Hole-doping; Raman spectroscopy

1. Introduction

Since the polymerization of C₆₀ films was first accomplished using phototransformation [1], many studies have examined C₆₀ polymer synthesized using various excitation processes [2] such as electron-beam irradiation [3], high-pressure [4], plasma-induced excitation [5], and so on. Because of those adequate chemical or physical excitations, a carbon double bond in a hexagon of a C₆₀ cage is broken; it transforms into an intermolecular four-fold ring with a neighboring molecule. Consequently, two C₆₀ molecules are combined and change into a dimer or some higher order of polymer. This process is the fundamental mechanism for C₆₀ polymerization.

The polymerized fullerite structures based on a “2 + 2 cycloaddition” bonding [6] were observed experimentally and theoretically [7–9]. One-dimensional (1D) chains revealed an orthorhombic phase; two-dimensional (2D) planes include a tetragonal and a rhombohedral phase. Few experimental data [4] have been reported about the possibility of a three-dimensional (3D) polymerized phase, but 3D C₆₀ polymers are expected to be extremely hard, with lower density and less brittleness than diamond.

The polymerizations usually proceed by compression at the order of gigapascals or heating to greater than a thousand degrees [4]. The C₆₀ cages partially collapse under stringent pressure conditions. These polymerization processes are not well-controlled and are unsuitable to supply sufficiently large 3D C₆₀ polymers for applications.

This work is intended to develop a novel photon-assisted process for synthesis of C₆₀ polymers by laser irradiation under moderately high pressure. We have also described a *hole doping effect*, as demonstrated in the synthesis of diamond from graphite [10]. We expect that this effect is applicable to the polymerization reaction of C₆₀ molecules because of the mutually similar structures of carbon networks in graphite and C₆₀.

Hereinafter, the newly developed photon-assisted process is introduced and the possibility of synthesis of 3D C₆₀ polymers by free electron laser (FEL) irradiation will be demonstrated.

2. Experimental

Fig. 1 shows the schematic apparatus developed for synthesis of C₆₀ polymers. The vacuum chamber was evacuated to *ca.* 10⁻⁴ Pa using a turbo molecular pump. The pristine powder was set in an anvil placed in vacuum. The powder was compressed via a bellows using a hydraulic press. Before laser irradiation, the sample was pre-annealed at *ca.* 500 K for 20 h in a vacuum chamber. Pressure, usually *ca.* 470 MPa, was

^{*} Corresponding author. Tel.: +81 47 469 5457; fax: +81 47 469 5457.

E-mail address: hyama@ecs.est.nihon-u.ac.jp (H. Yamamoto).

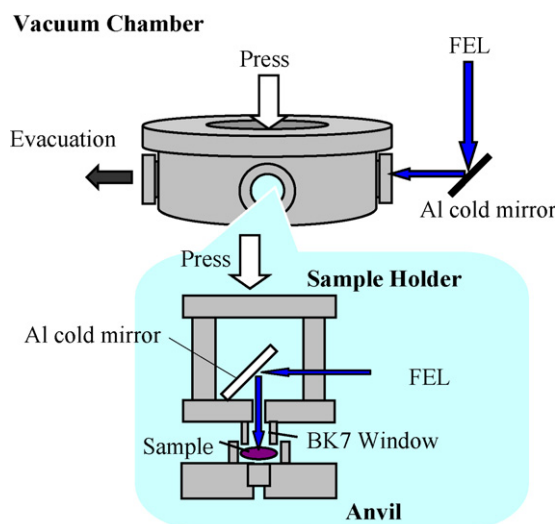


Fig. 1. Schematic apparatus constructed for synthesis of C_{60} polymers. The compressed surfaces of the sample were irradiated using a laser by the BK7 window. Aluminum cold mirrors were used for high reflectance of visible laser (wavelength less than *ca.* 700 nm) and for cutting near-infrared light. The quartz BK7 ensures high transmittance of greater than 95% of visible light.

applied to the sample powder using a quartz BK7 window. Visible laser light was introduced to the surface of the pressed sample using Al cold mirrors that reflect only light with wavelength of less than *ca.* 700 nm.

Since the 1980s, mid-infrared (wavelength of a few tens of micrometers) FELs have been developed and applied to numerous studies of laser-solid interaction [11]. We adopted an FEL system that generates a tunable near-infrared laser and higher harmonics. Details of the FEL system used there have appeared elsewhere [12]. A macro-pulse of a few tens of microseconds, which included micro-pulses of a few-hundred-picoseconds, constituted the FEL pulse, which was repeated in 2 Hz. The power of the fundamental macro-pulse was *ca.* 0.5 mJ/pulse. The irradiation time was typically 120–180 min. Because the FEL can supply a laser with a tunable wavelength, the fundamental wavelength was chosen arbitrarily for this work. The laser used for irradiation was the third harmonic of FEL with a fundamental wavelength of *ca.* 1350 nm. The wavelength that was mainly noticed was *ca.* 450 nm, of which the value was evaluated from the difference of the bonding energy of the C=C double bond and the C–C bond. Furthermore, an ultraviolet laser (345 nm) was also taken out as the fifth harmonic of *ca.* 1700 nm fundamental FEL.

Two kinds of pristine powder were prepared. Pure C_{60} (99.95%) was a commercial product. The C_{60} was also mixed with I_2 at the molar ratio of 1:4. Iodine was used for enhancement of polymerization reactions expected from the hole-doping effect. Because the electron affinity of the C_{60} is high, we aimed at promotion of electron transfer from C_{60} to iodine atoms, assisted by photon-excitation.

For a C_{60} molecule and its polymer, the optimized molecular structure and/or the molecular orbital was semi-empirically calculated using WinMOPAC (3.9 Professional; Fujitsu Co. Ltd.). Then molecular vibration modes were evaluated for investigation of the observed Raman spectra.

The obtained samples were 5-mm-diameter disks with thickness of less than 0.5 mm. They were packed in a vacuum box to prevent contamination from air. Raman microscopic spectroscopy (SYSTEM1000; Renishaw plc.) was used to study molecular vibration spectra. The light source used for excitation was a 514.5 nm Ar laser. Crystalline structures were studied using reflective X-ray diffraction (XRD) (RAD-C; Rigaku Corp.) with $Cu K\alpha_1$ X-rays.

3. Results and discussion

Our calculation of vibration modes indicated that the Raman spectrum broadened and shifted to a lower energy because of the polymerization reactions. A Raman Ag(2) mode of a C_{60} molecule is defined as a contracting vibration of pentagon rings. Fig. 2 shows results of schematic vibration analysis of the Ag(2)-derived mode in a C_{60} monomer, a 2 + 2 dimer, and a trimer. When a C_{60} molecule is combined with another molecule, the Ag(2) modes changed into other vibration modes because of lower symmetry or vibration reduction. The polymerization of the C_{60} monomer engendered the Raman peak shift of the Ag(2)-derived mode to the lower energy. Our calculations indicate that the amounts of the Raman peak shift obtained in the dimer and the trimer, as shown respectively in Fig. 2, were *ca.* 9 and 16 cm^{-1} , thereby confirming qualitatively that the Raman peak broadens and shifts to the lower-energy side according to the progress of polymerization. The Ag(2)-derived mode is therefore noted as an index of the polymerization reaction progress.

Fig. 3 shows typical Raman peaks of the Ag(2)-derived mode in the case of 450 nm FEL irradiation. The wave number of the peak of the non-irradiated pristine C_{60} was 1463 cm^{-1} , whereas that of the irradiated C_{60} changed to 1460 cm^{-1} with a

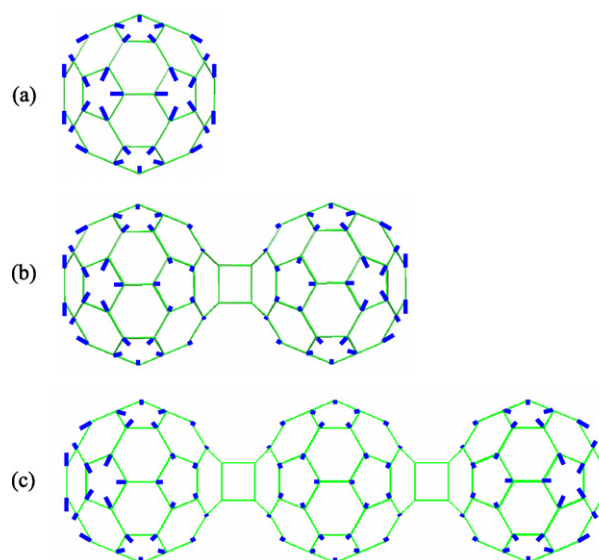


Fig. 2. Schematic molecular structures and Ag(2)-derived vibration modes calculated in: (a) a C_{60} monomer, (b) a dimer, and (c) a trimer. The dimer or trimer is formed by a “2 + 2” cycloaddition reaction between parallel carbon double bonds on two adjacent molecules. The amplitudes of the vibration of constituent C atoms are represented schematically as thick lines.

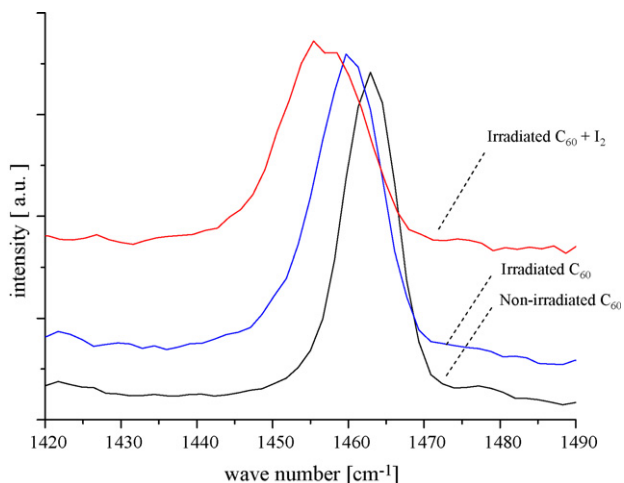


Fig. 3. Raman peaks of the Ag(2)-derived vibration modes observed in the three samples: non-irradiated pristine C_{60} , C_{60} , and $C_{60} + I_2$ irradiated by 450 nm FEL.

decrement by *ca.* 3 cm^{-1} . On the other hand, the irradiated mixture of $C_{60} + I_2$ revealed the peak wave number of 1455 cm^{-1} . The Raman shift was as great as *ca.* 8 cm^{-1} . The half-width of the Raman peak also increased in correspondence to the amount of the peak shift.

Nearly identical results were obtained for samples irradiated by FEL with various wavelengths of 400–500 nm. No distinct difference was observed in the Raman spectra, even by changing the wavelength.

However, the ultraviolet rays caused somewhat different changes of the Raman spectrum. Fig. 4 shows Raman peaks of the Ag(2)-derived mode in the case of 345 nm FEL irradiation. Double splitting of the peak by the irradiation was observed: C_{60} molecules are known to reveal large optical absorption at wavelengths of 221, 271, and 347 nm [13]. Because the optical density at 345 nm is about three times higher than that at 450 nm, polymerization reactions might proceed better in the thinner region of sample surfaces by 345 nm irradiation than by

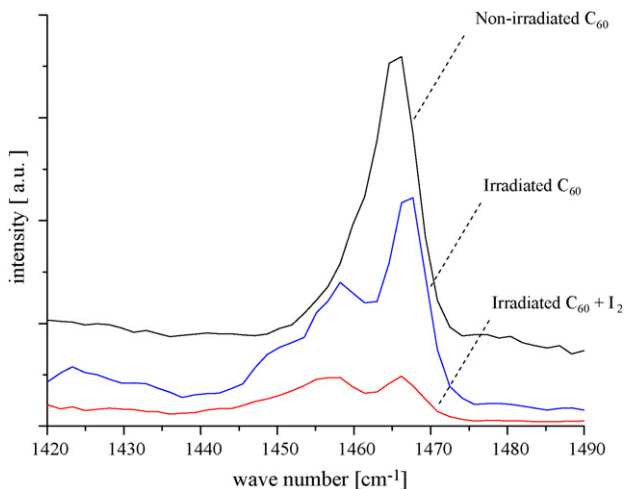


Fig. 4. Raman peaks of the Ag(2)-derived vibration modes observed in the three samples: non-irradiated pristine C_{60} , C_{60} , and $C_{60} + I_2$ irradiated by 345 nm FEL.

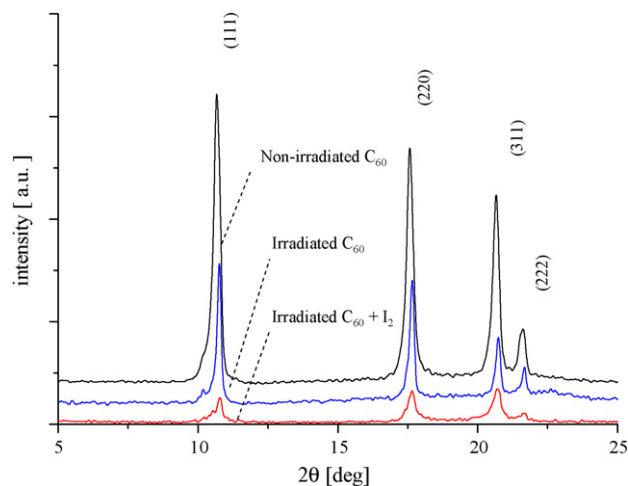


Fig. 5. XRD patterns of the three samples: non-irradiated pristine C_{60} , C_{60} , and $C_{60} + I_2$ irradiated by 450 nm FEL. The inset index corresponds to each fcc plane of C_{60} . The (1 1 1) peak intensity of the irradiated $C_{60} + I_2$ decreased remarkably.

450 nm irradiation. Consequently, the Raman peak of non-polymerized C_{60} also remained in the case of 345 nm irradiation. The spectrum shown in Fig. 4 revealed the splitting peak. The amounts of the Raman shift observed were *ca.* 7 cm^{-1} in the C_{60} sample and *ca.* 10 cm^{-1} in the $C_{60} + I_2$ sample. The peak decreased, broadened, and came to resemble that of 450-nm irradiation.

It is noteworthy that the change of the Raman peak of the $C_{60} + I_2$ sample was definitely larger than that of pure C_{60} . This result implies that some additional mechanisms work for promotion of polymerization by addition of I_2 . It can be inferred that photo-excited electrons of C_{60} molecules transfer to iodine atoms: hole-doping into C_{60} molecules occurs.

The hole-doping effect was also confirmed through crystal-line structure analyses. Fig. 5 shows typical XRD patterns of samples irradiated using 450 nm FEL. The *d* values of (1 1 1) planes of the irradiated C_{60} and $C_{60} + I_2$ sample were smaller by $7 \times 10^{-3} \text{ nm}$ and $8 \times 10^{-3} \text{ nm}$, respectively, than that of the non-irradiated C_{60} . The decrement of the lattice parameter was about 1%. Furthermore, the main peak (1 1 1) markedly decreased and broadened in the case of the $C_{60} + I_2$ sample. That result suggests that binding between C_{60} molecules took place and that the decline of the crystalline structure progressed according to polymerization reactions induced by FEL irradiation and/or addition of iodine.

4. Conclusion

The FEL, usually of 450 or 345 nm wavelength, was irradiated to surfaces of compressed C_{60} or $C_{60} + I_2$ powder in vacuum. Simulation of molecular vibration modes revealed that the Raman peak of the Ag(2)-derived mode shifts to the lower-energy side and/or the half-width of the peak broadens concomitant with progress of the polymerization reaction. A mixture sample $C_{60} + I_2$ irradiated by 450 nm FEL showed a Raman shift of *ca.* 8 cm^{-1} , of which the value was distinctly larger than that of the pure C_{60} sample. The XRD results revealed that the average distance between C_{60} molecules

shortened by about 1% and the crystalline structure was degraded by the FEL irradiation. The obtained results suggest that 3D polymerization of C₆₀ was promoted using laser irradiation and/or the effect of the photon-assisted hole-doping from iodine to C₆₀ molecules. Detailed characterization of the obtained samples is a subject for future work.

Acknowledgements

This work was partly supported by the “Academic Frontier” Project for Private Universities: a matching fund subsidy from MEXT, 2000–2004. The authors would like to thank the staff of Laboratory for Electron Beam Research and Application of Nihon University for assistance with FEL operations.

References

- [1] A.M. Rao, P. Zhou, K.-A. Wang, G.T. Hager, J.M. Holden, Y. Wang, W.-T. Lee, X.-X. Bi, P.C. Eklund, D.S. Cornett, M.A. Duncan, I.J. Amster, *Science* 259 (1993) 955.
- [2] M.S. Dresselhaus, G. Dresselhaus, P.C. Eklund, *Science of Fullerenes and Carbon Nanotubes*, Academic Press Inc., San Diego, 1996, p. 209.
- [3] Y.B. Zhao, D.M. Poirier, R.J. Pechman, J.H. Weaver, *Appl. Phys. Lett.* 64 (1994) 577.
- [4] H. Yamawaki, M. Yoshida, Y. Kakudate, S. Usuba, H. Yokoi, S. Fujiwara, K. Aoki, R. Ruoff, R. Malhotra, D.C. Lorents, *J. Phys. Chem.* 97 (1993) 11161.
- [5] N. Takahashi, H. Dock, N. Matsuzawa, M. Ata, *J. Appl. Phys.* 74 (1993) 5790.
- [6] A.M. Rao, P. Zhou, K.-A. Wang, G.T. Hager, J.M. Holden, Y. Wang, W.T. Lee, X.-X. Bi, P.C. Eklund, D.S. Cornett, M.A. Duncan, I.J. Amster, *Science* 259 (1993) 955.
- [7] A.M. Rao, P.C. Eklund, J.-L. Hodeau, L. Marques, M. Nunez-Regueiro, *Phys. Rev. B* 55 (1997) 4766.
- [8] V.A. Davydov, L.S. Kashevarova, A.V. Rakhmanina, V. Agafonov, H. Allouchi, R. Ceorin, A.V. Dzyabchenko, V.M. Senyavin, H. Szwarc, *Phys. Rev. B* 58 (1998) 14786.
- [9] X. Chen, S. Yamanaka, K. Sako, Y. Inoue, M. Yasukawa, *Chem. Phys. Lett.* 356 (2002) 291.
- [10] H. Nakayama, H. Katayama, H. Yoshida, *Jpn. J. Appl. Phys.* 41 (2002) 817.
- [11] H.P. Freund, J.T.M. Antonsen, *Principles of Free-Electron Lasers*, Chapman & Hall, London, 1992.
- [12] Y. Hayakawa, I. Sato, K. Hayakawa, T. Tanaka, K. Yokoyama, T. Sakai, K. Kanno, K. Ishiwata, E. Hashimoto, *Nucl. Instrum. Methods A507* (2003) 404.
- [13] S. Kazaoui, R. Ross, N. Minami, *Solid State Commun.* 90 (1994) 623.

Crystal Growth of Magnetolectric Cr₂O₃ Thin Film on Sapphire and SrTiO₃

Takeshi ASADA, Kenjiro NAGASE, Nobuyuki IWATA, and Hiroshi YAMAMOTO

College of Science and Technology, Nihon University, Funabashi, Chiba 274-8501, Japan

(Received July 12, 2007; accepted September 18, 2007; published online January 22, 2008)

Representative magnetolectric (ME) material Cr₂O₃ films were prepared on *R*-cut sapphire (*R*-Al₂O₃) and SrTiO₃ (STO) substrates with the aim of applying them in perovskite oxide electronic devices. Cr₂O₃ thin films were deposited using the DC–RF hybrid magnetron sputtering system at different substrate temperatures. When the *R*-Al₂O₃ substrate temperature was 550 °C, Bragg peaks (*n*, \bar{n} , 0, 2*n*) were observed. The full width at half maximum (FWHM) of the rocking curve was smallest at *T*_s = 550 °C with a value of 0.52°. The grain size of Cr₂O₃ increased with substrate temperature in the 400–600 °C range. The lengths of rectangular Cr₂O₃ grains were in the ranges of 200–600 nm along the $[\bar{1}101]$ direction and 100–300 nm along the $[11\bar{2}0]$ direction. Furthermore, Cr₂O₃ films were deposited on SrTiO₃ (100) with CeO₂ buffer layers. The Cr₂O₃ thin film deposited on the smooth CeO₂ buffer layers with the average roughness (*R*_a) = 0.41 nm showed a *c*-axis orientation; moreover, a Cr₂O₃(0001)/CeO₂(100) // STO(100) crystal relationship was obtained. [DOI: 10.1143/JJAP.47.546]

KEYWORDS: magnetolectric effect, sputtering, Cr₂O₃, sapphire, CeO₂ buffer, SrTiO₃

1. Introduction

The magnetolectric (ME) effect is defined as the appearance of magnetic fields induced by electric fields. When electric fields are applied, the changes in the relative position between \pm ions result in changes in magnetic superexchange interactions and then magnetic fields appear outside.^{1–3} As a representative ME material, antiferromagnetic insulator Cr₂O₃ has been studied.⁴ Because magnetic fields are induced along the direction of electric fields applied, the ME coefficients are different in the directions of the *a*-, *b*-, and *c*-axes.^{1,3} The coefficient in the *c* direction is highest at room temperature as compared with those in the other axes. In contrast, the ME coefficient along the *a* direction is higher than that along the *c*-direction at a low temperature. Therefore, investigation of the crystal orientation of Cr₂O₃ is important for application of the ME effect.

We expected that ME materials can be applied to novel electronic devices, particularly in combination with a series of perovskite oxides showing various functional properties, such as superconductivity, ferroelectricity, and ferromagnetism. Most perovskite oxide films have been prepared on cubic perovskite crystal substrates as SrTiO₃ (STO). However, lattice matching is not good between cubic STO and rhombohedral Cr₂O₃. In order to combine Cr₂O₃ with a series of perovskite oxides devices, Cr₂O₃ films should be deposited on STO with cubic CeO₂ buffer layers.^{5–7} The purposes of this work are to optimize substrate temperature for sputtered Cr₂O₃ films on *R*-Al₂O₃ and to investigate film growth on STO with CeO₂ buffer layers.

2. Experimental Procedure

Cr₂O₃ films were deposited on *R*-Al₂O₃($\bar{1}102$) by off-axis DC–RF hybrid magnetron sputtering. Substrate temperature (*T*_s) was changed from 300 to 600 °C. Other typical growth conditions were DC current, RF power, and sputtering pressure of 0.04 A, 100 W, and 0.26 Pa (Ar : O₂ = 4 : 1), respectively.

As a substrate, a *R*-Al₂O₃ single crystal (5 × 10 mm²) was etched by HF (HF : H₂O = 1 : 7) for 10 s, and subsequently annealed at 1000 °C for 12 h in air.

Two samples (samples A and B) of Cr₂O₃/CeO₂ bilayers were deposited on the STO substrates by off-axis RF

magnetron sputtering. The sputtering conditions for CeO₂ buffer in sample A were *T*_s, RF power, and sputtering pressure of 700 °C, 80 W and 9 Pa (Ar : O₂ = 1 : 1), respectively. The sputtering conditions for CeO₂ in sample B were *T*_s, RF power, and sputtering pressure of 380 °C, 50 W, and 6 Pa (Ar : O₂ = 1 : 1), respectively. The CeO₂ // STO film of sample B was annealed at 1000 °C for 3 h in air. The surface average roughness (*R*_a) of CeO₂ buffer layers was investigated before the sputtering of Cr₂O₃ films.

The crystalline structures of the films were investigated by X-ray diffraction analysis (XRD; Rigaku RAD-C system) with the θ – 2θ scan and rocking curve at 2θ . The surface morphology was observed by scanning probe microscopy in the dynamic force microscopy (DFM) mode (Nanonavigation SPI3800N and SPA400 unit; Seiko Instruments).

3. Results and Discussion

3.1 Cr₂O₃ on *R*-Al₂O₃

The XRD pattern of Cr₂O₃/*R*-Al₂O₃ at *T*_s = 550 °C is shown in Fig. 1. The Cr₂O₃($\bar{1}102$) and Al₂O₃($\bar{1}102$) Bragg diffraction peaks were observed and the crystal relationship between Cr₂O₃ and Al₂O₃ was Cr₂O₃($\bar{1}102$) // Al₂O₃($\bar{1}102$). Similar XRD patterns were observed in the films prepared at *T*_s = 300–600 °C.

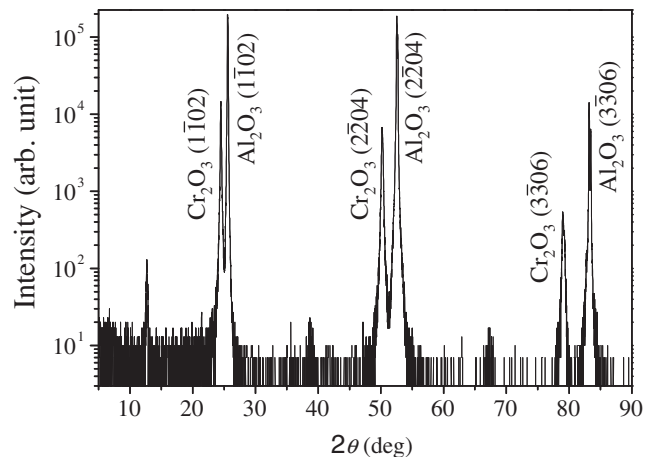


Fig. 1. XRD pattern of Cr₂O₃ deposited at *T*_s = 550 °C on *R*-Al₂O₃. The crystal relationship between Cr₂O₃ and *R*-Al₂O₃ was Cr₂O₃($\bar{1}102$) // Al₂O₃($\bar{1}102$).

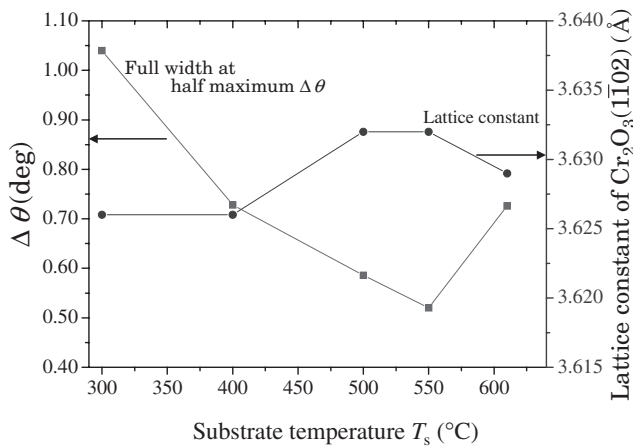


Fig. 2. T_s dependence of $\text{Cr}_2\text{O}_3[1\bar{1}02]$ lattice constant and $\Delta\theta$ (FWHM) of rocking curve at $\text{Cr}_2\text{O}_3(1102)$ reflection. The left-side index and the right-side index show FWHM of rocking curve reflection and lattice constant of $\text{Cr}_2\text{O}_3(10\bar{1}2)$ plane, respectively.

Figure 2 shows the T_s dependence of $\text{Cr}_2\text{O}_3(1\bar{1}02)$ lattice constant and full width at half maximum (FWHM) of rocking curve reflection ($\Delta\theta$). The lattice constant was almost constant from $T_s = 300$ to 400°C and lattice constant increased from $T_s = 400$ to 500°C . The value of $\Delta\theta$ decreased monotonically with increasing T_s from $T_s = 300^\circ\text{C}$. The smallest value was 0.52° at $T_s = 550^\circ\text{C}$.

The small value of $\Delta\theta$ at higher T_s indicates that high T_s induces crystal orientation along the normal direction for substrates. Crystal degradation might proceed at T_s above 550°C .

Two typical DFM images ($2 \times 2 \mu\text{m}^2$) of $R\text{-Al}_2\text{O}_3$ substrate surfaces are shown in Figs. 3(a) and 3(b). All the substrates showed a step and terrace structure. From the line profile shown in Figs. 3(a) and 3(b), the widths of each terrace were in the 180–200 nm range and 400 nm, respectively.

Figures 3(c)–3(f) show the $2 \times 2 \mu\text{m}^2$ DFM surface images and line profiles of $\text{Cr}_2\text{O}_3 // R\text{-Al}_2\text{O}_3$ deposited at $T_s = 300$ – 600°C . Table I shows grain size (along $[11\bar{2}0] \times$ along $[\bar{1}101]$) as a function of T_s . Figure 3(c) shows the film deposited at $T_s = 400^\circ\text{C}$ on the substrate shown in Fig. 3(a). Rectangular grains appeared with sizes in the $100 \times (100\text{--}200) \text{ nm}^2$ range. The difference in height between grains was approximately 3.5 nm, as determined from the line profile shown in Fig. 3(c). Figure 4(d) shows the film deposited at $T_s = 500^\circ\text{C}$ on the substrate shown in Fig. 3(b). The rectangular grains became larger along the $[11\bar{2}0]$ direction and coalesced. The lengths of grains were in the 200–300 nm range along the $[\bar{1}101]$ direction the same as the widths of substrate terraces shown in Fig. 3(b). On the other hand, the lengths of grains were in the 200–300 nm range along the $[11\bar{2}0]$ direction. Grain boundaries were observed and their lengths were longer along the $[11\bar{2}0]$

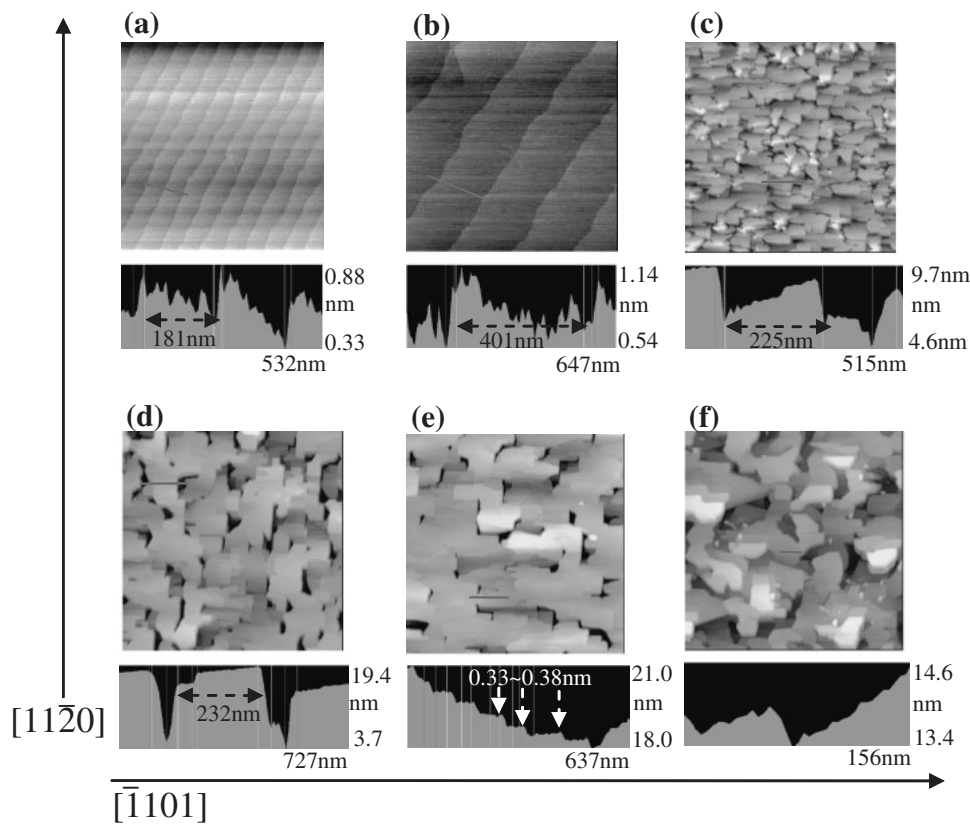


Fig. 3. DFM surface images ($2 \times 2 \mu\text{m}^2$) of $R\text{-Al}_2\text{O}_3$ substrates are shown in (a) and (b), as well as DFM surface images of Cr_2O_3 films deposited at (c) $T_s = 400^\circ\text{C}$, (d) $T_s = 500^\circ\text{C}$, (e) $T_s = 550^\circ\text{C}$, and (f) $T_s = 600^\circ\text{C}$. The figures below the surface images are line profiles. The arrows from the bottom to the top and the left to the right show $[11\bar{2}0]$ and $[\bar{1}101]$ crystal directions, respectively. The arrows in the line profile show the width of terrace, step height and/or grain length. The grain size of Cr_2O_3 increased with T_s in the 400 – 600°C range. The lengths of Cr_2O_3 grains were in the range of 200 – 600 nm along the $[\bar{1}101]$ direction and 100 – 300 nm along the $[11\bar{2}0]$ direction.

Table I. T_s depending on grain size.

T_s (°C)	Grain size (nm ²)
400	100 × ~200
500	~300 × ~300
550	~300 × ~600
600	~400 × ~400

direction. About 30 grain boundaries were observed in the DFM image of $2 \times 2 \mu\text{m}^2$. Figure 3(e) shows the film deposited at $T_s = 550^\circ\text{C}$ on the substrate shown in Fig. 3(b). The grains were clearly larger along the $[\bar{1}101]$ direction. The lengths of grains were in the 200–600 nm range along the $[\bar{1}101]$ direction. Namely, the grain size was larger than the width of terraces observed in Fig. 3(b). As shown in the line profile, several steps along the $[\bar{1}101]$ direction were observed in the one-grain plane. The step heights were in the 0.3–0.4 nm range, the same as that of 1/3 unit cell of Cr_2O_3 with the R -plane (about 0.363 nm). About 21 grain boundaries were observed in the DFM image of $2 \times 2 \mu\text{m}^2$. In the film grown at 600°C , grains of various sizes grew along the $[11\bar{2}0]$ and $[\bar{1}101]$ directions. The grain size was $400 \times 400 \text{ nm}^2$. Bunching steps, the height of which was approximately 5 nm, were observed, as shown in Fig. 3(f). The surface smoothness was degraded.

Grain size is expected to increase with T_s because surface energy is decreased by large islands with decreasing island boundaries and increasing migration length. The rectangular grain sizes at $T_s = 400\text{--}550^\circ\text{C}$ were restricted by steps and terraces of $R\text{-Al}_2\text{O}_3$ shown in the Figs. 3(a) and 3(b). Therefore, at $T_s = 400^\circ\text{C}$, coalescence did not occur and the surface was covered by many grains of 200–400 nm sizes the same as the width of terraces. At $T_s = 500^\circ\text{C}$, grain size along the $[11\bar{2}0]$ direction was increased owing to a large migration length. Therefore, coalescence occurred along the $[11\bar{2}0]$ direction. However, the length of grains along the $[\bar{1}101]$ direction was the same as the width of terraces (about 400 nm), as shown by the line profile in Fig. 3(b), because sputtered flux atoms were not able to move over the steps of $R\text{-Al}_2\text{O}_3$. At $T_s = 550^\circ\text{C}$, migration length increased and atoms moved over the steps of $R\text{-Al}_2\text{O}_3$. Therefore, larger grains along the $[11\bar{2}0]$ and $[\bar{1}101]$ directions were obtained. As a result, the density of grain boundaries decreased. At $T_s = 550^\circ\text{C}$, the terrace in one grain was composed of several steps of 1/3 unit cell at most, showing a two-dimensional island growth. At $T_s = 600^\circ\text{C}$ migration length along the $[11\bar{2}0]$ and $[\bar{1}101]$ directions became isotropic, because of sufficiently migration energy for moving over the steps. Therefore, grains of various sizes were observed at $T_s = 600^\circ\text{C}$.

The surface of the film prepared at $T_s = 550^\circ\text{C}$ was smooth and revealed a two-dimensional growth. The results of XRD analysis and AFM indicated that about $T_s = 550^\circ\text{C}$ was the optimum for obtaining the highest quality of a $\text{Cr}_2\text{O}_3(1\bar{1}02)$ crystal, and a large ME effect is expected.

3.2 Cr_2O_3 on STO with CeO_2 buffer

Figure 4 shows the XRD pattern of Cr_2O_3 on the STO substrate with two kinds of CeO_2 buffer layer (samples A

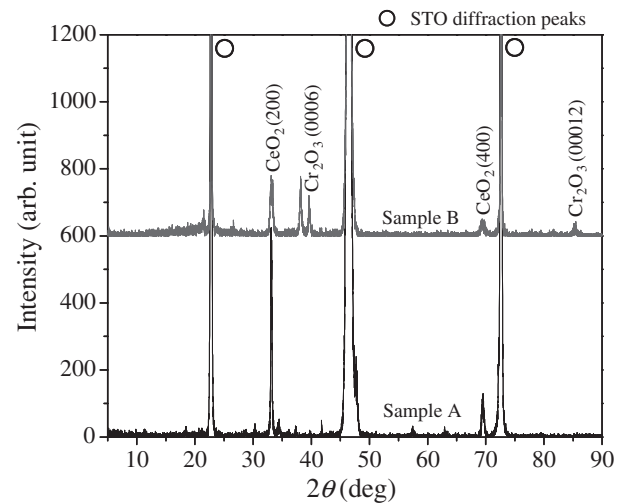


Fig. 4. XRD pattern of $\text{Cr}_2\text{O}_3/\text{CeO}_2 // \text{STO}$ bilayered samples A and B. Open circles indicate peaks from STO (100). Sample A did not show any diffraction peaks from Cr_2O_3 . Sample B revealed a trigonal c -axis Cr_2O_3 growth.

and B). Cr_2O_3 films were grown at $T_s = 550^\circ\text{C}$, at which a highly oriented film growth was obtained on $R\text{-Al}_2\text{O}_3$. No Bragg diffraction peak from Cr_2O_3 was observed for sample A. In contrast, sample B revealed a c -axis oriented growth and the crystal relationship was $\text{Cr}_2\text{O}_3(0001)/\text{CeO}_2(100) // \text{STO}(100)$.

The lattice constant of Cr_2O_3 is almost the same as that of Al_2O_3 . The lattice matching between CeO_2 and Al_2O_3 has been studied.^{5,6)} The lattice mismatches in $\text{CeO}_2(100)$ vs $\text{Al}_2\text{O}_3(11\bar{2}0)$ and $\text{CeO}_2(100)$ vs $\text{Al}_2\text{O}_3(0001)$ were approximately 24 and 8%. Namely, the mismatching of $\text{Cr}_2\text{O}_3(0001)/\text{CeO}_2(100)$ is smaller than that of $\text{Cr}_2\text{O}_3(11\bar{2}0)/\text{CeO}_2(100)$. Therefore, we consider that a c -axis-oriented growth was obtained in sample B. The results of XRD analysis indicated that Cr_2O_3 grew on $\text{CeO}_2(100) // \text{STO}(100)$ with a c -axis orientation.

The R_a of the CeO_2 layers was first investigated using a DFM image with a size of $1 \times 1 \mu\text{m}^2$. The R_a values of the CeO_2 buffer in samples A and B were 4.2 and 0.41 nm, respectively.

The DFM surface images of samples A and B are shown in Figs. 5(a) and 5(b). In Fig. 5(a) showing sample A deposited on the rough CeO_2 buffer with $R_a = 4.2 \text{ nm}$, various sizes of grains and deep valleys of grain boundaries were observed and R_a was 17.0 nm. As shown in Fig. 5(b), smooth Cr_2O_3 surfaces with R_a of 4.2 nm were observed on smooth CeO_2 with $R_a = 0.41 \text{ nm}$.

The surfaces of sample A were not smooth and no Bragg diffraction peak was observed. In sample B, valleys disappeared and grains with clear facets appeared.

It was thought that the smooth part of sample B corresponded to the c -planes of Cr_2O_3 . The crystal smoothness of the CeO_2 layer strongly affected Cr_2O_3 growth as an important factor. The crystal quality of Cr_2O_3 film will be improved more by improving the crystalline alignment of CeO_2 layers. From the obtained results on the crystalline structure, Cr_2O_3 films are expected to be applied to devices, for example, as a magnetic control gate layer for novel oxide electronic functional devices fabricated on STO substrates.

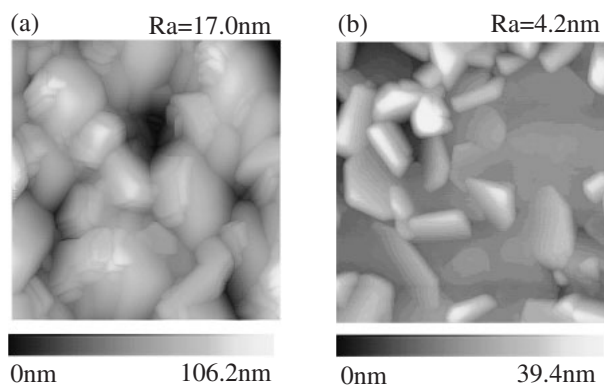


Fig. 5. DFM surface images ($1 \times 1 \mu\text{m}^2$) of Cr_2O_3 films, (a) sample A and (b) sample B. Sample A was deposited on the CeO_2 buffer layer with $R_a = 4.2 \text{ nm}$. Sample B was deposited on the comparatively smooth CeO_2 buffer layer with $R_a = 0.41 \text{ nm}$.

4. Conclusions

The ME Cr_2O_3 films were prepared by sputtering on *R*-cut sapphire and STO with CeO_2 buffers. The grain shape of

Cr_2O_3 was affected by the steps and/or width of terraces in Al_2O_3 substrates. An adequate substrate temperature $T_s = 550^\circ\text{C}$ resulted in a highly oriented Cr_2O_3 growth and the film was composed of coalesced large rectangular grains. The STO substrate with CeO_2 buffer showed the growth of Cr_2O_3 with a *c*-axis orientation. It was also confirmed that superior Cr_2O_3 growth required smooth CeO_2 buffers with small R_a . In conclusion, the Cr_2O_3 films are applicable to novel perovskite oxide crystals fabricated on cubic STO substrates.

- 1) K. Siratori, K. Kohn, and E. Kita: *Acta Phys. Pol. A* **81** (1992) 431.
- 2) P. J. Brown, J. B. Forsyth, and F. Tasset: *Solid State Sci.* **7** (2005) 682.
- 3) H. Wiegmann, A. G. M. Jansen, P. Wyder, J.-P. Rivera, and H. Schmid: *Ferroelectrics* **162** (1994) 141.
- 4) M. Foebig: *J. Phys. D* **38** (2005) 123.
- 5) M. Shirakawa, M. Miura, T. Ohazama, Y. Shingai, A. Saito, M. Mukaida, and S. Ohshima: *Physica C* **412–414** (2004) 1277.
- 6) J. C. Nie, H. Yamasaki, Y. Nakagawa, K. Develos-Bagarinao, M. Murugesan, H. Obara, and Y. Mawatari: *J. Cryst. Growth* **284** (2005) 417.
- 7) H. Y. Lee, S. I. Kim, Y. P. Hong, Y. C. Lee, Y. H. Park, and K. H. Ko: *Surf. Coat. Technol.* **173** (2003) 224.

Growth of Vertically Aligned Carbon Nanotubes Depending on Thickness of Catalyst Films by Plasma-Enhanced Chemical Vapor Deposition

Hiroki Okuyama
Nobuyuki Iwata
Hiroshi Yamamoto

College of Science and Technology, Nihon University,
Funabashi-shi, Chiba, Japan

We attempted to control the diameter and density of vertically aligned carbon nanotubes (VACNTs) using plasma-enhanced chemical vapor deposition. The VACNT diameter was reduced by decreasing the Ni catalyst thickness. Introducing the Mo layer between Ni catalyst and quartz substrate was effective for thin VACNT growth from the thin Ni catalyst film. This result demonstrated that the metal films had to be highly electric-conductive for inducing plasma on the Ni catalyst to grow VACNTs. The maximum density of VACNTs was obtained through the use of optimum plasma pretreatment time.

Keywords: density control; diameter control; Ni catalyst; plasma-enhanced chemical vapor deposition; vertically aligned carbon nanotubes

1. INTRODUCTION

Carbon nanotubes (CNTs) have been studied intensively because of their many characteristics such as high electric conductivity [1], high permissible current density [2], and high mechanical strength in spite of their high flexibility [3]. Furthermore, the growth direction of CNTs is controllable by applying an electric field during chemical vapor deposition (CVD) growth [4]. These characteristics are beneficial to

The authors are grateful for the financial support of a Grant-in-Aid from the Futaba Foundation. This work was supported by the Ministry of Education, Culture, Sports, Science and Technology through a Scientific Grant-in-Aid (No. 15360173).

Address correspondence to Hiroki Okuyama, College of Science and Technology, Nihon University, 7-24-1-401, Narashinodai, Funabashi-shi, Chiba 274-8501, Japan. E-mail: okuyama@yamanoya.ecs.cst.nihon-u.ac.jp

prepare various nanostructures for use in scanning probe microscopy (SPM) tips [5–7], field emitters [8–10], wire of ultra large-scale integrated circuits [11], and so on. The required properties for CNTs are different for each purpose. Requirements pertain for CNTs regarding the diameter and density: high density of thin CNTs is necessary for the wire to satisfy high permissible current density and low resistance [11]. In the case of field emitters, low density of thin CNTs is preferred to enhance the electric field at CNT tips [12]. An individual and a thin CNT are necessary for application in an SPM tip.

In this article, we report vertically aligned (VA) CNT growth using plasma-enhanced (PE) CVD. We attempted to control the diameter and density of VACNTs intended to support electronics applications. Diameter control was investigated using various thicknesses of Ni catalyst and introducing a Mo underlayer. Density control was performed by varying the plasma pretreatment time.

2. EXPERIMENTAL

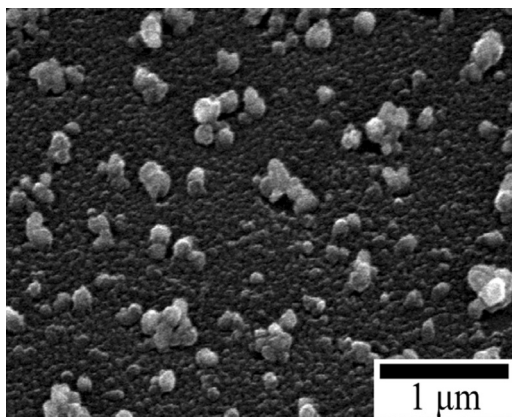
Patterned metals of Ni catalysts and Mo underlayers were deposited on quartz substrates ($5 \times 5 \text{ mm}^2$, 0.5 mm thickness) through a metal mask (30 μm thickness, 200 μm pattern width, 100 μm gap) using radio frequency magnetron sputtering. The chamber background pressure was 3.0×10^{-3} Pa, and the pressure during deposition was fixed at 2.0 Pa by feeding Ar gas. The growth conditions were 120°C substrate temperature and 50 W sputtering power for Mo underlayers, and 70°C and 20 W, respectively, for Ni catalysts. The films' deposition rates were 10 nm/min for Mo and 3.5 nm/min for Ni.

The CNTs were grown using DC PECVD method. The reactor tube of the CVD equipment was heated to 500°C. The background pressure was 0.1 Pa. The flow of H_2 :Ar (50:50 ccm) was introduced into the reactor tube during heating. Plasma pretreatment was performed by inducing DC glow discharge from immediately before the CNT growth. The DC glow discharge was induced by applying a bias voltage of -250 V between the substrate holder and grounded anodes separated from the substrates by approximately 5 mm. The metal pattern was connected electrically to the cathode of substrate holder by applying Ag paste. The CNT growth was performed by adding 5 ccm of ethylene (C_2H_4) gas. The total pressure was maintained at 2 kPa.

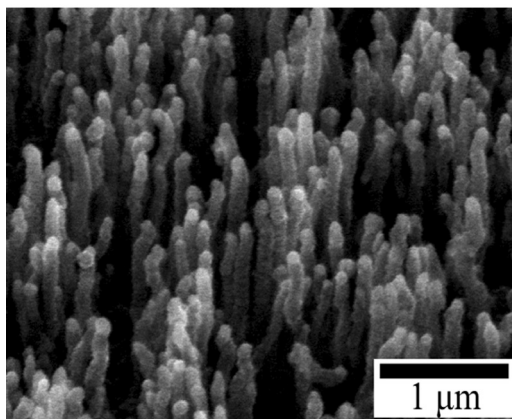
The obtained CNTs were observed using a field emission scanning electron microscope (SEM; S-4500; Hitachi Ltd.) operated at 15 kV and a field emission transmission electron microscope (TEM; HF-2000; Hitachi Ltd.) operated at 200 kV.

3. RESULTS AND DISCUSSION

Figure 1 shows the effect of Ag paste, which electrically connects the Ni/Mo patterns to the cathodes. The respective thicknesses of Ni catalyst and Mo underlayer were 3.5 nm and 10 nm. The specimen of Figure 1(a) was prepared by putting the substrate on the cathode without applying Ag paste. The specimen shown in Figure 1(b) was prepared by electrically connecting the Ni/Mo pattern to the cathode by applying Ag paste. Some particles were observed on the patterns, which were not connected electrically to the cathode. Figure 1(b)



(a)



(b)

FIGURE 1 SEM images of the surface of the Ni/Mo pattern after CVD. (a) The Ni/Mo pattern was not connected electrically to the cathode. (b) The Ni/Mo pattern was connected electrically to the cathode using Ag paste.

shows that VACNTs were prepared on the patterns by applying Ag paste. Figure 2 shows the VACNTs as observed using TEM. The hollow center and graphitic sidewalls were visible. In this case, the number of walls was 25, and the CNT internal and external diameters were *ca.* 4.6 nm and *ca.* 26 nm, respectively.

In the case of PECVD method, a cathode dark space is used mainly for preparing CNTs [13]. The cathode dark space contains many positive ions and radicals. The active species reduce the activation energy for a catalytic reaction. In addition, the voltage drop takes place mostly in the cathode dark space because of its high impedance. The positive ions are accelerated using an electric field; some of them bombard the cathode of catalyst films. These impacts generate catalyst particles from continuous catalyst films [14–16]. The CNTs are aligned using an applied strong electric field. The thickness of the cathode dark space was estimated using the Child-Langmuir law [17]. The estimated thickness of the cathode dark space was 0.21 mm. Therefore, the DC glow discharge was not induced on a quartz substrate with 0.5 mm thickness although the

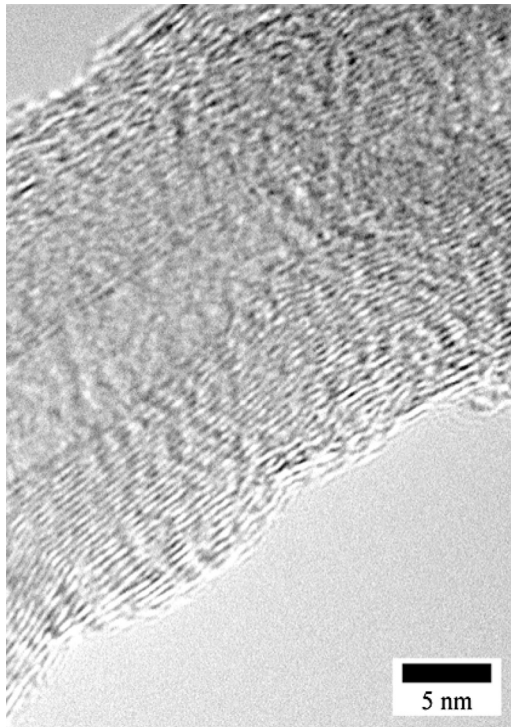


FIGURE 2 Typical TEM image of a VACNT.

substrate was placed on the cathode. The catalysts should be connected electrically to the cathode to induce plasma on the catalysts.

Figure 3 depicts SEM images of VACNTs with various Ni thickness. The Ni thickness, the pattern resistance from the Ag paste, and the diameter and the density of the grown VACNTs are listed in Table 1. The pretreatment was maintained for 1 min. The VACNT diameter was decreased by reducing the Ni catalyst thickness. Figure 3(a) shows that no CNTs grew from 3.5 nm of Ni thickness. Although the Ni thickness was equal to that shown in Figure 3(a), the smallest VACNT diameter was obtained by introducing the Mo underlayer, as shown in Figure 3(d).

The VACNT diameter was reduced by reducing the Ni catalyst thickness. The continuous Ni catalyst films were broken into fine particles using thermal and plasma pretreatment. The CNT diameter is determined by the catalyst particle diameter. In addition, the catalyst particle diameter depends on the initial thickness of the catalyst films [18,19]. However, VACNTs did not grow when the catalyst films were too thin, i.e., 3.5 nm. The pattern conductivity was reduced because

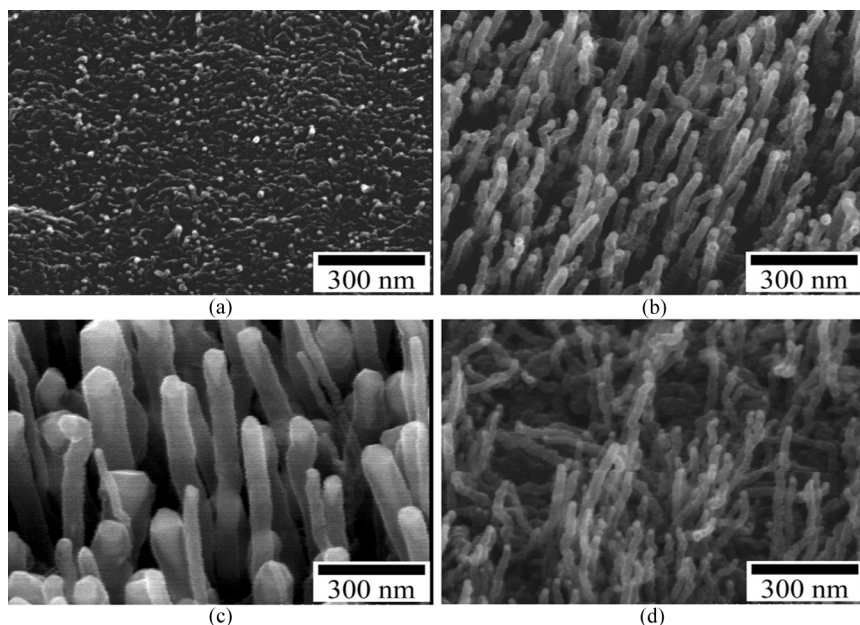
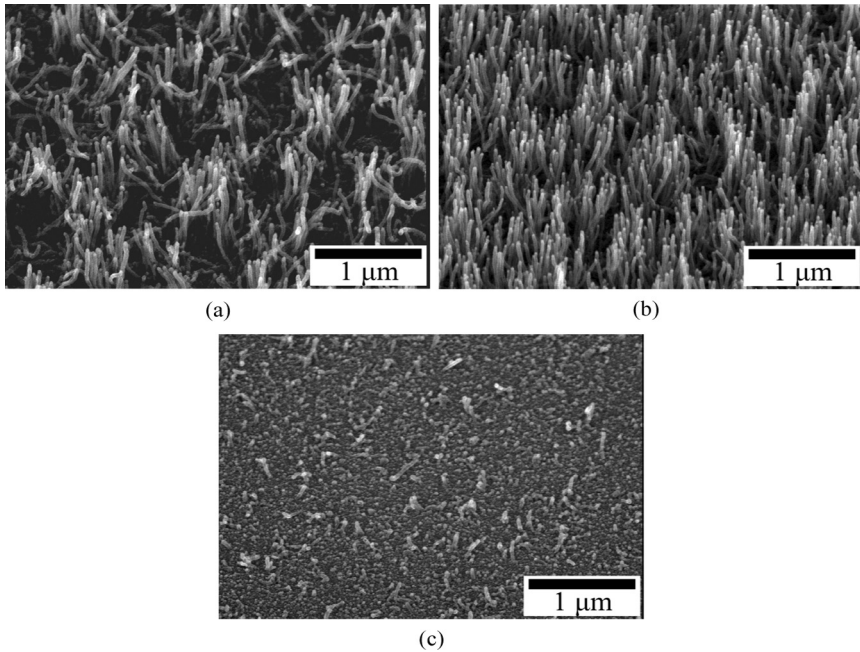


FIGURE 3 SEM images of VACNTs grown from various Ni catalyst thickness. The Ni catalyst film thicknesses were (a) 3.5 nm, (b) 35 nm, (c) 350 nm, and (d) 3.5 nm with a 10 nm Mo underlayer.

TABLE 1 Summary of the Obtained VACNTs with Various Ni Catalyst Thicknesses

	(a)	(b)	(c)	(d)
Thickness of Ni [nm]	3.5	35	350	3.5 with 10 nm Mo
Pattern resistance from Ag paste [Ω]	> 60 M	360 k	12 k	300 k
VACNT diameter [nm]	\times	40	40–150	30
VACNT density [μm^{-2}]	\times	100	30	90

the Ni catalysts formed fine particles. The resistance of the 3.5 nm Ni patterns was greater than 60 M Ω . Therefore, the plasma was not induced on the 3.5 nm Ni patterns during CNT growth because of their high resistance. By introducing the Mo underlayer, VACNTs with smallest diameters were obtained from 3.5 nm Ni patterns. The densities of VACNTs grown from 3.5 nm Ni patterns were slightly less than those of 35 nm Ni. Although the Ni catalysts were thin, plasma was induced on Ni catalysts because of the conductive Mo underlayer

**FIGURE 4** SEM images of the VACNTs at different plasma pretreatment times of (a) 0.5 min, (b) 1 min, and (c) 5 min.

and Ag paste. Therefore, introducing an Mo underlayer is effective for preparing VACNTs with small diameter and low density.

Figure 4 shows SEM images of samples with different plasma pretreatment times. The Ni catalyst and Mo underlayer were 3.5 nm and 10 nm thick, respectively. The pretreatment times were (a) 0.5 min, (b) 1 min, and (c) 5 min. In fact, VACNTs with *ca.* 30 nm of diameter grew from the films, which had been pretreated for 0.5 and 1 min. For pretreatment time of 5 min, poorly aligned CNTs with 20–35 nm diameter and 80–450 nm of length grew sparsely. The respective densities of the VACNTs are shown in Figure 5: they were (a) $50 \mu\text{m}^{-2}$, (b) $90 \mu\text{m}^{-2}$, and (c) $20 \mu\text{m}^{-2}$.

The CNT density was increased by extending the pretreatment time from 0.5 min to 1 min. The plasma induces catalyst films to form fine particles, as discussed above. Many catalyst particles were produced during the extended pretreatment time. However, the CNT density was decreased by extending the pretreatment time to 5 min. The Ni catalyst and Mo underlayer were removed through the use of longer pretreatment times. Sparse CNTs were prepared because a small amount of Ni catalyst remained at the pattern. Short and the poorly aligned CNTs were prepared because the resistance of the Mo underlayer was increased as a result of the reduced thickness.

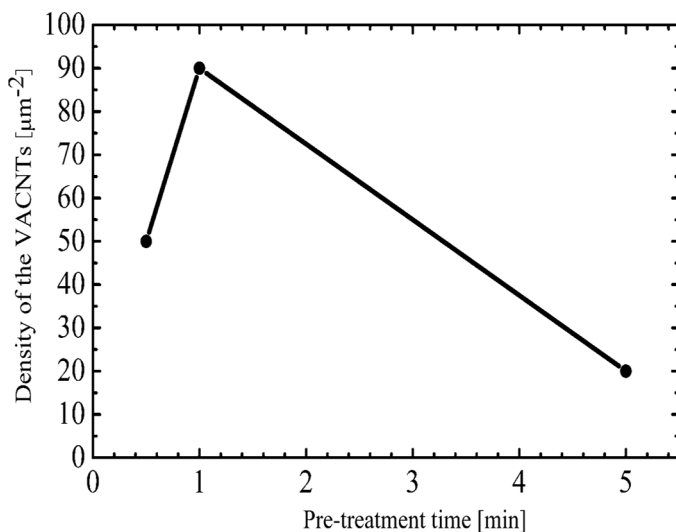


FIGURE 5 Density of the VACNTs as a function of plasma pretreatment time.

4. CONCLUSIONS

We attempted to control the density and the VACNT diameter using DC PECVD. It was important for VACNT growth that the DC plasma be induced onto the Ni catalyst. The VACNT diameter was reduced by decreasing the Ni catalyst thickness. Introducing the Mo underlayer was effective for thin VACNT growth from the thin Ni catalyst film. The VACNT density was maximized by plasma pretreatment time of 1 min. Longer or shorter pretreatment time than 1 min yielded a lower VACNT density.

REFERENCES

- [1] Kong, J., Yenilmez, E., Tomblor, T. W., Kim, W., Dai, H., Laughlin, R. B., Liu, L., Jayanthi, C. S., & Wu, S. Y. (2001). *Phys. Rev. Lett.*, *87*, 106801.
- [2] Yao, Z., Kane, C. L., & Dekker, C. (2000). *Phys. Rev. Lett.*, *84*, 2941.
- [3] Wong, E. W., Sheehan, P. E., & Lieber, C. M. (1997). *Science*, *277*, 1971.
- [4] Merkulov, V. I., Melechko, A. V., Guillorn, M. A., Lowndes, D. H., & Simpson, M. L. (2001). *Appl. Phys. Lett.*, *79*, 2970.
- [5] Hafner, J. H., Cheung, C. L., & Lieber, C. M. (1999). *Nature*, *398*, 761.
- [6] Stevens, R., Nguyen, C., Cassell, A., Delzeit, L., Meyyappan, M., & Han, J. (2000). *Appl. Phys. Lett.*, *77*, 3453.
- [7] Arie, T., Nishijima, H., Akita, S., & Nakayama, Y. (2000). *J. Vac. Sci. Technol. B*, *18*, 104.
- [8] Fan, S., Chapline, M. G., Franklin, N. R., Tomblor, T. W., Cassell, A. M., & Dai, H. (1999). *Science*, *283*, 512.
- [9] Saurakhiya, N., Zhu, Y. W., Cheong, F. C., Ong, C. K., Wee, A. T. S., Lin, J. Y., & Sow, C. H. (2005). *Carbon*, *43*, 2128.
- [10] Milne, W. I., Teo, K. B. K., Amaratunga, G. A. J., Lacerda, R., Legagneux, P., Pirio, G., Semet, V., & Binh, V. T. (2004). *Current Appl. Phys.*, *4*, 513.
- [11] Nihei, M., Kawabata, A., Kondo, D., Horibe, M., Sato, S., & Awano, Y. (2005). *Jpn. J. Appl. Phys.*, *44*, 1626.
- [12] Nilsson, L., Groening, O., Emmenegger, C., Kuettel, O., Schaller, E., Schlapbach, L., Kind, H., Bonard, J.-M., & Kern, K. (2000). *Appl. Phys. Lett.*, *76*, 2071.
- [13] Melechko, A. V., Merkulov, V. I., McKnight, T. E., Guillorn, M. A., Klein, K. L., Lowndes, D. H., & Simpson, M. L. (2005). *J. Appl. Phys.*, *97*, 041301.
- [14] Ren, Z. F., Huang, Z. P., Xu, J. W., Wang, J. H., Bush, P., Siegal, M. P., & Provencio, P. N. (1998). *Science*, *282*, 1105.
- [15] Täschner, Ch., Pácal, F., Leonhardt, A., Spatenka, P., Bartsch, K., Graff, A., & Kaltofen, R. (2003). *Surf. Coat. Tech.*, *174–175*, 81.
- [16] Sato, H., Takegawa, H., & Saito, Y. (2003). *J. Vac. Sci. Technol. B*, *21*, 2564.
- [17] Maissel, L. (1970). In: *Handbook of Thin Film Technology*. Maissel, L. I. & Glang, R. (Eds.), McGraw-Hill Book Company: New York, Chapter 4, 6.
- [18] Chhowalla, M., Teo, K. B. K., Ducatti, C., Rupesinghe, N. L., Amaratunga, G. A. J., Ferrari, A. C., Roy, D., Robertson, J., & Milne, W. I. (2001). *J. Appl. Phys.*, *90*, 5308.
- [19] Bower, C., Zhou, O., Zhu, W., Werder, D. J., & Jin, S. (2000). *Appl. Phys. Lett.*, *77*, 2767.

4.5 光励起プロセスによるフラーレンポリマーの合成

4.5.1 まえがき

C_{60} が sp^3 的結合によって3次元的に共有結合した3次元結晶性 C_{60} ポリマーは、紫外線照射や高温・高圧下によって合成されてきた。^[1]これは、ダイヤモンド以上の硬度を持ち、ultrahard fullerideとも呼ばれる。^[2]さらにこの物質を発展させ、分子同士が無秩序に結合した非晶質構造とすれば、弾性・粘性に富むものとなる。それは超硬質、超軽量、超柔軟という驚異的な特性を持ち、スーパーダイヤモンドと呼ぶにふさわしい優れた材料となるもの期待されている。しかし、 C_{60} 光重合反応や高温・高圧下での反応機構については未だ明確になっていない。また、従来のプロセスでは得られるポリマーの形状や大きさに限界があり、応用へ向けての検討も進んでいない。

本報告では、現在までに試みられてきた C_{60} ポリマー研究を概観した後、山本らの開発している自由電子レーザー(FEL)による光励起3次元 C_{60} ポリマー化プロセス^[3]について紹介する。波長可変性を特長とするFEL^[4]を用いれば、紫外から赤外にわたる広範囲の帯域の中から任意の波長を選び C_{60} に照射することが出来る。このとき、 C_{60} に混入したハロゲン元素(ヨウ素)を光照射によってアクセプタとして作用させ、 C_{60} のエネルギー不安定化をもたらし、重合反応を促進するという新しい手法も開発された。さらに、デバイス応用を視野に入れた、 C_{60} 薄膜成長中にFEL照射を行いながらポリマーを成長させる試みについても紹介する。

4.5.2 C_{60} ポリマー研究の動向

C_{60} 分子の π 電子による二重結合の一部が切れ、隣接する C_{60} 分子(モノマー)間に架橋が生じた状態($-C_{60}-$)_nを C_{60} ポリマーという。Raoら^[5]は固体 C_{60} 薄膜に光(N_2 レーザー、波長337nm)を照射すると C_{60} はポリマーを形成することを報告した。その反応機構として光環化付加反応(2+2)が提唱された。隣接する C_{60} 分子の(C=C)二重結合が平行でかつ4.2Åより近い距離にあるときに光が当たると、2-2環化付加反応によって隣接分子をつなぐ四員環が形成されるという。光ポリマー化は C_{60} が自由に回転している260Kより高い温度でのみ進行する。また、固体 C_{60} が酸素と結合していると光誘起ポリマー化は起こりにくいことも指摘されている。

高温高圧処理を施した C_{60} は新しい凝集相を形成する。Iwasaら^[6]は酸素を遮断した雰囲気中で結晶を高温高圧(300~800℃, ~5GPa)で1時間処理した後、常温常圧に戻した試料を分析した。その結果、熱処理温度が300~400℃の範囲では格子定数の縮まったfcc(F)相が形成され、X線回折のピーク幅は約20%広くなり、 C_{60} 分子間の距離が約0.1Å短くなることを示した。また、500~800℃では三方晶trigonal相(図4.5.1(C))、700℃-4GPaと600℃-3GPaでは2次元的な三方晶相と正方晶tetragonal(図4.5.1(B))の混合物^[7]、300℃-8GPaでは1次元的な斜方晶

orthorhombic(図4.5.1(A))が得られることも報告されている。さらに高温・高圧で処理すればダイヤモンド級に硬いアモルファスな超硬炭素が得られるとMoretら^[8]は報告している。

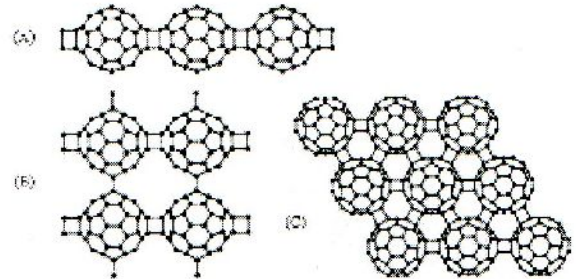


図4.5.1 代表的、 C_{60} ポリマー相 (A)1次元斜方晶相、(B)2次元正方晶相、(C)2次元三方晶相

出典：P. C. Eklund and A. M. Rao Eds., *Fullerene Polymers and Fullerene Polymer Composites*, Springer, Berlin, 1999, p.252.

最近、Blankら^[9]やChiら^[10]に引き続き、Yamanakaら^[11]は C_{60} 2次元ポリマー単結晶を出発物質として、15GPaの高圧処理によって3次元ポリマー単結晶を合成することに成功し、その詳しい結晶構造を解析した。

一般的な C_{60} ポリマーの特徴としては、 sp^3 結合の出現、分子間距離の短縮化、対称性の低下、分子内C=C伸縮振動のソフト化、有機溶媒に不溶などがあげられる。 C_{60} ポリマーは準安定状態であり、加熱(~200℃)すると元のモノマーに戻るという特徴もある。その際、ポリマーの結合を切ってモノマーに戻る活性化エネルギーは約1.25eVである。中でも興味深い物性はその硬度である。密度3.5g/cm³のダイヤモンドを密度2.7g/cm³のポリマーで傷をつけることができる^[12]と報告されている。^[12]ポリマーの密度とピッカース硬度の関係をみると、フラーレンポリマーは密度は低いにもかかわらず極めて高い硬度を示しており、^[12]超硬度材料として大いに期待される。

フラーレン重合体合成との関連において、グラファイトにホールドーピングすることで、比較的低温・低圧条件のもとで層間を共有結合させてダイヤモンドを合成するプロセスが開発された。基底状態のグラファイトとダイヤモンドの間には、一原子当たり約0.3eVのエネルギーを励起しなければ越えられないエネルギーの壁が存在する。圧力を印加することでこのエネルギーの壁はしだいに減少し、40GPaを超えると壁はほぼ消失する。つまり、グラファイトからダイヤモンドへの構造変化が可能となることが指摘された。これが一般的に知られている人工ダイヤモンドの高圧合成の原理である。Nakayamaら^[13]の報告によると、グラファイトにホールドーピングを行い、そのドーピング量を増す(~0.25/atom)ことで、エントロピーダイヤグラムは圧力印加と同様のカーブを描くという。価電子帯に正孔が励起され

た状態ではグラファイト構造が著しく不安定になり、安定なダイヤモンドへ構造変化するのであるが、言い換えれば、ホールドープを行ったグラファイト中の炭素原子は、超高圧下におけるエネルギー状態と同一視することが出来る。

このことはグラファイトと同じ表面構造を持つフラーレン、 C_{60} に対しても有効であると期待される。例えば、Endoら^[14]はボロンを用いたカーボナノチューブへのホールドープと熱処理(～2000℃)でナノチューブ同士を結合させることに成功している。本報告で紹介されるハロゲンを用いた光励起ホールドーピング法はこのような効果を期待したものである。

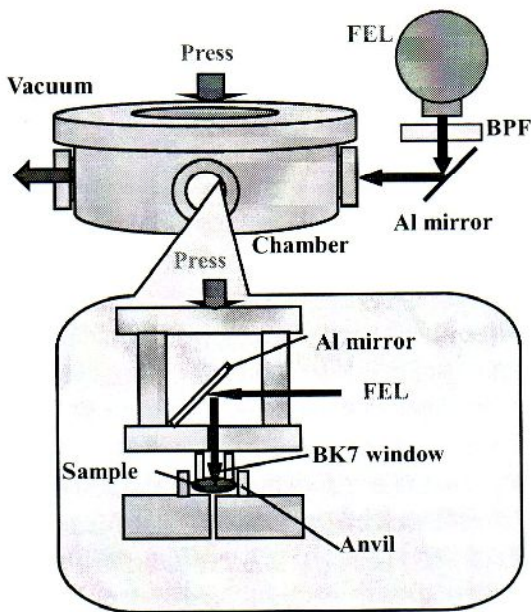


図 4.5.2 FEL 照射プロセスの装置模式図

4.5.3 バルクプロセス実験

試料は真空中で加圧・レーザー照射することにより作製された。図 4.5.2 に用いられた装置の概略を示す。 C_{60} 粉末のみのサンプルと、 C_{60} と I_2 を mol 比 1:4 で混合した 2 種類を出発原料とした。それを SUS304 製アンビルに詰め、光学ウインドウ (BK7 または合成石英製) を蓋として圧力を加えた。真空排気、アンビル加熱後に、FEL を光学ミラーならびに狭帯域フィルター (BPF) を通して試料に照射した。得られる試料は、高さ約 1 mm、直径 5 mm ϕ の円盤状である。

FEL 波長は可変であり、基本波を 1050～1800 nm の波長範囲で変化させ、その 3 倍高調波が用いられた。ここで用いられた FEL は強い高調波を発振できるところに特徴がある。^[15] 特に、1450 nm の 3 倍高調波 (450 nm)、1725 nm の 5 倍高調波 (345 nm) が詳しく検討された。450 nm はベンゼン環の結合エネルギーより見積られた、 C_{60} の二重結合を打ち切るのに必要なエネルギーに相当する波長である。BPF を通した場合には 0.1 mJ/Pulse 以下の小さなレーザー強度となるが、450 nm や 345 nm FEL 高調波は比較的強度が高く、それぞれ約 0.5 mJ/Pulse、約 2 mJ/Pulse であった。繰り返し周波数は

2 Hz で 120～300 min の照射が行われた。

4.5.4 薄膜プロセス実験

C_{60} 分子のマイカ基板上への蒸着時に、波長 1350 nm の FEL (第 3 高調波を含む) が照射された。FEL パルスの繰り返し周波数は 2 Hz であり、その強度は 2.3 mJ/pulse であった。PNB クヌードセンサーより C_{60} は蒸着され、真空度は 2×10^{-5} Pa、基板温度は 42℃、蒸着速度は約 2.1 Å/s とした。同条件で FEL を照射せずに C_{60} 薄膜が作製され、特性比較試料とされた。

4.5.5 評価方法と結果

試料の評価にはラマン分光装置、X 線回折装置を使用された。特に、ラマン分光において C_{60} 分子の $A_g(2)$ 振動モードが着目された。IR およびラマンスペクトルには C_{60} 分子の対称性の低下により、それまで縮退していた分子振動による多くの新しいピークが出現する。また、アルゴンイオンレーザー励起のラマン散乱の測定において、 C_{60} の分子振動のうち C=C 伸縮振動に由来する $A_g(2)$ 振動 (五角形が伸縮する“ペンタゴナルピンチ”モード) の振動数が、励起光強度が 50 mW/mm^2 を超えると 1469 cm^{-1} から 1460 cm^{-1} にシフトする原因もポリマー化によるものだと言われている。^[6] その変化量は重合反応の指標として用いることができる。

BPF を用いて波長を 350～600 nm まで変化させながら照射を行ない、X 線回折によって得られた試料の格子定数を評価した。図 4.5.3 に測定結果の一例を示す。変化量は小さいものの、波長約 500 nm の FEL 照射において面間隔の縮小効果が大きいことが分かった。ただし、紫外域でのレーザー強度は著しく低下している可能性を検討する必要がある。

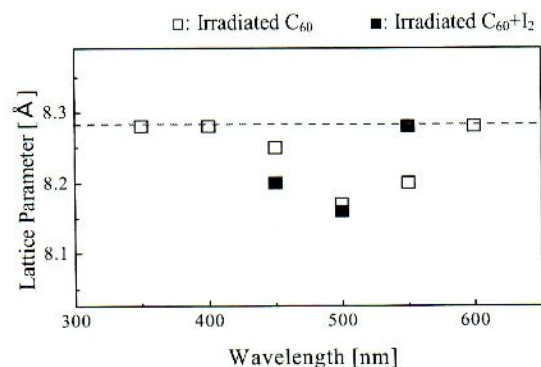


図 4.5.3 FEL 照射試料の格子定数における波長依存性

図 4.5.4 に 450 nm FEL 照射試料におけるラマン分光結果を示す。 C_{60} 試料のピークは約 3 cm^{-1} レッドシフトし、 I_2 添加サンプルでは 8 cm^{-1} に達した。また、345 nm FEL 照射試料のラマン分光結果を図 4.5.5 に示す。ここでは明確なピーク分裂が観察された。これは試料による照射光の吸収によって、表面近傍のみで光重合反応が進んだ結果であると

考えられる。そのピーク変化量に着目すると、 C_{60} では約 8 cm^{-1} 、 I_2 添加サンプルでは約 10 cm^{-1} に及ぶ大きなピークシフトが確認された。いずれの波長の照射実験においても、明確な I_2 添加効果が確認できた。一方、X 線回折ピークのブロード化と格子定数の減少が観察され、ポリマー化の進行が確かめられた。

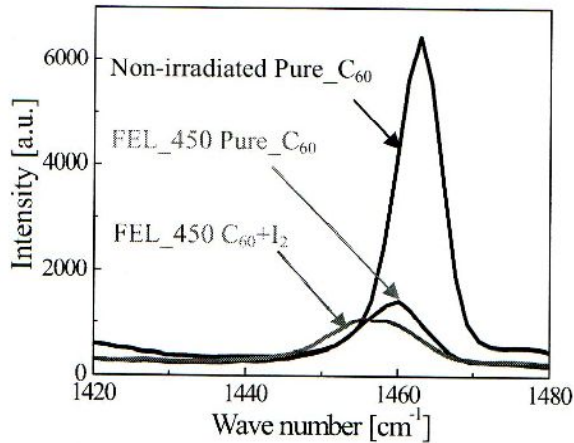


図 4.5.4 450 nm FEL 照射試料のラマンスペクトル

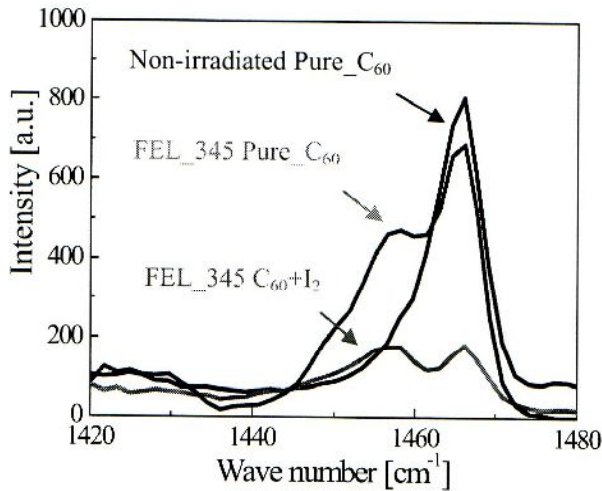


図 4.5.5 345 nm FEL 照射試料のラマンスペクトル

一方、FEL 照射薄膜プロセスによって作製された試料のラマン分光の結果を図 4.5.6 に示す。 C_{60} 薄膜で 1469 cm^{-1} に観察された $A_g(2)$ ピークは FEL 照射下で作製された膜では 8.1 cm^{-1} 低エネルギー側にシフトした。このラマンピークシフトは明確なポリマー化反応の進行を示唆している。スペクトル中にはなお一部未反応の部分が残されているが、これは今後照射条件の最適化によって減少させることは可能であると思われる。今後、膜厚を厚くする過程において、ポリマーからモノマーへの変化が生じる可能性についても検討を加える必要があるだろう。

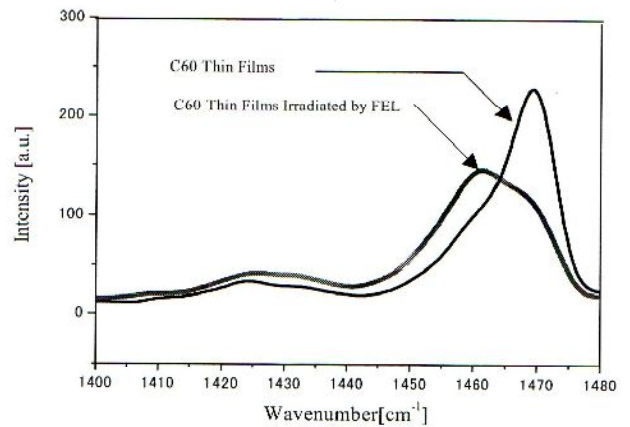


図 4.5.6 1350 nm FEL 照射 C_{60} 薄膜のラマンスペクトル

4.5.6 あとがき

以上、フラーレン C_{60} ポリマーに関する研究の概略を述べ、最近の C_{60} ポリマー合成研究の概略を紹介した。 C_{60} とヨウ素混合粉末を真空中で加圧・FEL 照射することによって得られた試料のラマンピークシフト量の大幅な増加と X 線回折等の結果より、FEL の波長選択照射とヨウ素添加による光励起反応によりポリマー化反応を大幅に促進できることが明らかとなった。しかし、その反応は試料の光吸収のため、表面近傍でのみ進行しており、比較的大きな試料を作製するにはプロセスの改善が必要となることも分かった。そこで、 C_{60} 薄膜成長中の FEL 照射によって連続的にポリマーを成長させる可能性も検討されており、反応温度や時間に関する検討は今後の課題であるが、明確なポリマー化反応が確認された。この手法によって厚膜が形成できれば、硬度等の機械的性質や電気物性についての解析が進めるであろう。

参考文献

- (1) P. C. Eklund and A. M. Rao Eds., *Fullerene Polymers and Fullerene Polymer Composites*, Springer, Berlin, 1999.
- (2) V. D. Blank et al., *Diamond Related Mater.*, **7** (1998) 427.
- (3) E-MRS Proceedings
- (4) H. P. Freund and J. T. M. Antonsen, *Principles of Free-Electron Lasers*, Chapman & Hall, London, 1992.
- (5) A. M. Rao et al., *Science*, **259** (1993) 955.
- (6) Y. Iwasa et al., *Science*, **264** (1995) 1570.
- (7) M. Nunez-Regueiro et al., *Phys. Rev. Lett.*, **74** (1995) 278.
- (8) R. Moret et al., *Europhys. Lett.*, **40** (1997) 55.
- (9) V. D. Blank et al., *Carbon*, **36** (1998) 319.
- (10) D. H. Chi et al., *Phys. Rev.*, **B68** (2003) 153402.
- (11) S. Yamanaka et al., *Phys. Rev. Lett.*, **96** (2006) 076620.
- (12) 山中, 久保, *固体物理*, **41** (2006) 407.
- (13) H. Nakayama et al., *J. Phys. Condens. Matter.*, **41** (2002) 817.
- (14) M. Endo et al., *J. Amer. Chem. Soc.*, **5** (2005) 1099.
- (15) Y. Hayakawa et al., *Nucl. Instr. And Meth.*, **A507** (2003) 404.

Fabrication of Carbon Nanofiber Emitters for Excitation of Organic Phosphor Thin Films

Shinji IDE, Masato YOSHIKUNI, Nobuyuki IWATA, and Hiroshi YAMAMOTO

College of Science and Technology, Nihon University, 7-24-1 Narashinodai, Funabashi, Chiba 274-8501, Japan

(Received July 12, 2007; revised September 27, 2007; accepted October 11, 2007; published online January 22, 2008)

For applications to a novel low-voltage acceleration field emission display, carbon nanofiber (CNF) emitters were fabricated using a screen printing method. The two types of CNF of different lengths, normal-length CNFs, and cut CNFs were examined. A current density of 1.4 mA/cm^2 was achieved at $10 \text{ V}/\mu\text{m}$ in CNF emitters prepared from the paste composed of normal-length CNFs (1 wt %), glass paste (6 wt %), and gold nanometal ink (30 wt %). The field enhancement factor β in the Fowler–Nordheim equation was *ca.* 5800. CNF emitters without gold nanometal ink showed low performance. Emitter performance was determined on the basis of the results of scanning electron microscopy (SEM) and field emission characteristics. [DOI: 10.1143/JJAP.47.700]

KEYWORDS: carbon nanofiber, field emission display, screen printing, CNF emitter, emission current density

1. Introduction

Recently, organic light-emitting devices (OLEDs) and field emission displays (FEDs) have been investigated aggressively as next generation displays. However, each display has its own problems: limited lifetime for OLEDs or high acceleration voltage for FEDs. We have proposed a novel low-voltage acceleration field emission display (LV-FED) composed of simply fabricated carbon nanofiber (CNF) emitters and organic electroluminescent (EL) thin films as shown in Fig. 1.¹⁾ The specific structural features of high luminescence efficiency and long lifetime are due to the difference in reflectance between vacuum and emissive layers and/or the absence of cathode layers. In our previous study, a stacking structure of tris(8-hydroxyquinolate)-aluminum (Alq_3)/ N,N' -di-[(1-naphthyl)- N,N' -diphenyl]-(1,1'-biphenyl)-4,4'-diamine (α -NPD)/CuPc on indium tin oxide (ITO) substrates was irradiated by thermally activated electrons with an emission current density of *ca.* 1 mA/cm^2 .^{2,3)} However, the observed luminescence disappeared quickly in 10 s. It was concluded that the deterioration of luminescence was caused by the accumulation of electrons at the interfaces of Alq_3/α -NPD because of an insufficient electric field applied in the organic stacking layers. This problem will be overcome by placing electron emitters close to luminescent layers. For example, with $50 \mu\text{m}$ and 500 V between the cathode and the anode, an electric field of $10 \text{ V}/\mu\text{m}$ is applied.⁴⁾

We aimed to simply fabricate CNF emitters applicable to the above-proposed LV-FED. Two kinds of CNF were investigated. The purpose of comparing a normal-length fiber with a shortened fiber is to study the dependence of CNF emitter performance on length and/or shape. Normal-length tangled and short-length CNFs easily came apart in the paste. Therefore, two types of emitter site are expected. In one type of site, the side of tangled CNFs are not surrounded by paste and not exposed on paste surfaces. In other type of emitter site, the ends of CNFs protrude from paste surfaces. The latter type is expected for cut-CNFs rather than normal-length CNFs. Moreover, binder materials and conducting materials in CNF paste were studied to obtain excellent field emission properties.⁵⁾ Glass paste was used as the binder material to increase adhesive strength and gold nanometal ink as the conducting material to increase electric conductivity between CNFs and the substrate. The

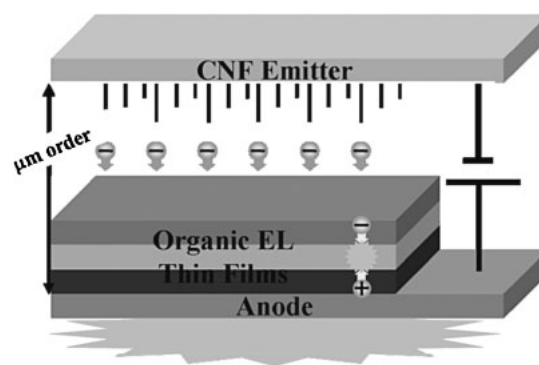


Fig. 1. Schematic configuration of the novel LV-FED composed of simply fabricated CNF emitters and EL thin films.

CNF emitter fabrication technique used was a screen printing method. The method using CNF paste has been recognized as a promising technique for FED fabrication, which is applicable to large-area displays or amenable to mass production.⁶⁾ We intended here to prepare CNF emitters that can achieve an emission current density higher than 1 mA/cm^2 .

2. Experimental Procedure

CNF emitters were fabricated on an ITO substrate using a screen printing method. The CNFs used were multiwall carbon nanofibers (MWCNFs) produced by Showa Denko. The CNFs were massively synthesized from a mixed solution of ferrocene, thiophene, and benzene by thermal chemical vapor deposition at *ca.* 1000°C . The obtained CNFs were baked above 2500°C for 30 min to eliminate amorphous carbon and catalysts.⁷⁾ The CNFs used were multiwalled with a diameter of about $0.1 \mu\text{m}$ (hereafter, normal-length CNFs). The shorted CNFs (hereafter, cut-CNFs), which were prepared from the normal-length CNFs by a fragmentation process, were also used. The scanning electron microscopy (SEM) images of normal-length CNFs and cut-CNFs are shown in Fig. 2. The normal-length CNFs were tangled and the cut-CNFs were straight. The lengths of normal-length CNFs and cut-CNFs were *ca.* $20 \mu\text{m}$ and less than $20 \mu\text{m}$, respectively. The insulating glass paste (Asahi Glass AP5346) and conducting gold nanometal ink (ULVAC Materials Au1T) were adopted as CNF binding materials.

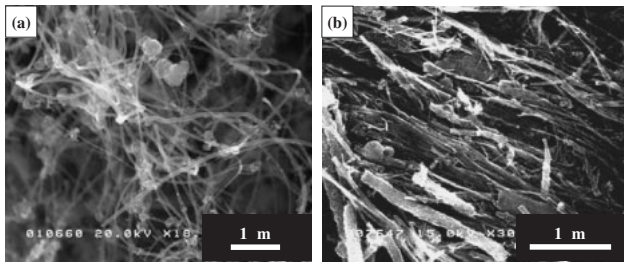


Fig. 2. SEM images of (a) normal-length and (b) cut-CNFs.

Table I. Preparation conditions of CNF emitters (unit: wt %).

Sample	N1G6Au0	N1G6Au30	C1G6Au0	C1G6Au30
CNF	Normal	Normal	Cut	Cut
	1	1	1	1
Gold nanometal ink	0	30	0	30
α -Terpineol	93	63	93	63
Glass paste	6	6	6	6

In Table I, the preparation conditions of CNF emitters are summarized. The normal-length or cut-CNFs (1 wt %) were dispersed in α -terpineol and sonicated for 24 h. The solution with glass paste (6 wt %) and gold nanometal ink (0 or 30 wt %) was mixed and stirred for 30 min. CNFs were presonicated in gold nanometal ink for 1 h. The obtained solution was CNF paste. Regarding the CNF emitter sample name, the first initial N or C means normal-length or cut-CNF, respectively. The second initial G means glass paste and the third initial Au means gold nanometal ink. The number appearing with the name is the wt % of each component.

ITO substrates were cleaned by rinsing in acetone and ethanol, and then dried in blown compressed nitrogen gas. The substrate size was $10 \times 20 \text{ mm}^2$. Squeezed CNF paste was dried at 150°C for 10 min and baked at 510°C for 5 min to remove organic solution in the paste.

The CNF emitter surface morphology was observed by SEM. Emission current was measured in 3×10^{-6} Torr at room temperature. The distance between an anode copper plate and the cathode CNF emitter was *ca.* $50 \mu\text{m}$. The emission sites should be distributed uniformly. There were, however, inequalities on screen-printed surfaces. Therefore, the gap length of electrodes is a critical parameter for emitter performance. In this work, a gap of *ca.* $50 \mu\text{m}$ was investigated because the length of CNFs and the roughness of paste surfaces were typically in a few micrometer order. The emission area was $5 \times 5 \text{ mm}^2$.

3. Results and Discussion

The SEM images of N1G6Au0 and C1G6Au0 are shown in Figs. 3(a) and 3(b). Furthermore, those of N1G6Au30 and C1G6Au30 with gold nanometal ink are shown in Figs. 3(c) and 3(d). In N1G6Au0, CNFs and the glass paste were intermingled and CNFs stood against glass particles. The glass particles were round. The diameter and the length of protruded CNFs were 20–200 nm and $5 \mu\text{m}$, respectively. The glass paste held CNFs and increased adhesive strength. In C1G6Au0, the emitter CNF bunches were filled with glass

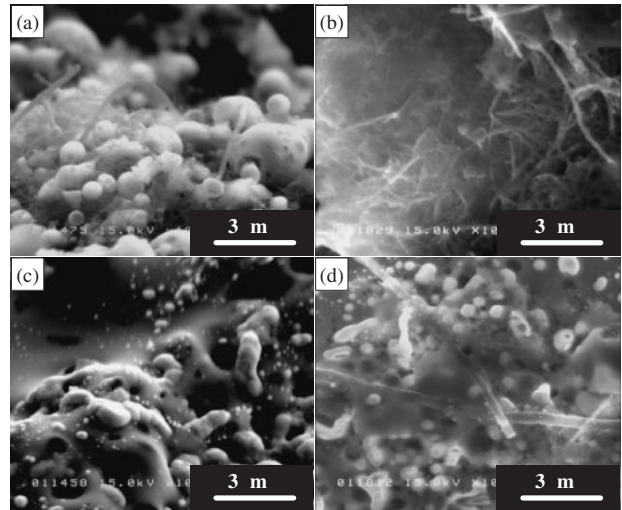


Fig. 3. SEM images of CNF emitters (a) N1G6Au0, (b) N1G6Au30, (c) C1G6Au0, and (d) C1G6Au30.

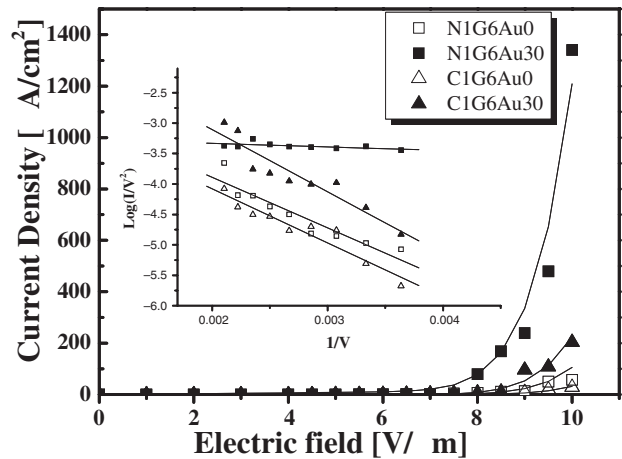


Fig. 4. Emission current density vs. applied electric field. The solid lines are theoretical fitting curves obtained using the Fowler–Nordheim equation with each evaluated β value. The inset shows $\log(I/V^2)$ vs. $1/V$.

particles. N1G6Au30 showed a cluster of glass and gold but CNFs were not clearly observed. In C1G6Au30, the diameter and the length of CNFs were *ca.* 200 nm and over $6 \mu\text{m}$, respectively.

The bent normal-length CNFs protruded from the glass paste surface, whereas cut-CNFs were buried in the glass paste. Thus, the considered sufficient field emission was expected in the normal-length CNF emitter. The SEM images suggest that glass paste is a suitable binder material and normal-length CNFs are suitable for emitter materials.

Figure 4 shows the obtained emission current density as a function of applied electric field. N1G6Au30 revealed a much higher emission current density than other samples. A current density of 1.4 mA/cm^2 was achieved at $10 \text{ V}/\mu\text{m}$. The emission currents obtained from C1G6Au0, N1G6Au0, and C1G6Au30 were smaller, 29, 58, and $230 \mu\text{A/cm}^2$, at $10 \text{ V}/\mu\text{m}$, respectively. It was noted that the current density obtained from normal-length CNF emitter N1G6Au30 was about 6 times as large as that from cut-CNF emitter C1G6Au30. Defining the turn-on electric field E_{10} as the

value at which a current density of $1 \mu\text{A}/\text{cm}^2$ was observed, E_{to} was $6 \text{ V}/\mu\text{m}$ in N1G6Au30. Other emitters showed high E_{to} , $8 \text{ V}/\mu\text{m}$.

The emitters containing gold nanometal ink showed higher current densities. Gold nanometal ink was suitable for increasing emission current density because electric conductivity between CNFs and substrates increased.

The insert in Fig. 4 shows the Fowler–Nordheim⁸⁾ plots. The field enhancement factor β was evaluated by fitting the experimental data, assuming that the work function of CNF is 5 eV .⁹⁾ The solid curves and lines are fitting results obtained using the β value of each emitter. The β value of N1G6Au30 was larger, *ca.* 5800, than that of other samples.

From the observation of SEM images, it was found that normal-length CNFs leaned against each other and cut-CNFs were lying on paste surfaces. The applied electric field is easily concentrated at the ends of the leaning CNFs, which functioned as effective emitter sites. Thus, an inferior emitter performance was obtained in the case of using the cut-CNFs. Gold nanometal ink included in the glass binder is expected to induce electric activity for CNFs noncontacting with substrates. On the other hand, small air spaces in tangled CNFs are not filled by the glass binder. Even in this case, very small gold nanometal ink particles with a diameter of *ca.* 7 nm adhere to CNFs and might improve the electric contact between CNFs. Thus, the total electric conductivity of CNFs on substrates increases and the density of emission sites increases. As a result, the sample with gold nanometal ink showed better emission performance.

Conclusively it was demonstrated that as emitter materials, normal-length CNFs and gold nanometal ink are suitable for obtaining a high performance of a CNF emitter prepared by a screen printing method.

4. Conclusions

CNF paste mixed with glass paste and gold nanometal ink was adopted to prepare CNF emitters with high performance. The glass paste was used to increase adhesive strength with substrates. The gold nanometal ink was used to increase electric conductivity between CNFs and substrates. Also, the two types of CNF with different lengths, normal-length CNFs and cut-CNFs were examined. The highest emission current density obtained was $1.4 \text{ mA}/\text{cm}^2$ at $10 \text{ V}/\mu\text{m}$ in the emitter composed of 1 wt% normal-length CNFs and 30 wt% gold nanometal ink. The field enhancement factor β in the Fowler–Nordheim equation was *ca.* 5800. Since current density above $1 \text{ mA}/\text{cm}^2$ was successfully obtained from the simply prepared CNF emitters, they will be applied to novel LV-FEDs.

- 1) N. Iwata, Y. Hata, M. Yoshikuni, and H. Yamamoto: *Mater. Sci. Eng. C* **27** (2007) 1174.
- 2) K. Onozuka, N. Iwata, and H. Yamamoto: *Int. J. Mod. Phys. B* **16** (2002) 4445.
- 3) Y. Hata, T. Ichinose, N. Iwata, and H. Yamamoto: *Trans. Mater. Res. Soc. Jpn.* **30** (2005) 175.
- 4) B. J. Chen, W. Y. Lai, Z. Q. Gao, C. S. Lee, S. T. Lee, and W. A. Gambling: *Appl. Phys. Lett.* **75** (1999) 4010.
- 5) H. Y. Shin, W. S. Chung, K. H. Kim, Y. R. Cho, and B. C. Shin: *J. Vac. Sci. Technol. B* **23** (2005) 2369.
- 6) H. Machida, S. Honda, S. Ohkura, K. Oura, H. Inakura, and M. Katayama: *Jpn. J. Appl. Phys.* **45** (2006) 1044.
- 7) M. Yoshikuni, S. Ide, N. Iwata, and H. Yamamoto: *Trans. Mater. Res. Soc. Jpn.* **32** (2006) 329.
- 8) R. H. Fowler and L. W. Nordheim: *Proc. R. Soc. London, Ser. A* **119** (1928) 173.
- 9) O. Gröning, O. M. Küttel, C. Emmenegger, P. Gröning, and L. Schlapbach: *J. Vac. Sci. Technol. B* **18** (2000) 665.

Development of high capacity Stirling type pulse tube cryocooler

J. Imura ^{a,*}, S. Shinoki ^a, T. Sato ^a, N. Iwata ^a, H. Yamamoto ^a, K. Yasohama ^a, Y. Ohashi ^b,
H. Nomachi ^b, N. Okumura ^b, S. Nagaya ^c, T. Tamada ^c, N. Hirano ^c

^a College of Science and Technology, Nihon University, 7-24-1, Narashinodai, Funabashi-shi, Chiba 274-8501, Japan

^b Aisin Seiki Co., Ltd., 2-1, Asahi-machi, Kariya, Aichi 448-8650, Japan

^c Chubu Electric Power Co., Inc., 1, Toshin-cho, Higashi-ku, Nagoya-shi, Aichi 261-8680, Japan

Accepted 5 April 2007

Available online 5 June 2007

Abstract

We have been developing a Stirling type pulse tube cryocooler, aiming for a cooling capacity of 200 W at 80 K for a superconducting magnetic energy storage system. In this work, we adopted stainless steel meshes for the regenerator of the cryocooler, and studied the influences of the mesh number on the cooling capacity. The prepared mesh numbers were #150, 200, 250, 350 and 400. Using #250 mesh, and at a frequency of 45 Hz and power consumption of 3.1 kW, the achievable lowest temperature and cooling capacity at 80 K was 46.2 K and 123 W, respectively. Furthermore, in order to optimize the performance, some regenerators were made by stacking several kinds of meshes with different stacking orders. Using these regenerators, we have obtained a high cooling capacity of 169 W at 80 K with power consumption of 4 kW.

© 2007 Elsevier B.V. All rights reserved.

PACS: 07.20.Mc

Keywords: Pulse tube cryocooler; Regenerator; Cooling capacity

1. Introduction

Usually there is a method of using liquid gases such as liquid helium or liquid nitrogen, for cooling of superconducting apparatus. However, considering running cost and troubles of handling liquid gases, usage of a cryocooler is much preferable. Typical cryocoolers are Stirling [1] cryocooler, Gifford-McMahon (GM) cryocooler [2] and pulse tube cryocooler [3–5]. The pulse tube cryocooler is divided into two types of Stirling and GM according to the method of pressure wave generations. Stirling and GM cryocoolers have a displacer for phase shifting at low temperature part. This moving displacer induces undesirable vibrations in these cryocoolers. However, the pulse tube cryocooler does not have such a displacer, so we can expect it has low vibration and high reliability.

We have been developing a Stirling type pulse tube cryocooler, aiming at a cooling capacity of 200 W at 80 K for a superconducting magnetic energy storage system. In order to achieve the purpose, we investigated the characteristics of a regenerator that is one of the most important components of a cryocooler.

2. Experimental

Fig. 1 shows a schematic drawing of Stirling type pulse tube cryocooler used in this experiment. As shown in Fig. 1, the cryocooler consists of a pressure wave generator (PWG) [6], heat exchangers, a regenerator, a cold head, a pulse tube, and a phase shifting system made up with an inertance tube [7] and a buffer tank.

The linear compressor of CFIC Inc. was used as a PWG. The pistons of the linear compressor were diameter of

* Corresponding author. Tel./fax: +81 47 469 5457.

E-mail address: junnosuke_imura@yahoo.co.jp (J. Imura).

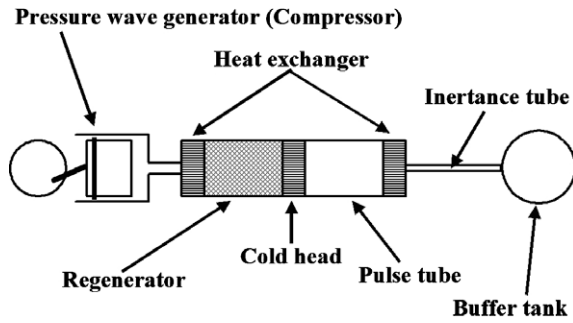


Fig. 1. Schematics of Stirling type pulse tube cryocooler.

115 mm and length of 50 mm. Displacement of the piston was 20 mm of peak to peak (P-P) at the maximum.

Pulse tube was diameter of 40 mm and length of 200 mm.

The regenerator was diameter of 100 mm and length of 60 or 80 mm. We have prepared different meshes for the regenerator; these numbers are #150, 200, 250, 350 and 400 mesh. These meshes had almost the same porosity.

An inertance tube, which is suitable for high frequency operation of 50 Hz around, was adopted as a phase shifting system. The external diameter of inertance tube was 12.7 mm, thickness 1 mm, and length 1.2 m. The capacity of the buffer tank was 3.78 l.

Working fluid was helium gas and its charged pressure is 2 MPa.

Temperature at the cold head and regenerator was measured by using Pt–Co and Pt resistance thermometers, respectively.

Pressure amplitudes of helium gas were measured at the output of the PWG (P_1) and at the inlet of the inertance tube (P_2).

3. Results and discussion

At first, we show the results for the regenerators made by stacking one kind of meshes. Experiments were carried out at driving frequency of 45 Hz and piston displacements of 14.5 mm P-P. The lowest temperature of the cold head

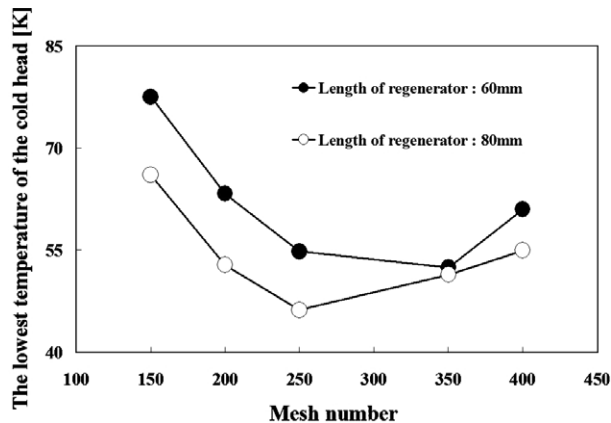


Fig. 2. The lowest temperature of the cold head vs. mesh number.

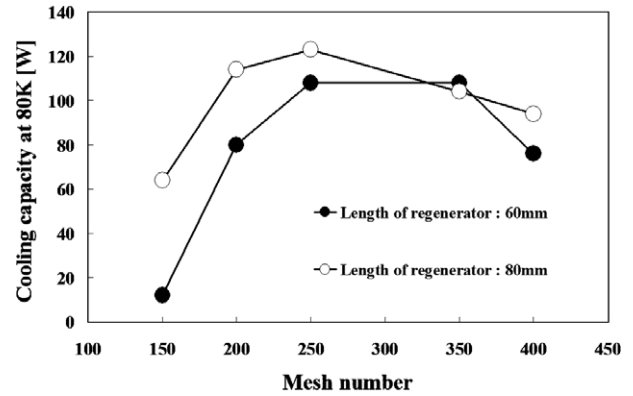


Fig. 3. Cooling capacity at 80 K vs. mesh number.

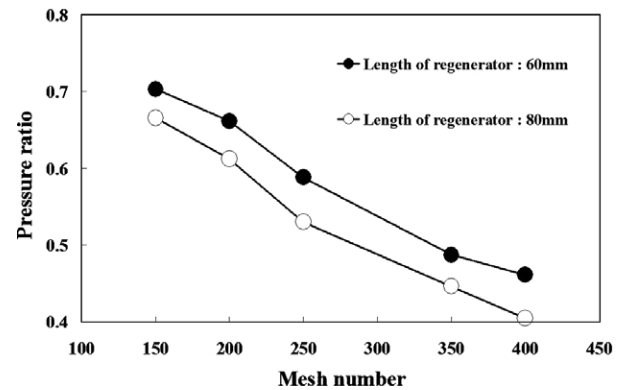


Fig. 4. Pressure ratio vs. mesh number.

and cooling capacity at 80 K vs. mesh number are shown in Figs. 2 and 3, respectively. With #250 mesh, the lower temperature of cold head and highest cooling capacity at 80 K were obtained in this series. Furthermore, as for the length of regenerator, 80 mm is better than 60 mm. With #250 mesh and regenerator length of 80 mm, the lowest temperature of the cold head and the highest cooling capacity at 80 K was 46.2 K and 123 W, respectively. In this case, power consumption was 3.1 kW. Fig. 4 shows pressure ratio P_2/P_1 vs. mesh size. Pressure wave is transmitted in the direction of the pulse tube from the PWG. When P_2 is smaller than P_1 , pressure loss takes place in the cryocooler. That is, the decrease of the pressure ratio means the increase of pressure loss. This loss causes temperature rise and reduction of cooling power. We think that the regenerator causes the pressure loss.

The temperature distribution of a regenerator is shown in Fig. 5. The origin of the horizontal axis of the figure corresponds to the position of the higher temperature side of regenerator, and 80 mm its lower temperature side. For #150, #200 and #250 meshes, a gradient of the temperature was almost constant as a function of a position. But for #350 and #400, temperature was almost constant up to the middle of the regenerator, and then fell down.

The following results are for the regenerators made by stacking mixed meshes. Ideally, the capability of the regen-

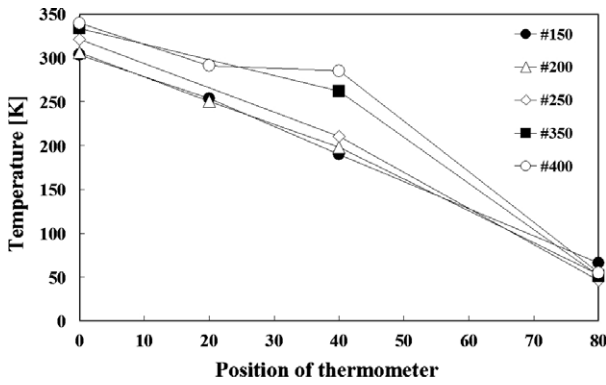


Fig. 5. Temperature distribution of the regenerator.

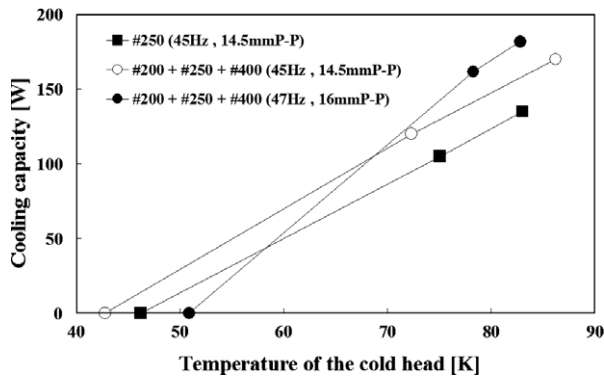


Fig. 6. Cooling capacity vs. temperature of the cold head.

erator constructed with the larger number mesh is higher. But, pressure loss becomes large as increasing the meshes, as shown in Fig. 4. Therefore, the small number mesh was placed in the higher temperature region and the large

number mesh in the lower temperature region. The performance of cooling capacity with 3 kinds of meshes is shown in Fig. 6. The result for #250 mesh regenerator is also shown for comparison. By stacking mixed meshes the higher cooling capacity was obtained rather than by stacking one kind of meshes. The highest performance was obtained in the regenerator with #200, 250 and 400 meshes; the cooling capacity of 148 W at 80 K. Furthermore, when the condition was changed into driving frequency of 47 Hz and the piston displacement of 16 mm P-P, the higher performance was obtained; the cooling capacity of 169 W at 80 K under power consumption of 4 kW.

4. Conclusion

In this work, the effects of the mesh size on cooling performance have been studied. To optimize the performance, several kinds of mesh number were stacked in the regenerator. Then the small number mesh was placed for the high temperature region of the regenerator and the larger number mesh for the low temperature. With one of these regenerators we have obtained the cooling capacity of 169 W at 80 K under electric input power of 4 kW.

References

- [1] C.M. Hargreaves, Elsevier Science Publishers, 1991, p. 94.
- [2] H.O. McMahon, Adv. Cryo. Eng 5 (1960) 354.
- [3] W.E. Gifford, R.C. Longworth, J. Eng. Ind 63 (1964) 264.
- [4] W.E. Gifford, R.C. Longworth, Adv. Cryo. Eng. 10 (1965) 69.
- [5] K. Oshima, Y. Matsubara, T. Kubo, Cryo. Eng, Japan 3 (1968) 72.
- [6] T.W. Bradshaw, J. Delderfield, S.T. Werreu, G. Davey, Adv. Cryo. Eng. 31 (1986) 801.
- [7] S.W. Zhu, S.L. Zhou, N. Yoshimura, Y. Matsubara, Cryo 9 (1997) 269.

Preparation of Carbon Nanofiber Emitters for Field Emission Display using Organic Thin Films

Masato Yoshikuni*, Shinji Ide, Nobuyuki Iwata and Hiroshi Yamamoto

College of Science & Technology, Nihon University

Funabashi-shi, Chiba 274-8501, Japan

Fax: 81-47-469-5457, e-mail: 2005_yoshikuni@yamanoya.eccs.cst.nihon-u.ac.jp

The purposes of this work are to prepare a low density carbon nanofiber (CNF) emitter by a spray spreading method and to investigate the performance of field emission. A sprayed paste was prepared with organic solution of tetrahydrofuran and also with binders of Au paste and Polycarbonate. The used CNF were massively synthesized by a thermal chemical vapor deposition and were burned to eliminate amorphous carbon and catalyst. The diameter of the CNF was about $0.1 \mu\text{m}\phi$. Two types of CNF were studied with the length of *ca.* $10\sim 20 \mu\text{m}$ (normal-CNF) and *ca.* $1.5 \mu\text{m}$ (cut-CNF). In the normal-CNF emitter the current density at $10 \text{V}/\mu\text{m}$ was about $1.4 \text{mA}/\text{cm}^2$ with an electric field enhancement factor β of about 1000, while $0.08 \text{mA}/\text{cm}^2$ with β of 4500 in the cut-CNF emitter. It was confirmed that the isolated CNF do play an important role as effective emitter sites.

Key words: carbon nanofiber (CNF), spray spreading, CNF emitter, field emission properties, Field Emission Display.

1. INTRODUCTION

We have been studying a novel low voltage Field Emission Displays (LV-FED) by using organic luminescence films as a phosphor. A stacking structure of $\text{Alq}_3/\alpha\text{-NPD}/\text{CuPc}$ on ITO substrate was irradiated by thermally activated electrons with the emission current density of *ca.* $1 \text{mA}/\text{cm}^2$ [1,2]. Observed luminescence was, however, quenched quickly. It was found that the quench was caused by an accumulation of electrons at the interface of $\text{Alq}_3/\alpha\text{-NPD}$ due to insufficient electric field applied in the organic stacking layers. We have expected that the issue will be overcome by adopting carbon nanofiber (CNF) electron emitters to shorten the distance between the electrodes [3]. In this work we tried to prepare CNF emitters which achieve an emission current density of several mA/cm^2 .

Recently screen-printing CNT emitter with accumulated many CNT layers have been vigorously developed for application to FED. The efficiency of emission is improved by adjusting a distance between isolated CNT. It was suggested that the optimum density of CNT to apply effectively the electric field is about $1.0 \times 10^7 \text{cm}^{-2}$ in the case of $1 \mu\text{m}$ -long CNF

which are dispersed in the distance of $3 \mu\text{m}$ [4]. Though a low density CNT emitter is desirable, it is difficult to prepare such an emitter by a conventional screen-printing method. The purpose of this study is to prepare a low density CNF emitter by a spray spreading method. Then the CNF emitter is also on investigated its field emission properties from a point of view of field enhancement factor β and a number of CNF as an emission site.

2. EXPERIMENTAL

We used multi-wall carbon nanofibers (MWCNF) which were massively produced by Showa Denko Co. Ltd. The CNF were typically synthesized from mixed solution of ferrocene, thiophene and benzene by thermal chemical vapor deposition at *c.a.* 1000°C . The obtained CNF were burned out above 2500°C for 30 min to eliminate amorphous carbon and catalysts. The size of the CNF powders was typically about $0.1 \mu\text{m}\phi$ in a diameter and *ca.* $20 \mu\text{m}$ in a length (named as normal-CNF). On the other hand the CNF with short length of *ca.* $1.5 \mu\text{m}$ in a length (named as cut-CNF), which were prepared from

Table 1: The preparation conditions of CNF emitters.

Organic Solvent	THF
CNF powder (wt %.)	Cut or Normal-CNF (0.1)
Dissolution	Sonication for 24 h. Stirring for 30 min. at 70°C
Binder (wt %.)	Au-past (1.0)
Dispersion solvent (wt %)	PC (10)
Deposition by spray	0.1MPa , 400°C
Annealing	Baking at 400°C

the normal-CNF by a fragmentation process, were also used.

The preparation conditions of CNF emitters are summarized in Table 1. CNF were tetrahydrofuran (THF) and sonicated for 24 h. Au paste and polycarbonate (PC) were mixed and stirred for 30 min at 70°C. As binders Au paste was used to increase conductivity [5] and PC to improve distribution of CNF [6]. The CNF paste was loaded into a hand-spray gun and was sprayed with N₂ gas at 0.1 MPa on ITO substrates heated at 400°C. The size of the ITO substrate was 10×20 mm². The distance between the substrate and the spray-nozzle was 200 mm. The spray for one second was repeated taking care not to cool the substrate temperature at the set temperature. After spraying specimens were baked at 400°C for 30 min to remove organic solution in the paste.

A surface morphology of the CNF emitter was observed by scanning electron microscopy (SEM). Measurement of emission current was carried out in a vacuum chamber in 3×10⁻⁶ Torr at room temperature. The distance between a copper plate (anode) and CNF (cathode) was ca. 50 μm. The measured emission area was 5×5 μm². The emission current-voltage (I-V)

characteristics were analyzed by using the Fowler-Nordheim (F-N) equation for the field emission.

3. RESULTS AND DISCUSSION

Fig. 1 shows the SEM images of CNF films added the binder with two different types of CNF ((a), (b) normal-CNF; (c), (d) cut-CNF). In Fig. 1(a) bundles of CNF with the size of 30-100 μmφ were observed, where CNF bundles (i), a binder (ii) and surfaces of ITO substrate (iii) were confirmed. Many CNF bundles were separated by a distance of 40-150 μm, while isolated CNF were quite few. The most of surfaces of ITO substrate were covered by Au film. Figure 1(b) shows the shape of a CNF bundle, where bent CNF became tangled with one another each other and the density of CNF was very high. It is not expected that an electric field is effectively applied on each the tip of CNF, even though so many tips of CNF protruded from the bundle.

In Figs. 1(c) and (d) CNF bundles were not found on the substrate, where grains of the binder (i), surfaces of ITO substrate (ii), a binder (iii), were observed. The grains with size of 10-60 μmφ were distributed randomly separated from one another. The surfaces of ITO substrate were covered by Au film and CNF were not included in the grain. In Fig. 1(d) straight CNF

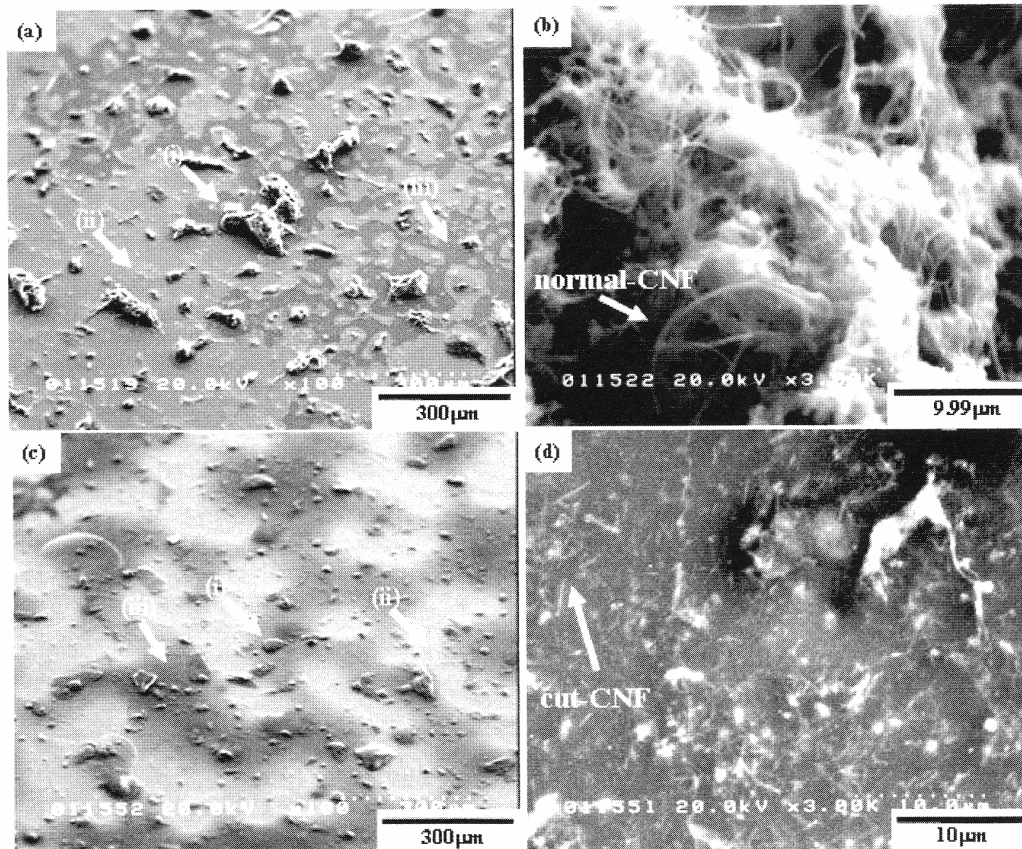


Fig. 1: The SEM images of the CNF films added binders of Au paste and PC with using two different CNF: normal-CNF (a), (c) and cut-CNF (b), (d).

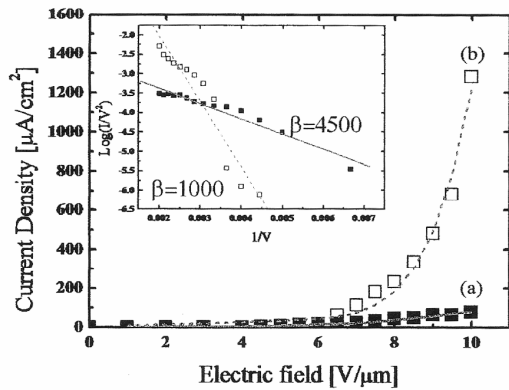


Fig. 2: Emission current versus applied voltage of CNF emitter with different two CNF (cut-CNF (a) and normal-CNF (b)). The inset shows the data plotted as $\log(I/V^2)$ versus $1/V$ (Fowler-Nordheim plot). The solid and dotted lines are fitting lines with the evaluated value of β .

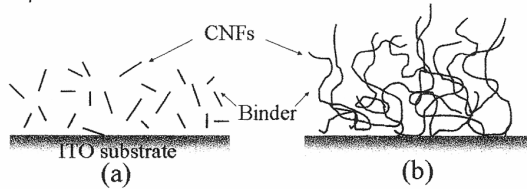


Fig. 3: Schematic cross sections of CNF films prepared with cut-CNF (a) and normal-CNF (b).

were isolated and were buried in the Au film, and a few tips of CNF protruded from the surface.

Fig.2 shows the emission current versus applied voltage (I-V) characteristics of the CNF emitter prepared by cut-CNF (a) and normal-CNF (b), where Au paste and PC were added as binders. The inset is the data plotted as $\log(I/V^2)$ versus $1/V$ (Fowler-Nordheim plot). A turn-on electric field E_t was defined as the electric field at which the observed current attains to 1% of the value obtained at $10 \text{ V}/\mu\text{m}$. The E_t was about $6 \text{ V}/\mu\text{m}$ in the both specimens and the current density at $10 \text{ V}/\mu\text{m}$ in the specimen of cut-CNF and normal-CNF was 0.08 and $1.4 \text{ mA}/\text{cm}^2$, respectively. On the other hand, the field enhancement factor β in the F-N equation was estimated according to the equation (1). Since the current observed includes the both emission current and conduction current, we separated the term of emission current,

$$I = aJ + (1-a)I' = a \frac{A(\beta E)^2}{\phi} \exp\left(-\frac{B\phi^{3/2}}{\beta E}\right) + (1-a)\frac{V}{R} \quad (1)$$

Where I is the current density obtained, J is emission current density in (F-N) equation [7], I' is conduction current obeying the Ohm's law, $A=1.56 \times 10^{-6} \text{ AeV}^2$, $B=6.83 \times 10^7 \text{ eV}^{-3/2} \text{ Vcm}^{-1}$, ϕ is work function of $4.85\text{-}5.05 \text{ eV}$ [8], a is a variable number ($0 < a < 1$), R is the resistance, and E is applied electric field. We assume that the work function of CNF was 5.0 eV equal to that of graphite. From fitting the data, the value of β

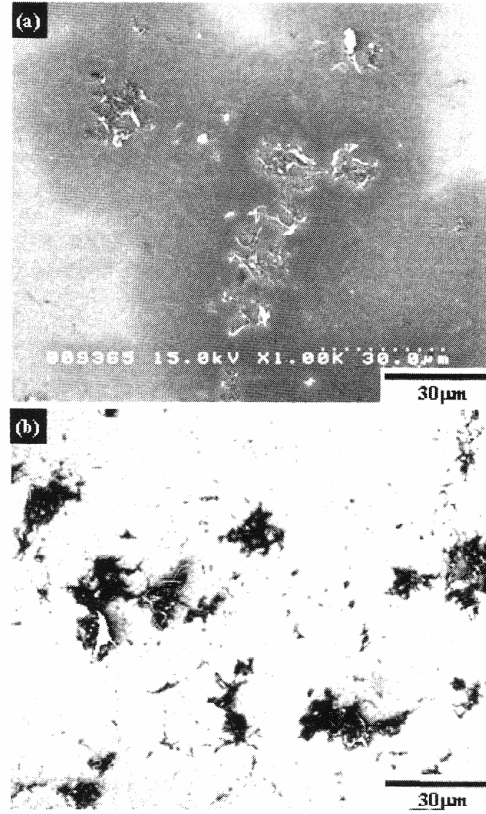


Fig. 4: SEM images of the CNF film with different numbers of isolated CNF. The densities of isolated CNF were $3.5 \times 10^5 \text{ cm}^{-2}$ (a) and $1.2 \times 10^7 \text{ cm}^{-2}$ (b).

evaluated was 1000 and 4500 for the specimen of normal-CNF and cut-CNF, respectively. The rate of emission current was evaluated by a , of which the value was 95% in normal-CNF and 84% in cut-CNF.

Fig. 3 shows schematic diagrams of cross section of CNF films prepared with cut-CNF (a) and normal-CNF (b). Most of cut-CNF was buried in the binders. Since cut-CNF with short length hardly pass through binder surfaces, the number of emission sites was small and high emission current was not obtained. Normal-CNF with long length and bent shape protruded from binders. So, many tips of CNF worked as field emission sites and high current density was obtained. Cut-CNF isolated resulted in, however, the increase of the value of β because of effective electric field concentration caused from their shapes.

Since the two kinds of CNF (normal- and cut-CNF) were used, it was not clear from the result in Fig1 (a) ~ (d) whether isolated CNF did play an important role or not. The cut-CNF was not studied because they were not so long and did not become bundles comparing with the normal-CNF. The number of isolated CNF was increased by using the cut-CNF. Then two types of CNF

emitters were prepared to make clear the role of isolated CNF by using same cut-CNF and/or changing only the number of isolated CNF.

The SEM images of CNF emitters with different number of isolated CNF are shown in Figs. 4(a), (b). The density of isolated CNF was $ca. 3.1 \times 10^5 \text{ cm}^{-2}$ in Fig. 4(a) and $ca. 1.2 \times 10^7 \text{ cm}^{-2}$ in Fig. 4(b), respectively. The number and the size of bundles were almost same in the both specimen. Fig. 5 shows I-V characteristics measured in the two CNF emitters in Fig.4 and the inset is the F-N plot. The current densities at $10 \text{ V}/\mu\text{m}$ in (b) was larger than in (a). The value of β in (b) was 2500 and larger than in (a), 500. It was clear that the number of isolated CNF was larger in the CNF emitter with the high electronic emission performance. It was confirmed that isolated CNF play an important role as emitter sites [9] and/or the CNF emitter with high b was prepared in the structure with isolated CNF dispersed.

4. CONCLUSION

A low density CNF emitter was prepared by a spray spreading method. The low density CNF emitter was investigated about its field emission properties from a point of view of β and the number of b and the number of field emission sites. From the normal-CNF emitter the current density of $1.4 \text{ mA}/\text{cm}^2$ @ $10\text{V}/\mu\text{m}$ was obtained. The cut-CNF emitter gave comparatively small current density, $80\mu\text{A}/\text{cm}^2$ at $10\text{V}/\mu\text{m}$ and the β of 4500 was, however, much larger than that of the normal-CNF emitter, 1000. It was confirmed that the isolated CNF played an important role as effective emitter sites. Conclusively a current density of mA/cm^2 order was obtained from the CNF emitter prepared by a spray spreading method. We will apply the emitter to a novel luminescence device composed with organic light emitting diode films.

REFERENCES

- [1] K. Onozuka, N. Iwata and H. Yamamoto, *Int. J. Mod. Phys. B* **16** (2002) 4445.
- [2] Y. Hata, T. Ichinose, N. Iwata and H. Yamamoto, *Trans. Mate. Res. Soc. Jpn.* **30** (2005) 175.
- [3] B. J. Chen, W. Y. Lai, Z. Q. Gao, C. S. Lee, S. T. Lee and W. A. Gambling, *Appl. Phys. Lett.* **75** (1999) 4010.
- [4] J. Li, W. Lei, X. Zhang, and X. Zhou, *Appl. Surf. Sc.*, **220** (2003) 96.
- [5] t. j. Vink, M. Gillies, J. C. Kriege, and H. W. J. J. van de Laar, *Appl. Phys. Lett.*, **83** (2003)3552.
- [6] E. Sato, T. Takahashi, and K. Koyama, *TANSO*, **209** (2003) 159.
- [7] R. H. Fowler, L. W. Nordheim, *Proc. R. Soc. Lond., Ser., A* **119** (1928) 173.
- [8] M. Shiraishi, M. Ata, *Carbon*, **39** (2001) 2591.
- [9] N. Iwata et al, *Materials Science and Engineering*, (2006). (In press)

(Received January 18, 2007; Accepted February 20, 2007)

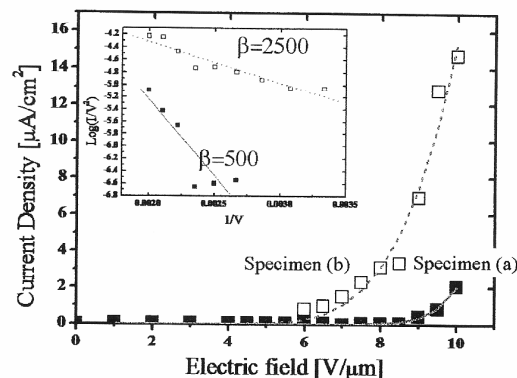


Fig.5: Emission current versus applied voltage in the different CNF film in fig.4 (a) and (b). The inset is the Fowler-Nordheim plot. The solid and dotted lines are fitted lines with the evaluated value of β .

Preparations of magnetoelectric thin films for superconducting devices

N. Iwata *, T. Asada, K. Nagase, T. Yamada, H. Yamamoto

Department of Electronics and Computer Science, College of Science and Technology, Nihon University, 7-24-1 Narashinodai, Funabashi-shi, Chiba 274-8501, Japan

Received 30 October 2006; accepted 9 February 2007
Available online 26 May 2007

Abstract

Representative magnetoelectric (ME) Cr_2O_3 thin films were grown on *R*-cut sapphire and $\text{SrTiO}_3(100)$ substrate in order to integrate with high temperature superconductor oxides. The replacement of a base current and stabilization of I_C spread for single flux quantum device is expected. Highly oriented Cr_2O_3 thin film grew on sapphire at 550 °C by off-axis DC–RF hybrid magnetron sputtering method with two-in. Cr metal target. The surface was composed of coalesced rectangular grains, the surface roughness R_a of which was 1.9 nm. Estimated induced magnetic field with electric field applied of 0.24 MV/cm was 1.0 G around 40 K.

© 2007 Elsevier B.V. All rights reserved.

PACS: 68.55.–a; 81.15.–z; 81.15.Cd

Keywords: Magnetoelectric effect; Cr_2O_3 ; Single flux quantum; Thin film

1. Introduction

We pay attention to apply the magnetoelectric (ME) materials of single phase compounds to single flux quantum (SFQ) device integrated by high critical temperature (high- T_c) superconductors [1–4]. The ME effect is defined as the dielectric polarization of a material in an applied magnetic field or an induced magnetization in an external electric field [1–4]. The performance of the SFQ device is featured as a high-speed (over 100 GHz) and low consumption (less than 100 nW/gate) following Si digital devices. However, increasing integration degree, large amount of base current is required, which give rise to uncontrollable operation due to accompanying magnetic field. In addition, to reduce the fluctuation of critical current (I_C) and to stabilize the device operation, working temperature is limited less than 40 K.

As shown in the Fig. 1, we propose a novel element how the ME material is embedded in a SFQ device. Since the ME material is grown to generate a base current, the base current is localized and then error operations could be reduced. It is expected that a base current in a SFQ device is replaced by the ME materials. The electric power loss from a current source is excluded. Furthermore, considering critical current I_C of the Josephson junction is modulated by the magnetic field penetrating the junction area, I_C spread of the junctions could be reduced by the induced magnetic field from the ME film. We expect that a larger-scale circuit is achievable by the induced and localized magnetic field from ME materials integrated with SFQ devices.

In this paper, we have focused on an antiferromagnetic insulator Cr_2O_3 which is a representative oxide among ME single phase compounds. Cr_2O_3 has the linear ME susceptibility of α_{xx} , α_{yy} and α_{zz} and the others are zero [1–4]. Magnetic field is induced along the direction of electric field applied. Since the ME effect is derived from a magnetic superexchange interaction, highly oriented ME films are claimed on SrTiO_3 (STO), MgO, sapphire, etc., to integrate with high- T_c superconductors.

* Corresponding author. Tel./fax: +81 47 469 5457.
E-mail address: iwata@ecs.cst.nihon-u.ac.jp (N. Iwata).

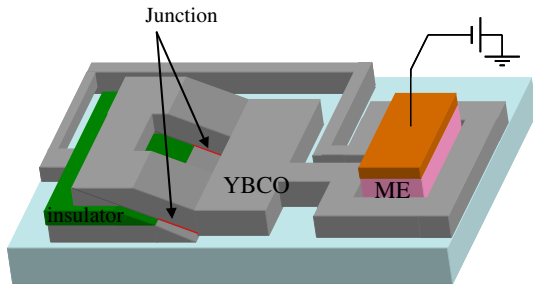


Fig. 1. Schematic image of a part of the SFQ device with ME material we propose. Induced magnetic field from the ME film generates the shielding current along the high- T_c superconductor. Shielding current could be a base current for operation of SFQ device.

2. Experimental

Cr_2O_3 films were grown by off-axis DC–RF hybrid magnetron sputtering method with two-in. Cr metal target on the substrates of *R*-cut sapphire and STO with CeO_2 buffer layer. Substrates surface of sapphire was etched by HF acid for 10 s ($\text{HF}:\text{H}_2\text{O} = 1:7$) and then annealed at 1000 °C for 12 h in air in advance. For Cr_2O_3 growth substrate temperatures, DC current, RF power and sputtering gas were 300–630 °C, 0.04 A, 100 W and 0.26 Pa ($\text{Ar}:\text{O}_2 = 4:1$), respectively. CeO_2 buffer layer was deposited by on-axis RF magnetron sputtering method with pressed CeO_2 powder at 380 °C. The substrate was 0.5 wt.% Nb-doped STO(100). A post-annealing was carried out at 1000 °C for 4 h in air prior to growth of Cr_2O_3 .

The X-ray diffraction (XRD) 2θ – θ scans from 5° to 90°, using Rigaku RAD-C system with $\text{Cu K}_{\alpha 1}$ and $\text{K}_{\alpha 2}$ radiation generated with a tube power of 40 kV and 30 mA, examined the grown films. The diffraction area was always same with divergence slit of $1/2^\circ$ and sample size of $5 \times 10 \text{ mm}^2$. The surface morphology was observed in a dynamic force mode by an atomic force microscopy (DFM, Seiko Instruments Inc. SII: NanoNavi Station).

3. Results and discussion

Fig. 2a shows a XRD pattern of Cr_2O_3 film grown on *R*-cut sapphire substrate at 500 °C and Fig. 2b is the magnified pattern around $\text{Cr}_2\text{O}_3(1-102)$ Bragg reflection at various substrate temperatures from 300 °C to 600 °C. Bragg reflections from *R*-plane of Cr_2O_3 were clearly observed just below those of sapphire substrate in 2θ . The peak indicated by open-triangle was probably due to oxygen deficient of substrate. Any other peaks did not appear in XRD patterns. The lattice spacing was 0.363 nm similar to that of substrate. As shown in Fig. 2b, peak intensity was the highest at 500 °C with shoulder at right hand side of the peak indicated by arrow. Peaks became decreasing in intensity and broader in films grown 300 °C, 400 °C and 600 °C. Fig. 3 shows the full width at half maximum (FWHM) of rocking curve for $\text{Cr}_2\text{O}_3(1-102)$ as a function of substrate temper-

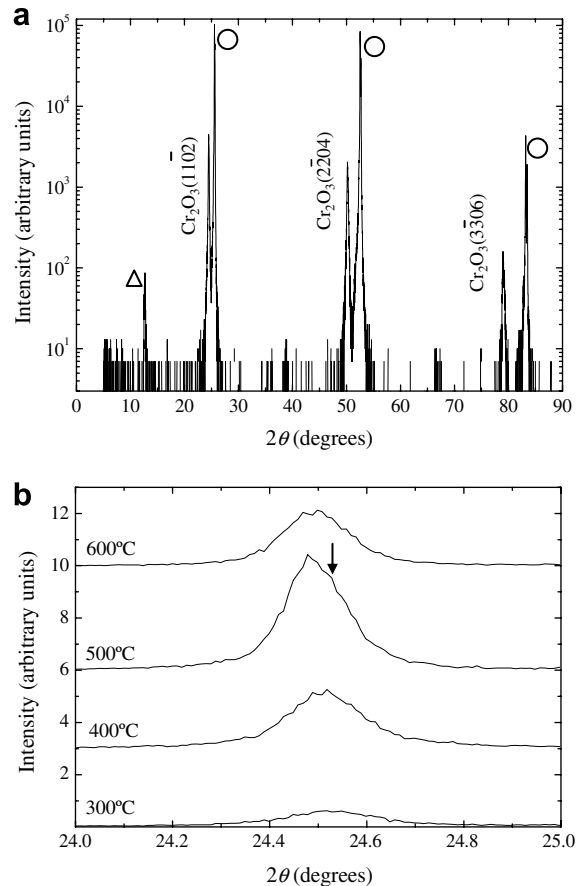


Fig. 2. XRD patterns of Cr_2O_3 film grown at (a) 500 °C on *R*-cut sapphire and (b) magnified images around $\text{Cr}_2\text{O}_3(1-102)$ Bragg reflection at various substrate temperature. Open circles and triangle are come from the substrate. Bragg reflections of Cr_2O_3 thin film were clearly observed.

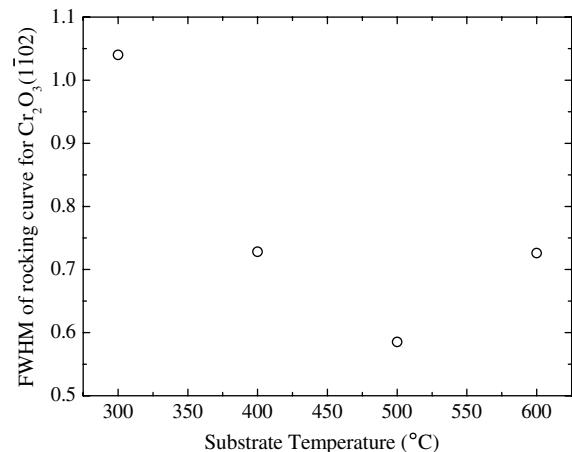


Fig. 3. The FWHM of rocking curve for $\text{Cr}_2\text{O}_3(1-102)$ as a function of substrate temperature. At 500 °C the sharpest peak was obtained.

ature. At 500 °C the rocking curve was 0.58° and the sharpest.

Generally the FWHM of Bragg reflections in 2θ – θ examination depends on a film thickness in particular less than 500 nm and a fluctuation of a lattice spacing. Since

the thickness of the grown film was constant approximately 190 nm in these experiments, the FWHM is a function of only the fluctuation of the $\text{Cr}_2\text{O}_3(1-102)$ lattice spacing. Considering the appearance of the shoulder at the right hand side of the $\text{Cr}_2\text{O}_3(1-102)$ Bragg reflection for the film grown at 500 °C, which was derived from the separation of the peak by $K_{\alpha 1}$ and $K_{\alpha 2}$ of different X-ray wave lengths, the fluctuation of the lattice spacing was reduced and then highly oriented film was obtained. Although a lattice mismatch is +4.01% along the $[11-20]$ direction and is +4.34% along the $[-1101]$ direction, an expected compressive stress in-plane is seemed to be released from the result of the same lattice spacing to the bulk value.

Figs. 4 and 5 show the surface images of the Cr_2O_3 films with the size of $2\ \mu\text{m} \times 2\ \mu\text{m}$ and line profiles of those images. In Table 1, grain sizes as a function of substrate

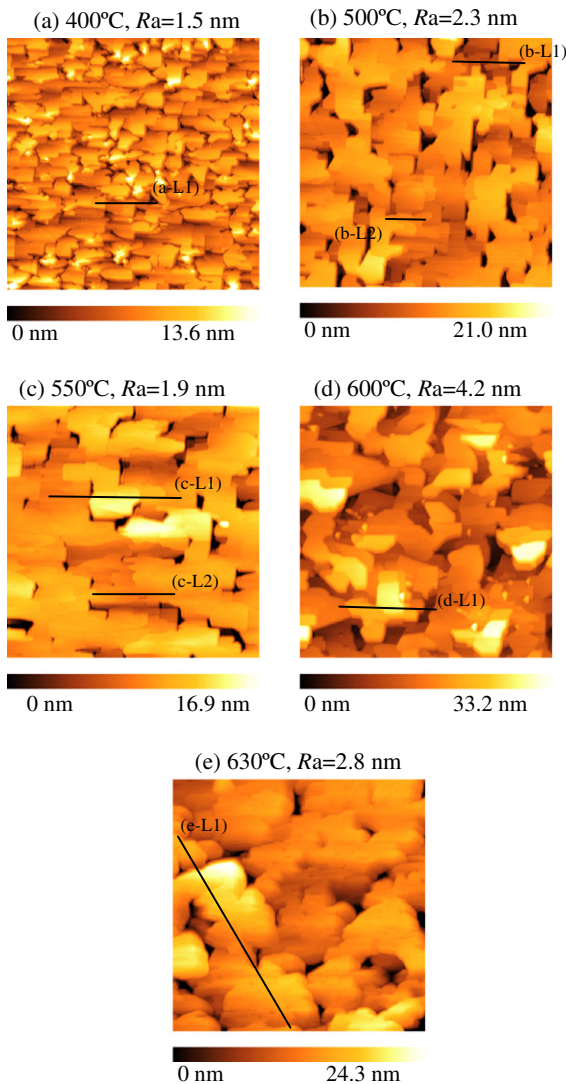


Fig. 4. Surface images with $2 \times 2\ \mu\text{m}^2$ of Cr_2O_3 thin films grown at (a) 400 °C, (b) 500 °C, (c) 550 °C, (d) 600 °C and (e) 630 °C. Scale bars were attached below each image. The film grown at (c) 550 °C showed the smoothest surface, the roughness R_a of which was 1.9 nm. Rectangular grains with the size of $200 \times 200\text{--}600\ \text{nm}^2$ coalesced throughout the surface except for the grains separated by deep grain boundaries.

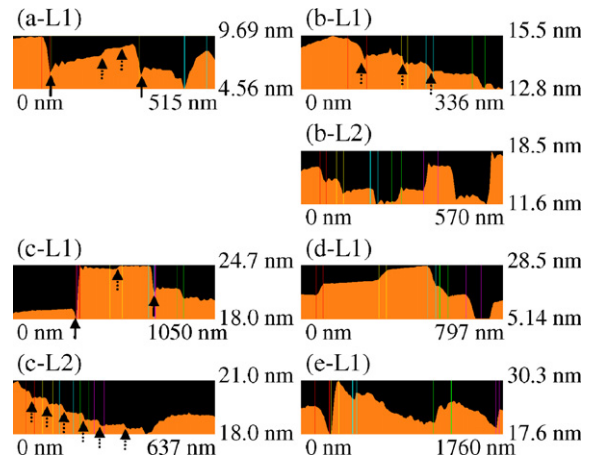


Fig. 5. Line profiles related to the index of the surface images of Fig. 4. Solid arrows indicate the difference in height at the grain boundary where coalescence did not take place. Dotted arrows indicate the steps composed of multiples of 1/3 unit cell along the $[1-102]$ direction inside one grain.

Table 1
Substrate temperature vs. grain size

Sub. temp. (°C)	Grain size (nm × nm)
400	100 × 100–200
500	100 × 100–500
550	200 × 200–600
600	400 × 400

temperature are summarized. Rectangular grains were mainly observed with the size of $100 \times 100\text{--}200\ \text{nm}^2$ at 400 °C in Fig. 4a. The difference in height between grains was approximately 3.5 nm indicated by solid arrows in Fig. 5a-L1. One grain contained 2 or 3 steps at the surface, indicated by dotted arrows, with the height of 0.3–0.9 nm, which was integer multiple of 1/3 unit cell along the $[1-102]$ direction, 0.363 nm. At 500 °C larger square grains with the size of $100 \times 100\text{--}500\ \text{nm}^2$ were observed and those grains were coalesced in Fig. 4b. In one grain the steps of 1–3 integer multiples of 1/3 unit cell was also observed as shown in Fig. 5b-L1 indicated by arrows. The grains growing from different nucleus sites, where coalescence did not occur, had a difference of 2–10 nm in height as shown in Fig. 5b-L2 and sometimes deep grain boundaries were formed. The deepest depth of the boundaries was 34 nm. At 550 °C as shown in Fig. 4c rectangular grains became larger and longer along a particular direction and the smoothest surface with the surface roughness R_a of 1.9 nm. Almost all of the grains coalesced except for the grains separated by deep grain boundaries as shown in Fig. 5c-L1 indicated by arrows. The density of deep boundaries decreased compared with that of Fig. 4b. As indicated by dotted arrows in Fig. 5c-L1 and c-L2, steps of 1/3 unit cell were clearly observed in one grain. Film growth looked like 2-dimensional island. At 600 °C although the largest grains were obtained, bunching steps, the value of which was approximately 5 nm, were observed as shown in Figs. 4d and 5d-L1.

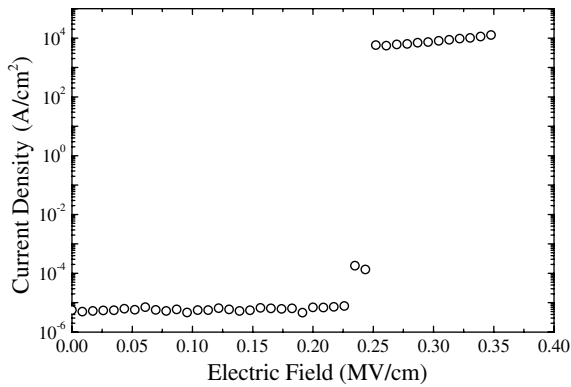


Fig. 6. I - V characteristic of $\text{Cr}_2\text{O}_3/\text{CeO}_2$ bilayered film on STO substrate. Below 0.24 MV/cm the film was insulating.

The surface smoothness was degraded down to the R_a of 4.2 nm due to the bunching steps. The surface of the terrace was so flat that even steps of $1/3$ unit cell did not appear. In addition, spherical grains were also observed with the size of $\varnothing 40 \mu\text{m}$. At 630°C as shown in Figs. 4e and 5e-L1 film 3-dimensionally grew without a regularity in grains.

As the substrate temperature is increased, the migration length increases and the density of nucleus sites as well as of grains decrease. At 400°C where coalescence did not take place, the surface was covered by many grains and boundaries with the height of 3.5 nm due to the short migration length. However at 500°C where start to coalesce but not to obtain sufficient migration length to be large grain, the deep grain boundary was expected to be introduced. As increasing substrate temperature up to 550°C , increased migration length led to larger grain and then the density of deep grain boundary was reduced. At 500 – 550°C , the terrace in one grain was composed of several steps of $1/3$ unit cell at most, indicating the 2-dimensional island growth. The unit of $-\text{O}-\text{Cr}-\text{O}-\text{Cr}-\text{O}-$, corresponding to the height of $1/3$ unit cell, stacks along the $[1-102]$ direction in Cr_2O_3 single crystal with rhombohedral structure. In the highly oriented Cr_2O_3 films, it is reasonable that the integer multiples of $1/3$ unit cell appear because of the repulsive force between O^{2-} ions at the interface of stacked $1/3$ unit cell. Above 600°C despite sufficient migration length to be large grain, Cr_2O_3 is expected to be decomposed due to deficient of oxygen, demonstrated by the results of XRD and the present of spherical grains.

Fig. 6 is a leakage current density as a function of electric field (I - V) of a bilayered film of $\text{Cr}_2\text{O}_3/\text{CeO}_2//$

STO(100) observed at room temperature. The thickness of Cr_2O_3 and CeO_2 was 220 nm and approximately 10 nm, respectively. The diameter of measurement area was $\varnothing 0.45 \text{ mm}$. From the XRD result Cr_2O_3 film was oriented along the c -direction normal to the substrate surface. Leakage current rapidly increased above 0.24 MV/cm indicating that the Cr_2O_3 film works as a ME material below the electric field.

We estimated the induced magnetic field tentatively with the obtained data. Assuming that the ME coefficient of Cr_2O_3 along the c -direction around 40 K α_{zz} is 10^{-4} (in CGS – gauss unit) and the demagnetizing field is neglected, induced magnetic field is estimated at 1.0 G [1–4]. For example, to obtain 0.5 mA by a shielding current, which is representative for base current in SFQ device, with $100 \mu\text{m}^2$ and 100 pH superconducting loop, 5 G is required. We expect to achieve such the value by optimizing the growth condition of CeO_2 for epitaxial growth of Cr_2O_3 on it.

4. Conclusion

We propose to apply the ME materials of single phase compounds to the SFQ device as the replacement of a base current and stabilization of I_c spread. The ME material generates induced magnetic field with electric field applied. As a representative ME material, Cr_2O_3 thin films were grown on R -cut sapphire and STO substrates in order to integrate with high- T_c superconductors. At 550°C , 0.26 Pa and a flow rate of $\text{Ar}:\text{O}_2 = 4:1$, highly oriented Cr_2O_3 thin films grew on sapphire substrate, the surface of which was composed of coalesced rectangular grains with the size of 200×200 – 600 nm^2 . The surface roughness R_a was 1.9 nm. Estimated induced magnetic field from the result of $\text{Cr}_2\text{O}_3/\text{CeO}_2//\text{STO}$ was 1.0 G around 40 K. To eliminate the induced magnetic flux, shielding current is expect to flow superconducting circuit, which is substituted for a base current of SFQ device by a current source.

References

- [1] K.K. Likharev, K. Semenov, IEEE Trans. Appl. Supercond. 1 (1991) 3.
- [2] M. Fiebig, J. Phys. D: Appl. Phys. 38 (2005) R123.
- [3] H. Wigelmann, A.G.M. Jansen, P. Wyder, J.P. Rivera, H. Schmid, Ferroelectrics 162 (1994) 141.
- [4] N. Iwata, K. Matsuo, N. Ootsuka, H. Yamamoto, Mat. Res. Soc. Symp. Proc. 811 (2004) 425.

Fabrication of Magnetolectric Cr₂O₃ Films for Application Single Flux Quantum Device

Takeshi Asada, Kenjiro Nagase, Takayuki Yamada, Nobuyuki Iwata and Hiroshi Yamamoto
College of Science & Technology Nihon University (CST), 7-24-1 Narashinodai, Funabashi-shi, Chiba 274-8501
Fax: +81-47-469-5457, e-mail: 2005_asada@yamanova.ecs.cst.nihon-u.ac.jp

Thin films of magnetolectric (ME) materials are expected to be applied to novel superconducting devices as voltage-controlled magnetic/current sources and gates. As a representative ME material Cr₂O₃ films were prepared on *R*-cut sapphire substrates by *DC-RF* hybrid magnetron sputtering. Strong Bragg diffraction peaks (n 0 $-n$ $2n$) from Cr₂O₃ with a trigonal phase were observed. Then full width at half maximum of rocking curves of (10-12) was 0.58degrees in the film deposited on substrate of 500°C substrates. The surface morphology of the film prepared at 550°C was very smooth with a step and terrace structure. The steps height was same the lattice spacing of Cr₂O₃ (10-12) planes. The Cr₂O₃ films deposited on Nb-SrTiO₃ (100) with CeO₂ buffer layers revealed *a*-axis or *c*-axis oriented growth. The CeO₂ buffer layer proceeded the growth of Cr₂O₃. A leakage current through the Cr₂O₃ film was suppressed less than 10⁻⁵A/cm² below the electric field of 0.24MV/cm.

Key words: magnetolectric effect, Cr₂O₃, Nb-STO, CeO₂ buffer, epitaxial growth

1. INTRODUCTION

A magneto-electric effect is defined as an appearance of magnetic fields induced by electric fields. When electric fields are applied, the deviation of \pm ions in the crystal takes place and results in changes of magnetic superexchange interactions and magnetic fields appear outside [1,2]. As a representative ME material antiferromagnetic insulator Cr₂O₃ has been studied [3]. Since magnetic fields are induced along the direction of electric fields applied, the orientation and crystallinity of the ME material are determining factors

It is expected that thin films of ME materials are applied to novel superconducting Josephson devices with voltage-control type of magnetic or current sources and gates. Fig. 1. shows the schematic example of a single flux quantum (SFQ) device fabricated by both cuprate high temperature superconductors (HTS) and ME thin films. When electric fields are applied to the ME thin film, magnetic fields are induced to generate shielding current in the superconductor loop including Josephson junctions. The novel circuit element enables a dispersed current source system for highly integrated SFQ circuits and also improves the performance of 100GHz class of high speed SFQ switching.

Most of HTS circuits have been prepared on cubic perovskite substrates, SrTiO₃(STO) or MgO. A crystal matching is not good between the substrate crystal and the trigonal Cr₂O₃. Cr₂O₃ films should be deposited on STO substrates buffered by cubic CeO₂ which has been studied for preparation of HTS thin films [4-7]. The purposes of this work are to optimize the substrate temperature for sputtered Cr₂O₃ films on *R*-cut sapphire (10-12) and to investigate the film growth on Nb-SrTiO₃ (STO) with CeO₂ buffer layers.

2. EXPERIMENTAL

Cr₂O₃ films were deposited by off-axis *DC-RF* hybrid magnetron sputtering from a Cr metal target with the

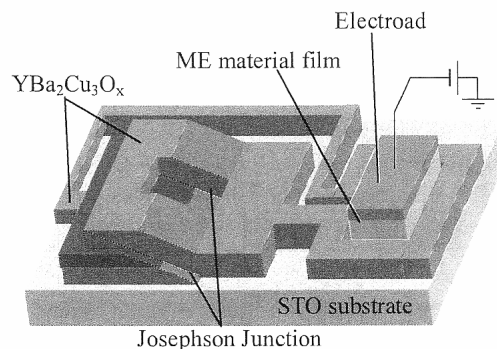


Fig. 1. Schematic novel HTS SFQ circuit as an application of ME material. Magnetic fields induced from the ME film generates base or shielding current in the Josephson junctions loop.

diameter of two-inch [8]. The typical growth conditions were as follow: substrate temperature (*T*_s) of 300~600°C, *DC* current of 0.04 A, *RF* power of 100 W and sputtering pressure of 0.26 Pa (Ar:O₂=4:1).

Substrates of *R*-cut sapphire single crystals (5 × 10mm²) were etched by HF(HF:H₂O=1:7) for 10 s before annealing at 1000°C for 12 hour in the air.

As a substrate, CeO₂ buffer layer was deposited by off-axis *RF* magnetron sputtering on Nb-STO(Nb 0.5wt%dope) and post-annealed at 500 or 1000°C in the air. Several CeO₂/Nb-STO substrates with different average roughness (*R*_a) were obtained and compared with the results for the Cr₂O₃ films growth.

The crystalline structure of the films was analyzed by X-ray diffraction (XRD: Rigaku RAD-C) with 2θ - θ scan from 5 to 90 degrees. Surface morphology was observed by an atomic force microscopy (AFM: Seiko Instruments Inc. Nanonavi-station).

3. RESULTS & DISCUSSION

3.1 Growth of Cr₂O₃ thin film on the R-cut sapphire

Fig. 2. shows the XRD pattern of Cr₂O₃//R-cut sapphire prepared at Ts=500°C. The open-circles peaks show the peaks from the sapphire substrate. All Bragg diffraction peaks were assigned to R-plane (n 0 -n 2n) of trigonal Cr₂O₃ phase and the substrate. The lattice spacing evaluated from the Cr₂O₃ (10-12) peak was 0.363nm same to that of bulk crystal. Fig. 3. shows the enlarged (10-12) peaks of the films deposited at Ts=300 ~ 600°C. Crystallization of the trigonal Cr₂O₃ phase was confirmed at Ts's above 300°C.

Fig. 4. shows the full width at half maximum (FWHM) of Cr₂O₃ (10-12) rocking curve. The smallest FWHM was 0.58 degrees in the film prepared at Ts=500°C, which revealed the superior crystal growth.

Since the inplane lattice parameter of R-planes of Cr₂O₃ is larger by about 4% than that of R-cut sapphire. The lattice spacing of Cr₂O₃ films are contracted in planes by internal compressive stress and are expanded perpendicular to substrate planes by tensile stress.

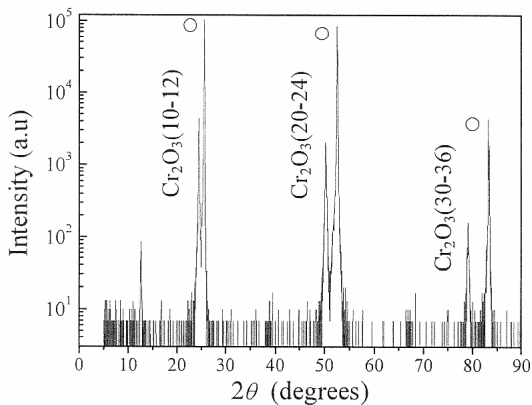


Fig. 2. XRD pattern of Cr₂O₃ film deposited on R-cut sapphire at Ts=500°C. Open circles show Bragg peaks from the substrate.

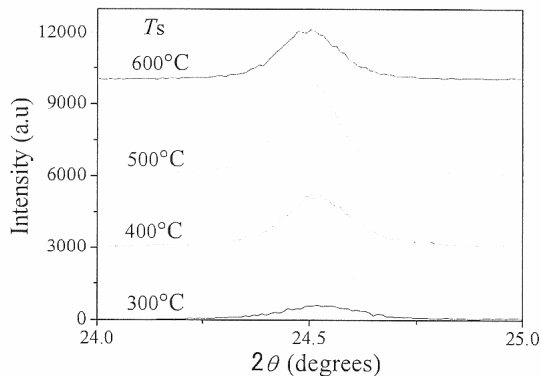


Fig. 3. Cr₂O₃ (10-12) Bragg peaks were observed in the films prepared on R-cut sapphire at Ts=300°C~600°C. The peak of the film deposited at 500°C was large and sharp.

From the results of XRD it was found that the lattice spacing of the film at Ts=500°C was almost same to that of the bulk and the internal stress was relieved.

Fig. 5. shows AFM surface images and line-profiles of Cr₂O₃ films prepared at various Ts's. In (a-1) at

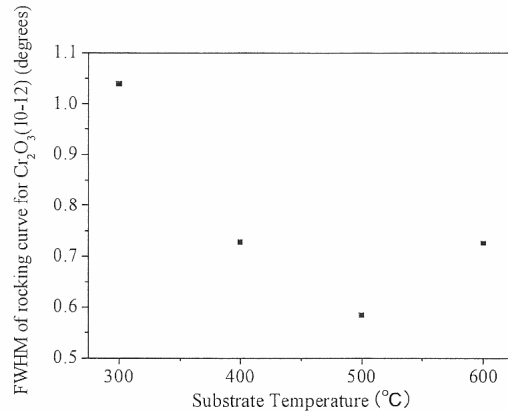


Fig. 4. FWHM of Cr₂O₃ (10-12) rocking curves of the films vs. Ts. The minimum value observed was 0.58degrees at Ts=500°C.

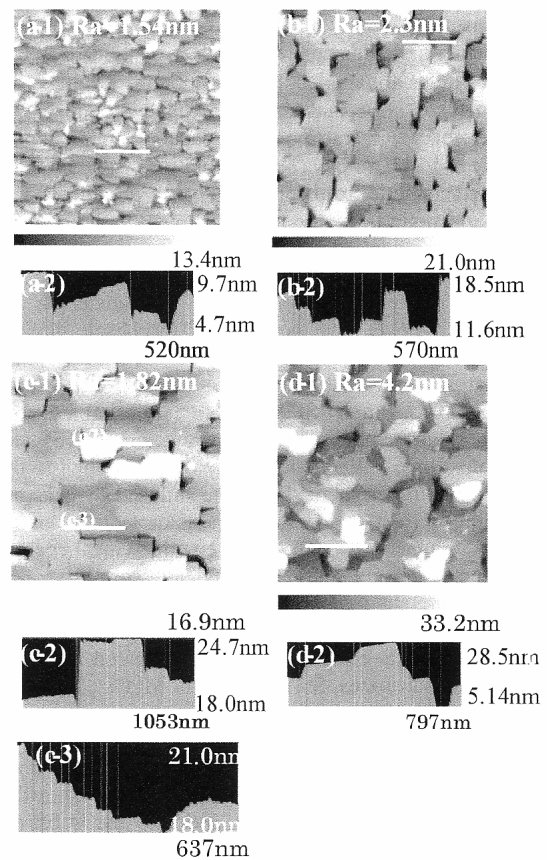


Figure 5. AFM surface images (2×2 μm²) and line-profiles of Cr₂O₃ thin films prepared at Ts= 400°C (a-1 and 2), 500°C (b-1 and 2), 550°C (c-1, 2 and 3), 600°C (d-1 and 2).

$T_s=400^\circ\text{C}$, characteristic rectangle grains appeared with the size $100 \times 100 \sim 200\text{nm}^2$. From the line-profile (a-2), the average bump between grains was approximately 3.5nm. The average roughness (Ra) was comparatively small, 1.5nm. In (b-1) at $T_s=500^\circ\text{C}$, the grains coalesced and their shape changed into square. In (c-1) at $T_s=550^\circ\text{C}$, the coalescence proceeded more clearly and grain boundaries decreased. As shown in the focused line-profile (c-3) several steps were clearly observed in one grain plane. Those steps height was same the lattice spacing of Cr_2O_3 with R -plane (0.363nm). The surface morphology suggested the 2-dimensional growth took place on 550°C substrates. In (d-1) at $T_s=600^\circ\text{C}$, the grain size became larger. The bump of grains increased as increasing T_s . The value of Ra was large, 4.2nm and bunching steps increased. A step and terrace structure disappeared as shown in (d-2).

It is thought that the grain boundary is caused by the internal stress which is induced from the lattice mismatch. As stated in the XRD result the inplane stress from the R -cut sapphire was relieved at about 500°C . The surface of the film prepared at the 550°C was very smooth and revealed 2-dimensional growth. Conclusively the results of XRD and AFM suggested that the growth of Cr_2O_3 is superior at $T_s=500 \sim 550^\circ\text{C}$ and results in an excellent step and terrace structure which suggests the possibility of an epitaxial growth.

3.2 Growth of Cr_2O_3 on the Nb-STO with CeO_2 buffer

Cr_2O_3 films were not grown directly on the STO substrate. Then the buffer layers of CeO_2 were prepared. Fig. 6. shows XRD patterns of $\text{Cr}_2\text{O}_3/\text{CeO}_2/\text{Nb-STO}$ bi-layers (sample A, B and C). The sample A was deposited on the rough CeO_2 layer which was not post-annealed after sputter deposition and has $R_a=4.2\text{nm}$. No Bragg diffraction peak from Cr_2O_3 was observed. The sample B was prepared on the smooth CeO_2 @ $R_a=0.41\text{nm}$ layer, post-annealed at 1000°C . The sample revealed a c -axis oriented growth of the trigonal Cr_2O_3 . The sample C was deposited on the CeO_2 layer post-annealed at 500°C and showed mixed phase growth with a -axis orientation. The Cr_2O_3 ($n n -2n 0$) and (30-30) peaks were observed. The results of XRD indicated that the trigonal Cr_2O_3 grew on the CeO_2 (100)//STO(100) with a -axis or c -axis orientation.

The AFM surface images of sample A and B were shown in Figures 7(a-1) and (b-1). Figures 7(a-2) and (b-2) show the surface morphology of the CeO_2 (100) substrate for sample A and B, respectively. In the film (a-1) grown on the substrate (b-1) various sizes of grains and deep valleys of grain boundaries were observed. The depth of the valley was above 70nm and the value of Ra was ca. 17nm. In the film (b-1) on the substrate (b-2) smooth surfaces with Ra of 4.2nm were observed.

The surfaces of sample A were not smooth and no Bragg diffraction peak was observed. On the other hand, hexagonal grains appeared in smooth surfaces of sample B. So it was thought that the smooth part of sample B corresponded to c -planes of Cr_2O_3 . These results suggested that the smoothness of the CeO_2 layer affected to Cr_2O_3 growth as a dominant factor and applications of Cr_2O_3 films are fulfilled for SFQ

electronic devices fabricated on STO substrates.

Fig. 8. shows a leakage current density as a function of applied electric field in sample B. The diameter of the measuring electrode was 0.45mm and the total thickness of the $\text{Cr}_2\text{O}_3/\text{CeO}_2$ film was ca. 230nm. The observed leakages current was suppressed less than $10^{-5}\text{A}/\text{cm}^2$ below electric field of 0.24MV/cm, the applied voltage of about 5V. So the Cr_2O_3 film works as the ME material under the order of 0.1MV/cm.

Assuming that the ME coefficient of Cr_2O_3 along the

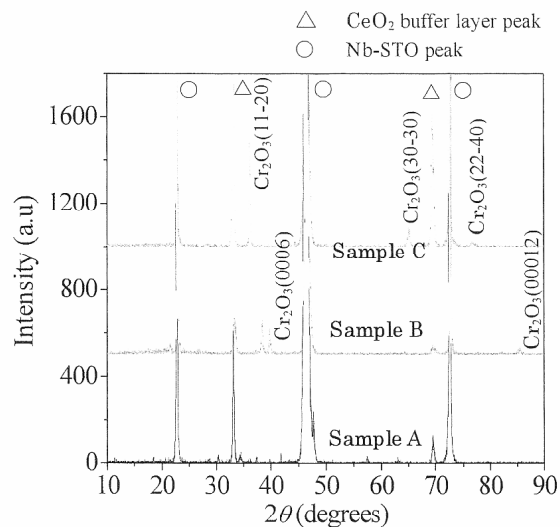


Fig. 6. XRD patterns of $\text{Cr}_2\text{O}_3/\text{CeO}_2/\text{Nb-STO}$ sample A, B, and C. The preferential c -axis orientation was confirmed in sample B. Sample C shows the a -axis growth with ($n n -2n 0$) plane.

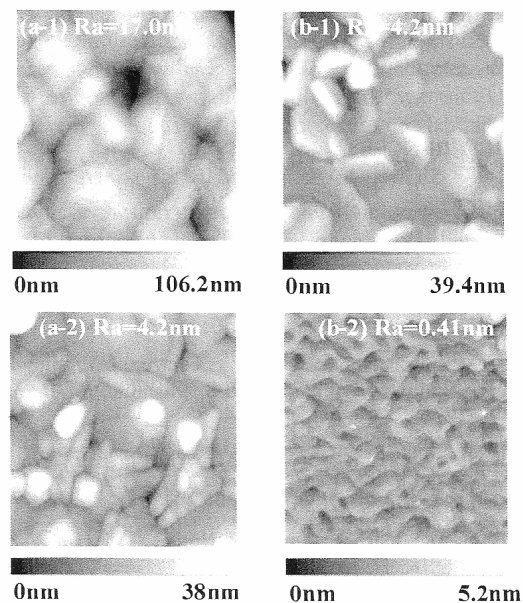


Fig. 7. AFM surface images ($1 \times 1 \mu\text{m}^2$) of sample A (a-1), sample B (b-1), the $\text{CeO}_2/\text{Nb-STO}$ substrate of sample A (a-2), and the substrate of sample B (b-2).

c -axis is 10^{-4} at about 50K [9, 10], the expected magnetic field in the film is about 1Gauss. Also the magnetic field induced at 300K attains up to 10Gauss, ten times as large as that at 50K.

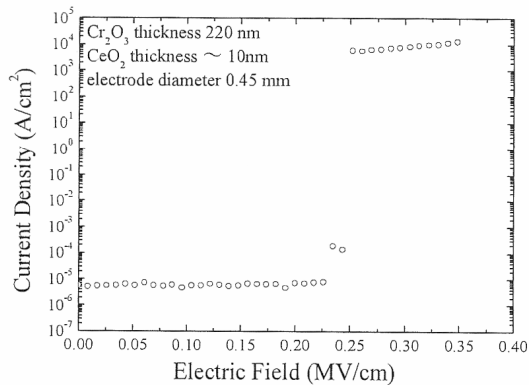


Fig. 8. The leakage current density vs. applied electric field in sample B of $\text{Cr}_2\text{O}_3/\text{CeO}_2/\text{Nb-STO}$. The bi-layered film was an insulator below electric field of *ca.* 0.24MV/cm.

[9] H. Wigelmann, A. G. M. Jansen, P. River and H. Schmid, *Ferroelectric.*, **62**, 141-146 (1994).

[10] N. Iwata, K. Matso, N. Ootsuka and H. Yamamoto, *Mat. Res. Soc. Symp. Proc.*, **811**, 425-430 (2004).

(Received December 10, 2006; Accepted August 21, 2007)

4. CONCLUSION

The ME Cr_2O_3 films were prepared on the R -cut sapphire and on Nb-STO with CeO_2 buffers by sputtering. The 2-dimensional growth of Cr_2O_3 was observed on the R -cut sapphire at 500~550°C. The $\text{CeO}_2/\text{Nb-STO}$ substrate successfully resulted in the growth of Cr_2O_3 with a -axis and c -axis orientation. The prepared $\text{Cr}_2\text{O}_3/\text{CeO}_2/\text{Nb-STO}$ revealed the superior insulating properties and assured comparatively large magnetic field of about 1Gauss. The obtained results strongly suggested that the Cr_2O_3 films are applicable for novel SFQ devices fabricated on cubic STO substrates.

5. REFERENCES

- [1] K. Siratori, K. Kohn, and E. Kita, *Acta physica polonica A.*, **81**, 431-466 (1992).
- [2] P. J. Brown, J. B. Forsyth, and F. Tasset, *Solid State Science.*, **7**, 682-689 (2005).
- [3] M. Foebig, *Journal of Physics D*, **38**, 123-152 (2005).
- [4] M. Shirakawa, M. Miura, T. Ohazama, Y. Shingai, A. Saito, M. Mukaida, and S. Ohshima, *Physica C.*, **412**, 1277-1280 (2004).
- [5] M. Spancova, I. Vavra, S. Gazi, D. Machajdik, S. Chromik, K. Frohlich, *Journal of Crystal Growth.*, **218**, 287-293 (2000).
- [6] H. Y. Lee, S. I. Kim, Y. P. Hong, Y. C. Lee, Y. H. Park, K. H. Ko, *Surface and Coatings Technol.*, **173**, 224-228 (2003).
- [7] Ai. Kamitani, H. Wakana, A. Ogawa, S. Adachi, K. Higuchi, H. Yamamoto, K. Tanabe, *J. Mater. Res.*, **21**, 263-269 (2006).
- [8] P. Hones, M. Diserens, F. Levy, *Surface and Coatings Technol.*, **120**, 277-283 (1999)

Improvement of ramp fabrication for high- T_c ramp-edge Josephson junction

K. Igarashi^{a,b,*}, K. Higuchi^{a,b}, H. Wakana^a, S. Adachi^a, N. Iwata^b,
H. Yamamoto^b, K. Tanabe^a

^a *Superconductivity Research Laboratory, ISTEK, 1-10-13 Shinonome, Koto-ku, Tokyo 135-0062, Japan*

^b *Nihon University, 7-24-1, Narashinodai, Funabashi-shi, Chiba 274-8501, Japan*

Accepted 6 March 2007

Available online 29 May 2007

Abstract

The fabrication process of ramps for HTS ramp-edge Josephson junctions was studied. We refined a photolithography method for producing ramps having smooth surfaces without a tail structure and similar angles in a chip. Optimization of resist reflowing parameters was crucially important. It was found that excessive reflowing gave rise to an increased spread in the angles. We demonstrated fabrication of smooth ramps with a small spread in their angles using a mask pattern for a toggle flip-flop circuit pattern by using the optimized reflowing parameters.

© 2007 Published by Elsevier B.V.

PACS: 81.65.Cf; 74.72.Bk; 82.37.Gk

1. Introduction

Ramp-edge Josephson junctions with interface-modified barriers using YBCO-type high- T_c superconductors (HTS) have been widely studied because of small spread of junction properties [1]. Before deposition of the counter electrode, the ramp surface of the base-electrode was changed to an amorphous structure by Ar ion bombardment. After deposition of the counter electrode on the modified ramp, the barrier layer was formed at the interface of the two electrodes. In fabrication of the junctions, several parameters that influence junction properties have been reported; for example, substrate temperature during the counter-electrode deposition [2], irradiation angle during Ar ion bombardment to form the modified ramp surfaces [3] and so on. The ramp angle is also one of the

parameters influencing the spread of junction properties [4]. It is necessary to develop a fabrication technique for the ramps having smooth surfaces and well-controlled angles [5,6]. To reduce the spread of junction properties, many ramps with the identical shape must be fabricated.

To fabricate the ramp-edge structures, the standard photolithography with reflowed photoresist and Ar ion-beam etching is generally applied. The cross-sectional images of an insulator/base-electrode bilayer film covered with reflowed photoresist before and after ion-beam etching are sketched in Fig. 1a. The ion-beam is irradiated along the slope of the reflowed photoresist. A smooth ramp can be fabricated. Horstmann et al. [6] pointed out the necessity of the reflowing process to make smooth ramps. They tried to fabricate the ramps without reflowing a photoresist. Two parts of the slope could be distinguished in the ramp. A steeper part of approximately 20° was followed by a long and shallow tail of only a few degrees. This situation is sketched in Fig. 1b. The resist stencil shades an area of significant width for incident angle $\beta < 90^\circ$. During the ion irradiation, not only thin films but also photoresist

* Corresponding author. Address: Nihon University, 7-24-1, Narashinodai, Funabashi-shi, Chiba 274-8501, Japan. Tel.: +81 3 3536 5709; fax: +81 3 3536 5717.

E-mail address: kyu_igarashi_1214@istec.or.jp (K. Igarashi).

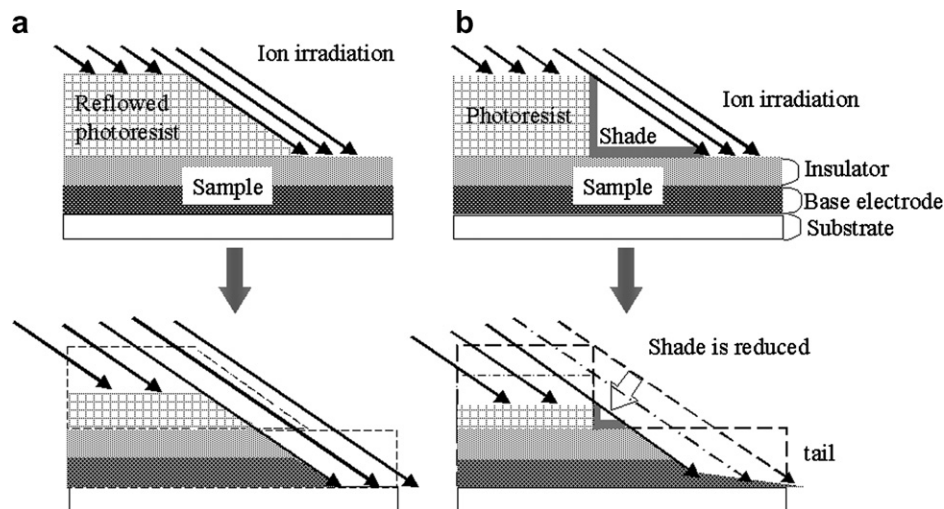


Fig. 1. Schematic illustrations for formation of the ramp profiles using (a) a reflowed photoresist and (b) a not-reflowed one.

are etched. As the photoresist is reduced, the shaded area becomes narrower. This narrowing produces a tail structure in the etched film. On the other hand, Blank et al. [7] and Schoop et al. [8] developed a fabrication method not using the reflowing process. They used TiN as the hard and thin mask, instead of photoresist. However, their method needs an additional vacuum chamber for TiN deposition.

Recently, we have fabricated HTS electronic devices containing many interface-modified ramp-edge junctions [9]. A 1σ -spread in critical current of approximately 8% was achieved for a 1000-junction series-array on a superconducting ground plane [10]. Proper operations of several elementary circuits for SFQ electronic devices were demonstrated [11]. For further reduction of the spread of these junctions, we initiated reinvestigation of our fabrication process. In this work, we focus on the ramp structure before the counter-electrode deposition. In our process, the resist reflowing process was chosen for convenience to fabricate the ramps. We investigated the structures of ramps located at different positions in a chip using an atomic force microscope (AFM) and observed the spread in ramp angle. After discussion of the correlation between the ramp structure and the shape of the reflowed photoresist, we propose a more suitable reflowing process to fabricate smooth ramps with the same angle and demonstrate it.

2. Experimental

Multilayer structures including an $Y_{0.9}La_{0.2}Ba_{1.9}Cu_3O_y$ (La-YBCO) superconductor and a $SrSnO_3$ (SSO) insulator were prepared on $15 \times 15 \text{ mm}^2$ MgO (100) substrate by off-axis magnetron sputtering. Their sequence was SSO (250 nm)/La-YBCO (200 nm)/SSO (250 nm)/La-YBCO (200 nm)/MgO. The upper and the lower La-YBCO layers are a base-electrode and a ground plane, respectively. Ramps were formed at the edges of the upper SSO (250 nm)/La-YBCO (200 nm) bilayer patterns by standard

photolithography with resist reflowing and Ar ion-beam etching.

Our standard process for ramp fabrication is as follows. At first, a mask of photoresist was made by spin-coating Shipley S1813 and baked in an electric furnace at 85°C for 20 min. The thickness of the mask was $1.4 \mu\text{m}$. After patterning by ultraviolet exposure and photoresist development, the sample was baked at 145°C for 5 min to reflow the photoresist. Ramps were formed by Ar ion-beam etching with an acceleration voltage of 280 V and an incident angle of 30° to the substrate with sample rotation. Finally, the mask was removed by O_2 -plasma ashing. We tried using another mask of Shipley S1808 ($0.8\text{-}\mu\text{m}$ thick). The thinner mask was baked under different conditions.

For morphology studies on the obtained ramps, an “open air” Nanopics 2000 was used in AFM dumping mode. The ramp angle for the base-electrode was evaluated.

3. Results and discussion

We fabricated ramps by our standard process. Ramps with no tail were successfully obtained. Their angles were investigated by measuring a line profile of the ramps fabricated at edges of patterned bilayers with a variety of sizes, as illustrated in the inset of Fig. 2. Three samples were prepared by the same procedure. The ramp angles are plotted against the length of the pattern, l , in Fig. 2. It is found that the ramp angle depends on the size of the patterned bilayer. Sato et al. [10] investigated the shapes of photoresists (reflowed and not reflowed) and the formed ramps using a scanning electron microscope (SEM). They described that the shape of photoresist was copied to the ramp. In our experiments, the ramps with significantly steeper angles were obtained for $l = 10$ and $20 \mu\text{m}$, as shown in Fig. 2. It is deduced that the shapes of photoresist at the edges of the bilayer patterns with large and small size must be different after reflowing.

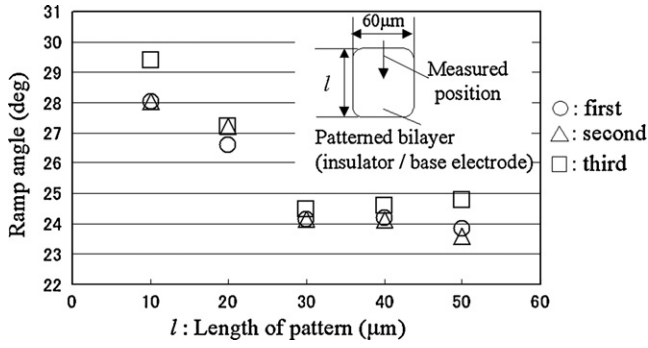


Fig. 2. Ramp angles for these samples including patterned insulator/base-electrode bilayers with various sizes, illustrated in the inset.

Before the reflowing, the photoresist at the edges has the same shape regardless the size of the bilayer pattern. As the baking for reflowing proceeds, the shape of the resist deforms gradually. In the above experiment, the 5-min baking made a difference in the shapes of the photoresist at the edges. It seems that the difference resulted in the observed spread in ramp angle, as shown in Fig. 2. It is expected that baking for a shorter period would make the difference less significant. Optimization of the reflowing condition, or the baking period and/or temperature, is crucially important. However, insufficient baking cannot eliminate the shaded portion which produces a tail structure (see Fig. 1). We changed the thick resist (1.4 μm) to a thinner one (0.8 μm) and optimized the reflowing conditions, that is the baking period at 145 °C.

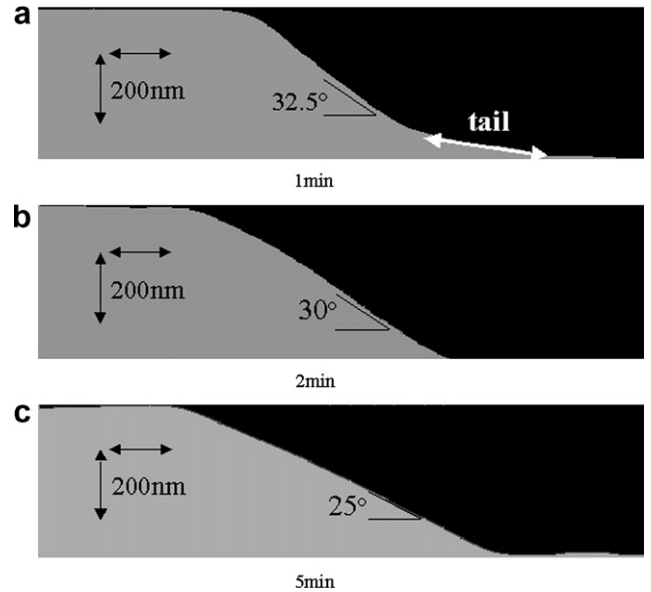


Fig. 3. AFM line profiles for the ramps. The ramps were fabricated using a thinner mask of S1808 (thickness, 0.7 nm) and reflowed at 145 °C for (a) 1, (b) 2 and (c) 5 min, respectively.

Fig. 3 shows the line profiles for the ramps fabricated using the photoresists reflowed for 1, 2 and 5 min. Reflowing for 1 min was not enough to eliminate the tail. Smooth ramps without tails were fabricated using resist reflowed for 2 min and more. The ramp angles were 32.5°, 30° and 25° for the reflowing periods of 1, 2 and 5 min, respectively.

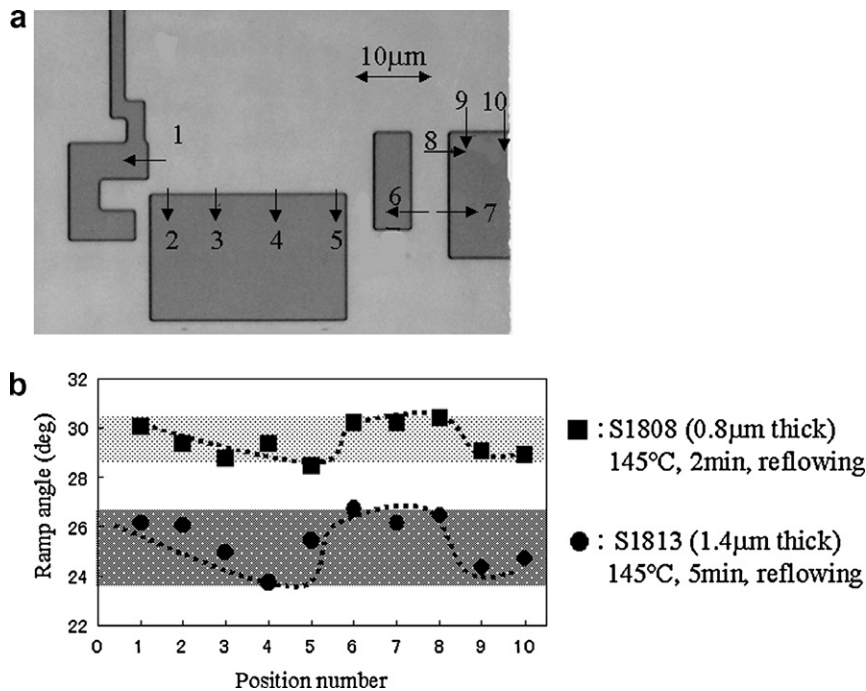


Fig. 4. (a) The optical microscope image of a toggle flip-flop circuit patterns and (b) the measured angles of the ramps. The numbered arrows in the image indicate the measured positions. The square and closed circles are ramp-angles fabricated using a thinner photoresist mask with 2-min-reflowing and a thicker photoresist mask with 5-min-reflowing, respectively.

The spreads in the ramp-edge angles made using 2-min- and 5-min-reflowed resists were compared. The angles for eight edges of bilayer patterns with different size ($15 \times 17 \mu\text{m}^2$ – $65 \times 80 \mu\text{m}^2$) in a chip were measured. The 2-min- and 5-min-reflowed resists yielded ramps with $30.0^\circ \pm 0.5^\circ$ and $25.0^\circ \pm 2.0^\circ$, respectively. The shorter baking period for reflowing resist resulted in the smaller spread, in accordance with our expectation. It is thus demonstrated that the use of the thin mask reflowed for 2 min can produce smooth ramps without a tail and improves the spread of the ramp angles in a chip.

We tried applying this improved method to prepare ramps using a pattern of an actual elementary circuit. The obtained ramp angles were compared with those fabricated using the standard method. Fig. 4a shows an optical microscope image of patterned bilayer for a toggle flip-flop. It contains base-electrodes with various size. The arrows in the figure indicate the positions for junction fabrication. The obtained results are plotted in Fig. 4b. The improved and standard methods yielded ramps with $29.5^\circ \pm 0.7^\circ$ and $25.5^\circ \pm 0.3^\circ$, respectively. A smaller spread was actually achieved by using the improved method. Additionally, we tried to draw the break lines along the obtained data by eye guide in Fig. 4b. It is found that two curves wind similarly. We considered that this tendency is due to the design of the circuit. For the further improvement of the ramp fabrication, we need to focus on the circuit design.

4. Conclusion

We investigated the ramp-edge angles of base-electrodes with a variety of size in a chip. An appreciable spread was observed and the deviation in the angle depended on the size. It was speculated that the spread in the angle originated from a difference in the edge-shape of resist mask. We refined a photolithography method containing a resist reflowing process. A method to shape the resist mask hav-

ing identical structures at edges was proposed. A thin photoresist mask was utilized in order to avoid formation of a tail structure in the ramps. It was found that excessive reflowing gave rise to an increased spread in the angle. By using the optimized resist reflowing parameters, we demonstrated fabrication of smooth ramps with a small spread in their angles for a toggle flip-flop circuit pattern.

Acknowledgment

This work was supported by the New Energy and Industrial Technology Development Organization (NEDO) as Superconductors Network Device Project.

References

- [1] T. Satoh, M. Hidaka, S. Tahara, *IEEE Trans. Appl. Supercond.* 9 (1999) 3141.
- [2] H. Wakana, S. Adachi, M. Horibe, Y. Ishimaru, O. Horibe, Y. Tarutani, K. Tanabe, *Physica C* 378–381 (2002) 1353.
- [3] H. Wakana, S. Adachi, M. Horibe, Y. Ishimaru, O. Horibe, Y. Tarutani, K. Tanabe, *Jpn. J. Appl. Phys.* 41 (2002) 239.
- [4] M. Horibe, Y. Inagaki, G. Matsuda, N. Hayashi, K. Kawai, M. Maruyama, A. Fujimaki, H. Hayakawa, *Supercond. Sci. Technol.* 12 (1999) 726.
- [5] T. Makita, K. Toma, K. Ishikawa, H. Zama, T. Utagawa, U. Kawabe, K. Tanabe, *IEEE Trans. Appl. Supercond.* 11 (2001) 155.
- [6] C. Horstmann, P. Leinenbach, A. Engelhardt, R. Gerber, J.L. Jia, R. Dittmann, U. Memmert, U. Hartmann, A.I. Braginski, *Physica C* 302 (1998) 176.
- [7] D.H.A. Blank, G.J.H.M. Rijnders, R.M.H. Bergs, M.A.J. Verhoeven, H. Rogalla, *IEEE Trans. Appl. Supercond.* 7 (1997) 3323.
- [8] U. Schoop, M. Schonecke, S. Thienhaus, S. Schymon, L. Alf, R. Gross, *Physica C* 351 (2001) 200.
- [9] Y. Tarutani, Y. Ishimaru, H. Wakana, S. Adachi, K. Nakayama, Y. Oshikubo, O. Horibe, Y. Morimoto, K. Tanabe, *Physica C* 412–414 (2004) 1528.
- [10] H. Sato, F.J.G. Roesthuis, A.H. Sonnenberg, A.J.H.M. Rijnders, H. Rogalla, D.H.A. Blank, *Supercond. Sci. Technol.* 13 (2000) 522.

Fabrication of ramp-edge Josephson junction by PLD method using double plume

K. Higuchi^{a,b,*}, K. Igarashi^{a,b}, H. Wakana^a, K. Nakayama^a, S. Adachi^a,
N. Iwata^b, H. Yamamoto^b, K. Tanabe^a

^a Superconductivity Research Laboratory, ISTE, 1-10-13 Shinonome, Koto-ku, Tokyo 135-0062, Japan

^b Nihon University, 7-24-1, Narashinodai, Funabashi-shi, Chiba 274-8501, Japan

Available online 21 June 2006

Abstract

Fabrication of high- T_c ramp-edge Josephson junctions with interface-modified barriers in a wide area have been studied. A novel pulsed laser deposition apparatus with a double laser plume was newly designed. We succeeded in observing RSJ I - V characteristics with an excess current ratio as low as approximately 15% for all junctions dispersively located on a chip with a size of $15 \times 15 \text{ mm}^2$. It was found that the characteristics of the junctions significantly depend on the geometric configuration of the laser plume and the ramps during counter-layer deposition.

© 2006 Elsevier B.V. All rights reserved.

PACS: 74.72.Bk; 74.50.+r; 81.15.Fg

Keywords: $\text{Y}_{0.9}\text{La}_{0.2}\text{Ba}_{0.9}\text{Cu}_3\text{O}_y$; Ramp-edge Josephson junction; Double laser plume

1. Introduction

Multilayer structures of various oxide thin films including Josephson junctions are indispensable in high- T_c electronic devices such as single flux quantum (SFQ) digital circuits [1–4]. SFQ circuits require reproducible fabrication of Josephson junctions with high $I_c R_n$ products and small $1 - \sigma I_c$ spreads. Interface-modified ramp-edge Josephson junctions have attracted much attention as reliable junctions, because of their higher $I_c R_n$ products and smaller I_c spreads in a chip than those reported in other types of high- T_c Josephson junctions [5,6]. The barriers of interface-modified junctions are fabricated from an amorphous layer, that is, made by an ion bombardment process. This amorphous layer is changed to the barrier layer through

appropriate annealing and counter-layer deposition processes [7]. Wakana et al. [8] have recently fabricated interface-modified ramp-edge Josephson junctions with La-doped $\text{YbBa}_2\text{Cu}_3\text{O}_y$ ($\text{Yb}_{0.9}\text{La}_{0.2}\text{Ba}_{1.9}\text{Cu}_3\text{O}_y$; La–YbBCO) counter-layer deposited by a pulsed laser deposition (PLD) method. It is well known that the properties of these junctions have a strong dependence on the recrystallization process of the interface-modified barrier. In the case of counter-layer deposition by PLD, in particular, the characteristics of the interface-modified ramp-edge Josephson junctions significantly depend on the geometric configuration of the laser plume and the ramps during counter-layer deposition [8].

In order to execute counter-layer deposition in a more homogeneous condition for the ramp surfaces, we designed a novel PLD apparatus with a double laser plume. A photographic view of the double plume during deposition is shown in Fig. 1. We expected that use of the double laser plume would enable us to fabricate ramp-edge Josephson junctions with more homogeneous characteristics in a wider area on a chip than the case for deposition with a

* Corresponding author. Address: Superconductivity Research Laboratory, ISTE, 1-10-13 Shinonome, Koto-ku, Tokyo 135-0062, Japan. Tel.: +81 3 3536 5709; fax: +81 3 3536 5717.

E-mail addresses: Higuchi@istec.or.jp (K. Higuchi), adachi@istec.or.jp (S. Adachi).



Fig. 1. Double laser plume during deposition.

single plume. In this work, we fabricated the junctions on a $15 \times 15 \text{ mm}^2$ substrate using the novel apparatus and investigated their properties. Samples with the counter-layers deposited employing different configuration of the double laser plume and the substrate were prepared. Properties of the junctions that were put all over a chip were examined.

2. Experimental

Firstly, multilayer films including a base-electrode layer (BE) on a ground plane (GP) were prepared on a $15 \times 15 \text{ mm}^2$ MgO (100) substrate by off-axis magnetron sputtering. $\text{Y}_{0.9}\text{La}_{0.2}\text{Ba}_{1.9}\text{Cu}_3\text{O}_y$ (La–YBCO) and SrSnO_3 (SSO) were used as a superconductor and an insulator, respectively. The layer sequence was SSO (250 nm)/La–YBCO (BE; 200 nm)/SSO (250 nm)/La–YBCO (GP; 200 nm)/MgO substrate. Ramp-edge structures for the

upper two layers were fabricated by the standard photolithography using a resist reflow process and Ar ion milling at 280 V with an incident angle of 30° . After removing the photoresist mask, an amorphous layer was formed on the ramp surfaces by Ar ion bombardment for 3 min at an acceleration voltage of 500 V and the incident angle of 90° to the substrate.

A La–YbBCO counter-layer was deposited by the two-step deposition process [9]. A 20-nm-thick primary-layer, which considerably influences the junction properties, was firstly deposited. Then a 200-nm-thick secondary-layer covered it to form a counter layer with low sheet inductance. Fig. 2 shows schematic illustrations of the substrate, target and the laser plumes for the deposition of the primary and secondary layers. During deposition of the former layer, the substrate was not rotated and the double plume stayed at two positions separated by a distance of d , as shown in Fig. 2(a). Points A, B, C and D in the figure are given for marking the projection of the plume centers in a plane including the substrate surface. We tried two distances of $d = 15$ and 25 mm. Deposition was carried out at a laser frequency of 5 Hz in 20-Pa oxygen atmosphere. The substrate-target distance was 67 mm. The energy density on the target was 1.7 J/cm^2 for each beam. For the secondary-layer deposition, the substrate was rotated and the double plume with a constant distance of 25 mm was scanned on the target, as shown in Fig. 2(b). The laser frequency, energy density and the substrate-target distance were changed to 2 Hz, 1.2 J/cm^2 and 70 mm, respectively.

In this work, we did not use Ag-paste for fixing a substrate on a sample holder to improve reproducibility. Possibility of contamination due to Ag-paste can be avoided. The substrate was directly heated by thermal radiation from a heater located at the backside of the substrate. Tem-

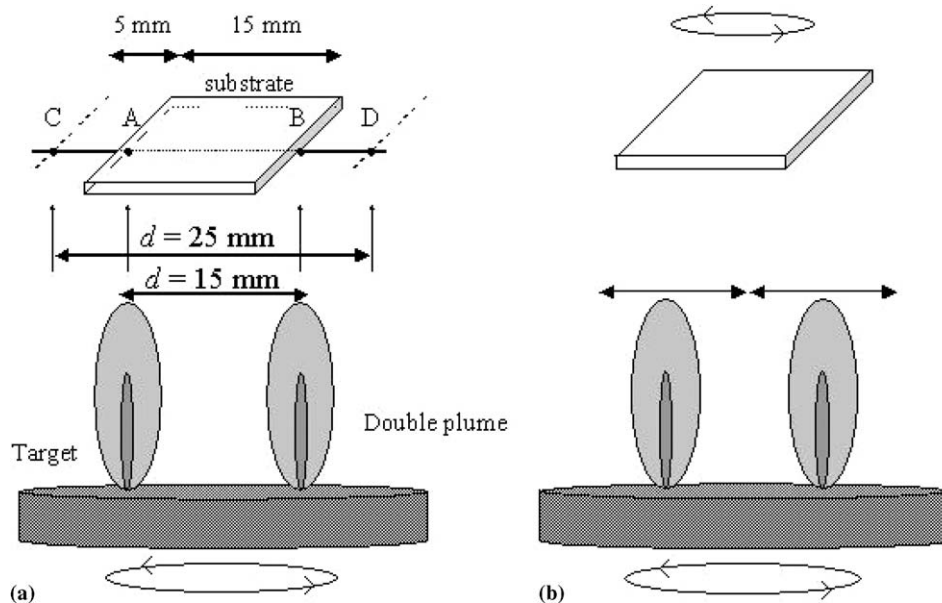


Fig. 2. Schematic illustration of the substrate, the target and the laser plumes for depositions of (a) the primary and (b) the secondary layers. Characters of A–D are markers of the plume centers.

perature of the heater was set at 840 °C during the counter-layer deposition. The actual substrate temperature was unknown. Finally, a 450-nm-thick Au film was deposited on the La–YbBCO counter-layer, and the counter-electrode was patterned to width of 5 μm by photolithography and Ar ion milling. Current–voltage (I – V) characteristics for the fabricated junctions were evaluated at 4.2 K by a four-probe method.

3. Results and discussion

Fig. 3 shows typical I – V characteristics for the junction with the primary-layer prepared at $d = 15$ mm. The obtained junction exhibits resistively-shunted-junction (RSJ) I – V characteristics with an excess current ratio as low as approximately 15%. All the junctions on a chip showed RSJ I – V characteristics with similar excess current. The distribution of I_c values on a chip is shown in Fig. 4.

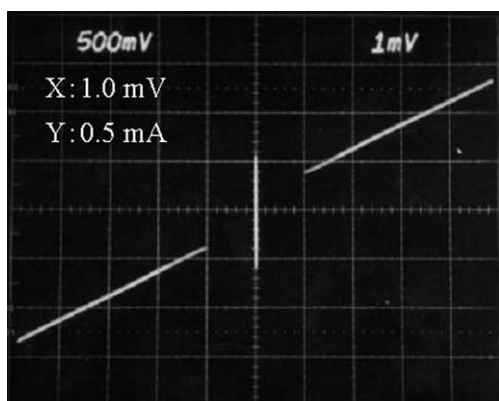


Fig. 3. Typical I – V characteristics for the junction with a primary layer prepared at $d = 15$ mm.

Directions of all the examined ramps were identical, as drawn in the inset of Fig. 4. The height of each column indicates the average I_c for 10 junctions within an area of $200 \times 200 \mu\text{m}^2$. The $1-\sigma$ spreads in each column was 13.7–29.7%. The columns in the figure indicates that the junctions on the chip with a size of $15 \times 15 \text{ mm}^2$ exhibited $I_c = 0.21$ – 1.1 mA. The $1-\sigma$ spread in I_c was 47%. It was reported that the spreads of I_c for ramp-edge junctions without ground plane in a $10 \times 10 \text{ mm}^2$ substrate was 20% [10], being smaller than the obtained spread of 47% in the present study. We thought that the larger chip size and the junction fabrication on a ground plane made the reduction of the spreads difficult.

A contour map of I_c is also drawn in Fig. 4. The 15×15 area of a chip is divided to three regions in which the junctions exhibited I_c over 1 mA, 1.0–0.5 mA and less than 0.5 mA. It can be seen that I_c values are not distributed randomly on the chip. Assuming that the observed variation in I_c was caused by inhomogeneous substrate temperature, the I_c values should be concentrically distributed. The observed distribution is not so, as seen in Fig. 4. It suggests that the spatial configuration of the plumes and the ramps rather influenced the junction characteristics.

In the case of $d = 25$ mm, only a few junctions exhibited RSJ I – V characteristics with an excess current of 50%, as shown in Fig. 5(a). The other junctions show flux-flow-like I – V characteristics as in Fig. 5(b). The I_c mapping is illustrated in Fig. 6. This result implies that the formed barrier layers were inhomogeneous. The obtained results indicate that the junction properties significantly depend on geometric configuration of the laser plume and the ramps during counter-layer deposition even for the case of double plume PLD. Further optimization of the configuration is needed to improve the I_c spreads.

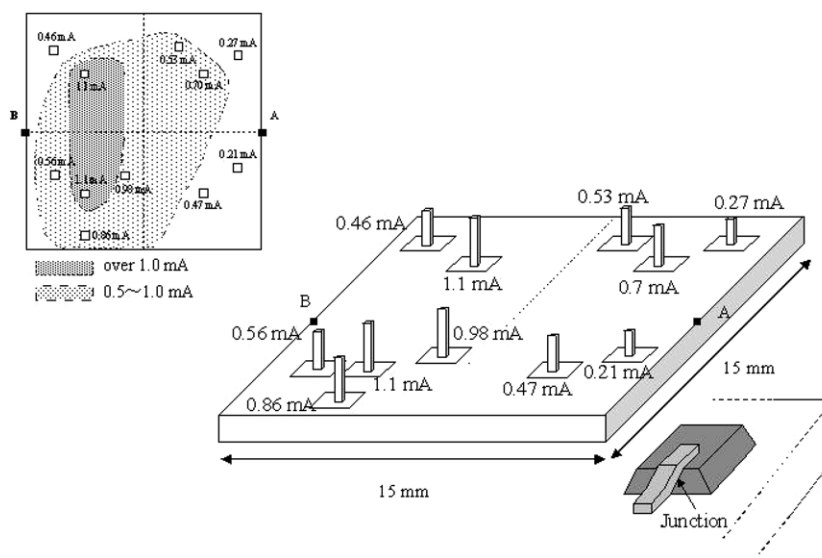


Fig. 4. Mapping of the average I_c values on a chip with a size of $15 \times 15 \text{ mm}^2$. The primary layer prepared at $d = 15$ mm. Characters of A and B are markers of the plume centers. Illustration of a typical junction is given in the inset. Directions of all junctions are identical. A contour map of I_c is in the inset.

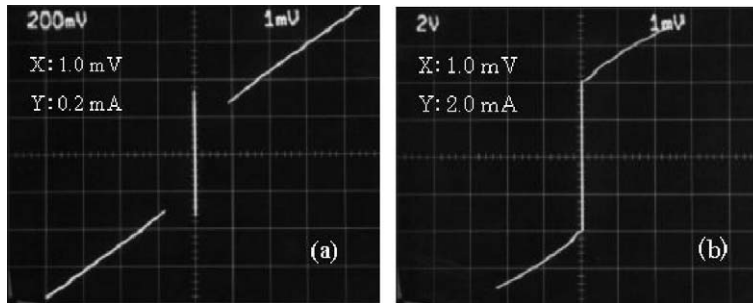


Fig. 5. Typical I - V characteristics for the junctions with a primary layer prepared at $d = 25$ mm.

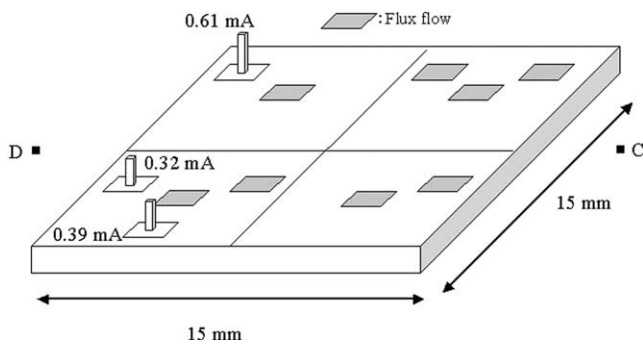


Fig. 6. Mapping of the average I_c values on a chip with a size of 15×15 mm². The primary layer prepared at $d = 25$ mm. Characters of C and D are markers of the plume centers. Directions of all junctions are identical, (see Fig. 4).

4. Conclusion

We fabricated interface-modified ramp-edge Josephson junctions using a newly designed PLD apparatus with a double laser plume. The junctions exhibiting RSJ I - V characteristics with an excess current 15% on a chip with a size of 15×15 mm². It proved that the PLD with a double laser plume could be utilized to realize high- T_c superconducting electronic devices with a large scale. Distribution of I_c on a chip was investigated. It was found that the spatial configuration of the plumes and the ramps during the counter-

layer deposition considerably influenced the junction characteristics.

Acknowledgements

This work was supported by the New Energy and Industrial Technology Development Organization (NEDO) as Superconductors Network Device Project.

References

- [1] A. Fujimaki, K. Kawai, N. Hayashi, M. Horibe, M. Maruyama, H. Hayakawa, IEEE Trans. Appl. Supercond. 9 (1999) 3436.
- [2] T. Satoh, J.G. Wen, M. Hidaka, S. Tahara, N. Koshizuka, S. Tanaka, IEEE Trans. Appl. Supercond. 11 (2001) 770.
- [3] J. Yoshida, S. Inoue, H. Sugiyama, T. Nagano, IEEE Trans. Appl. Supercond. 11 (2001) 784.
- [4] Y. Soutome, T. Fukazawa, K. Saitoh, A. Tsukamoto, K. Takagi, IEICE Trans. Electron E-85C (2002) 759.
- [5] B.H. Moeckly, K. Char, Appl. Phys. Lett. 71 (1997) 2526.
- [6] T. Satoh, M. Hidaka, S. Tahara, IEEE Trans. Appl. Supercond. 9 (2001) 770.
- [7] J.G. Wen, N. Koshizuka, S. Tanaka, T. Satoh, M. Hidaka, S. Tahara, Appl. Phys. Lett. 75 (1999) 2470.
- [8] H. Wakana, S. Adachi, M. Horibe, Y. Ishimaru, O. Horibe, Y. Tarutani, K. Tanabe, Jpn. J. Appl. Phys. 41 (2002) L 239.
- [9] H. Wakana, S. Adachi, M. Horibe, Y. Ishimaru, Y. Oshikubo, Y. Tarutani, K. Tanabe, Jpn. J. Appl. Phys. 41 (2002) L 1366.
- [10] H. Wakana, S. Adachi, M. Horibe, Y. Ishimaru, O. Horibe, Y. Tarutani, K. Tanabe, Physica C 378–381 (2002) 1353.

$I_c R_n$ product of $\text{YBa}_2\text{Cu}_3\text{O}_{7-x}$ ramp-edge junctions at temperatures higher than 30 K

Y. Morimoto^{a,b}, Y. Tarutani^{a,*}, H. Wakana^a, S. Adachi^a, K. Tsubone^a, Y. Ishimaru^a, K. Nakayama^a, Y. Oshikubo^a, O. Horibe^a, N. Iwata^b, H. Yamamoto^b, K. Tanabe^a

^a Superconductivity Research Laboratory, ISTEK, 1-10-13, Shinonome, Koto-ku, Tokyo 135-0062, Japan

^b Nihon University, 7-24-1, Narashinodai, Funabashi-shi, Chiba 274-8501, Japan

Abstract

We examined temperature dependence of the $I_c R_n$ (I_c being the critical current and R_n being the normal-state resistance) product for interface-engineered $\text{YBa}_2\text{Cu}_3\text{O}_{7-x}$ ramp-edge junctions formed on a groundplane. There were two types for the temperature dependence of the $I_c R_n$ product. One was the linear temperature dependence, and the other was a dependence that shows the steeper drop with temperature. There were two factors that were responsible for the temperature dependence of the $I_c R_n$ value. These were critical temperature T_c of the junctions and temperature dependence of the R_n value. The $I_c R_n$ value more than 1 mV at 40 K was obtained for the junction that had the T_c of 84 K and the positive coefficient of R_n value on temperature.

© 2006 Published by Elsevier B.V.

PACS: 74.78.Bz; 85.25.Dq

Keywords: $I_c R_n$ product; Oxide SFQ circuit; Hysteresis; Excess current

1. Introduction

In an oxide single-flux-quantum (SFQ) circuit, $I_c R_n$ product of Josephson junctions is very important for improving an operating frequency [1]. The $I_c R_n$ product is also important for a driver circuit because an output voltage is almost proportional to the $I_c R_n$ product. The $I_c R_n$ product much more than 2 mV at 4.2 K has easily been obtained for oxide junctions. This value is more than five times as much as the $I_c R_n$ product of resistor-shunted Nb junctions that have a critical current density less than 2000 A/cm².

Oxide SFQ circuits are supposed to be operated at temperatures from 30 K to 40 K when oxide SFQ chips are cooled down by a single-stage refrigerator. The $I_c R_n$ product required for the oxide junctions may be more than

1 mV at these operating temperatures. This is because the $I_c R_n$ value of 1 mV is the least minimum value for operating SFQ circuits at frequencies more than 100 GHz [2]. However, the $I_c R_n$ product rapidly decreases as a temperature is increased. The temperature dependence of the $I_c R_n$ value for oxide junctions has not systematically been studied.

In this report, $\text{YBa}_2\text{Cu}_3\text{O}_{7-x}$ ramp-edge junctions are fabricated and their $I_c R_n$ products are investigated. Temperature dependence of the $I_c R_n$ products is measured and the $I_c R_n$ products from 30 K to 40 K are compared among junctions that show different characteristics. Requirement to the characteristics for the junctions whose $I_c R_n$ products are more than 1 mV from 30 K to 40 K are found out for applying the ramp-edge junctions to SFQ circuits.

2. Junction fabrication and measurement

The ramp-edge junctions were made by the interface-engineering method [3,4]. A $\text{La}_{0.2}\text{Y}_{0.9}\text{Ba}_{1.9}\text{Cu}_3\text{O}_{7-x}$ film

* Corresponding author. Tel.: +81 3 3536 5709; fax: +81 3 3536 5705.
E-mail address: y-morimoto4038@istec.or.jp (Y. Tarutani).

was used for a base electrode and a $\text{La}_{0.2}\text{Yb}_{0.9}\text{Ba}_{1.9}\text{Cu}_3\text{O}_{7-x}$ film was used for a counter electrode, respectively. The $\text{La}_{0.2}\text{Y}_{0.9}\text{Ba}_{1.9}\text{Cu}_3\text{O}_{7-x}$ was also used for a groundplane. SrSnO_3 films was used for insulating layers between two of these electrodes. A MgO single crystal was used for a substrate.

The base electrode and the counter electrode were deposited by the sputtering method and the pulse-laser-ablation method, respectively. Substrate temperature during the counter layer deposition was changed among junction fabrication runs. Other fabrication parameters including the base layer deposition condition were kept the same. Junction barrier layer was formed by irradiating Ar beam onto surface of the base electrode.

Current–voltage (I – V) characteristics of the ramp-edge junctions were measured by a four-terminal probe method. Chip temperatures were measured by using a carbon-glass resistor. A package and socket on which a junction chip was mounted were kept in close contact with a Cu block. The Cu block was covered by double permalloy cylinders that magnetically shielded the chip. The chip was cooled

down by keeping the sample holder into a liquid He cryostat. The chip temperature was controlled by adjusting the sample distance from the liquid He surface.

3. $I_c R_n$ product of ramp-edge junctions

Current–voltage (I – V) curves of six ramp-edge junctions were measured at temperatures from 4.2 K to 90 K. These junctions were denoted as (A) throughout (F).

The I – V curves were measured at every four or five degrees from 4.2 K throughout 90 K. The I – V curves of junctions (A), (B), (C) and (F) measured at 40 K are shown in Fig. 1. These I – V curves are representing typical characteristics of ramp-edge junctions. These I – V curves differ in I_c or $I_c R_n$ values. These junctions show no hysteresis in the I – V curves although all these junctions showed different degrees of hysteresis at 4.2 K.

Temperature dependences of the $I_c R_n$ products for the junctions (A), (B), (C) and (F) are shown in Fig. 2. The $I_c R_n$ values were plotted from the I – V curves. Junctions (A) and (B) show the $I_c R_n$ products at 4.2 K more than

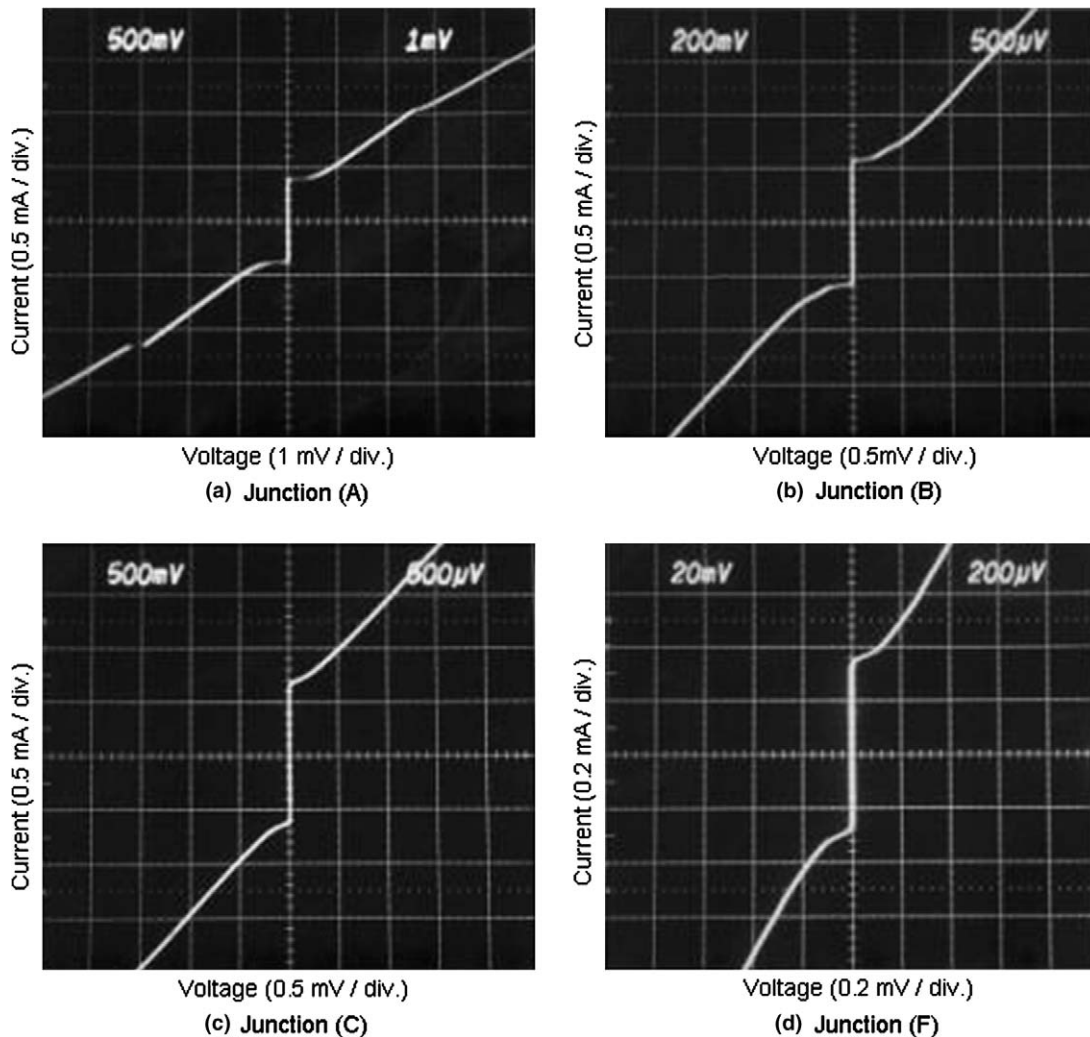


Fig. 1. I – V curves of ramp-edge junctions (A), (B), (C) and (F). Measured temperature was 40 K.

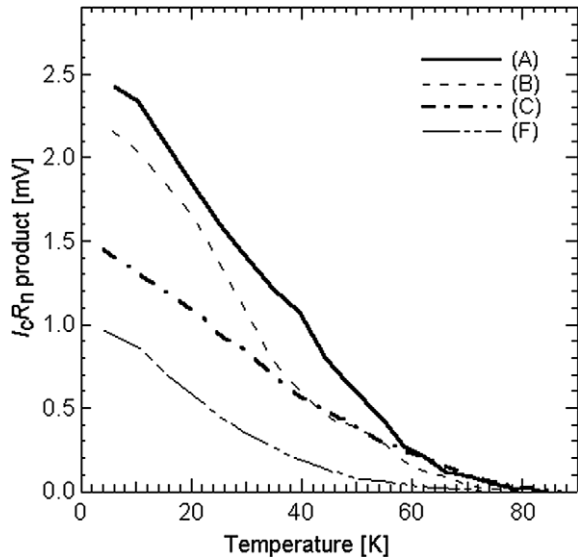


Fig. 2. The $I_c R_n$ product – temperature characteristics.

2 mV. On the other hand, junctions (C) and (F) show the $I_c R_n$ products less than 1.5 mV and 1 mV, respectively. Slope of the $I_c R_n$ products for junction (A) and junction (B) are much different. The $I_c R_n$ product of junction (B) at 40 K is almost comparable to that of sample (C) as a result of the steeper temperature dependence. Temperature dependences of the $I_c R_n$ products for junction (D) and junction (E) resembled those for junctions (A) and (B), respectively. From these result, requirements for the $I_c R_n$ value to be more than 1 mV at 40 K are not only the $I_c R_n$ product being much more than 2 mV at 4.2 K but also dependence of the $I_c R_n$ product on temperature being weak. Therefore, the ratio of the $I_c R_n$ value at 40 K to that at 4.2 K is an important parameter. This value is denoted as $I_c R_n (40\text{ K}/4.2\text{ K})$.

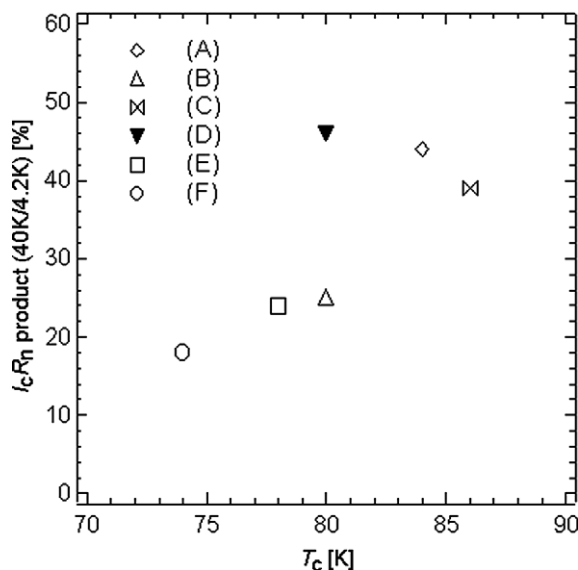


Fig. 3. Dependence of the $I_c R_n (40\text{ K}/4.2\text{ K})$ value on the junction T_c .

Dependences of the $I_c R_n (40\text{ K}/4.2\text{ K})$ values on the junction T_c are shown in Fig. 3. T_c of the base electrode was from 85 K to 86 K. The T_c of junction was corresponding to that of counter electrodes. As shown in Fig. 3, ratio of the $I_c R_n$ product at 40 K to that at 4.2 K did not much decrease when the junction T_c was increased to that of the base electrode. Dependence of the junction T_c on the substrate temperature is shown in Fig. 4. The junction T_c increased as the deposition temperature was increased.

Temperature dependences of the normal-state resistance R_n for the junctions from (A) to (F) are shown in Fig. 5. Samples (A) and (D) show positive coefficients of the R_n

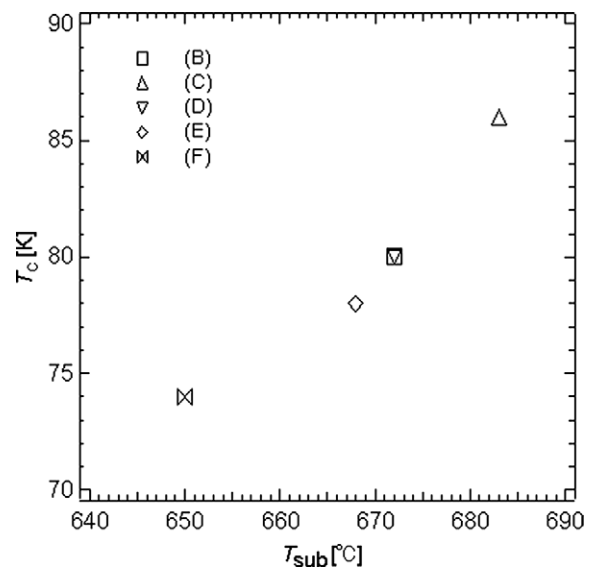


Fig. 4. Substrate temperature dependence of the T_c .

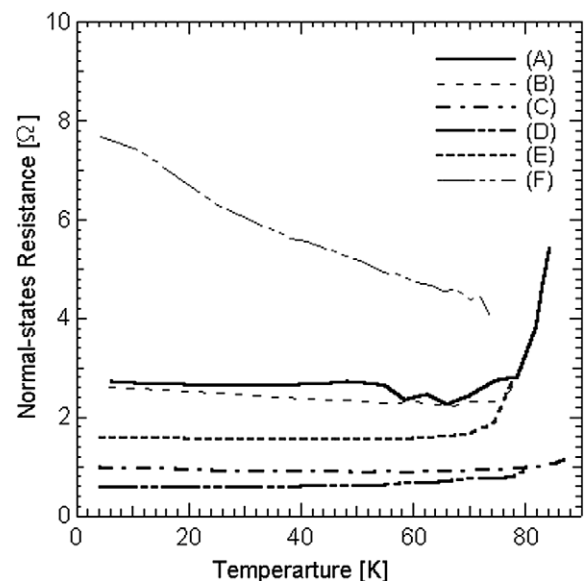


Fig. 5. Dependence of the R_n value on temperature.

value on temperature. On the other hand, samples (B) and (F) show negative coefficients of the R_n value on temperature. The $I_c R_n$ values of samples (A) and (D) almost linearly depended on temperature. Dependences of the $I_c R_n$ values on temperature for samples (B) and (F) was much steeper than that for samples (A) and (D). Decrease of the R_n values with temperature increase for samples (B) and (F) was one of the factor for the much greater decrease of the $I_c R_n$ products at 40 K.

The temperature dependence of the $I_c R_n$ value is determined by two factors. One is the typical temperature dependence that is determined by Josephson formulae [5]. The other is the conduction mechanism through a barrier. The normal resistance may change from 4.2 K to 90 K depending on the conduction mechanism. The negative coefficient of the R_n value for junction (F) indicates that the conduction through barrier is due to carrier hopping [6]. In this case, normal current is enhanced at higher temperatures in addition to tunnel current that owes the supercurrent. This normal current component may have suppressed the $I_c R_n$ value for junction (F) at higher temperatures. In this manner, there are two factors that are required to increase the $I_c R_n$ value more than 1 mV at 40 K. One is the $I_c R_n$ value at 4.2 K being more than 2 mV. The other is the temperature dependence of the $I_c R_n$ value being linear. Both factors can be satisfied by increasing the T_c of the counter electrode to that of the base electrode. Such a junction has a higher critical current density. It is necessary to decrease the junction size depending on the I_c value.

4. Conclusions

In conclusion, the temperature dependence of the $I_c R_n$ products for the ramp-edge junctions was examined. There were two types for the temperature dependence of the $I_c R_n$ product. One was the linear temperature dependence, and the other was the nonlinear dependence that showed rapid drop of the $I_c R_n$ product with temperature. The junctions having the $I_c R_n$ value more than 1 mV at 40 K had the linear temperature dependence of the $I_c R_n$ value in addition to the $I_c R_n$ value more than 2 mV at 4.2 K.

Acknowledgement

This work was supported by the New Energy and Industrial Technology Development Organization (NEDO) as Superconductors Network Device Project.

References

- [1] K.K. Likharev, V.K. Semenov, *IEEE Trans. Appl. Supercond.* 1 (1991) 3.
- [2] V.K. Kaplunenko, Z.G. Ivanov, E.A. Stepanov, T. Claeson, *Appl. Phys. Lett.* 67 (1995) 282.
- [3] H. Wakana, S. Adachi, H. Sugiyama, M. Horibe, Y. Ishimaru, Y. Tarutani, K. Tanabe, *Physica C* 392–396 (2003) 1362.
- [4] Y. Ishimaru, Y. Wu, O. Horibe, H. Tano, T. Suzuki, Y. Tarutani, U. Kawabe, K. Tanabe, *Jpn. J. Appl. Phys.* 41 (2002) 1998.
- [5] T. Van Duzer, C.W. Turner, *Principles of superconductive devices and circuits*, Elsevier, Amsterdam, 1980, p. 142.
- [6] M. Kupriyanov, in: Y. Bando, H. Yamauchi (Eds.), *Adv. Supercond.* 5 (1992) 1049.

Position-selective growth of vertically aligned carbon nanotubes for application of electronic-measuring nanoprobe

Hiroki Okuyama*, Nobuyuki Iwata, Hiroshi Yamamoto

College of Science and Technology, Nihon University, 7-24-1-401, Narashinodai, Funabashi, Chiba 274-8501, Japan

Available online 29 November 2006

Abstract

Position-selective growth of carbon nanotubes (CNTs) and vertically aligned CNTs (VACNTs) on patterned metal electrodes have been prepared by thermal chemical vapor deposition (TCVD) and DC plasma enhanced chemical vapor deposition (PECVD). We propose newly a position-controlling method of CNTs by controlling not only a position of Ni as catalysts but also the morphology of Mo as underlayers for the catalysts. The position-selective growth of CNTs was achieved at the edges of the patterned metal by TCVD. The morphologies of the Mo underlayer at the selected area were rough and porous. No CNTs grew on smooth Mo surfaces. The minimum width of selectively grown CNTs, ca. 2.6 μm , was approximately one-eightieth of the patterned metal, 200 μm . VACNTs were synthesized by a PECVD method, however, the VACNTs grew up all over the patterned metal. The Ni catalysts formed into fine particles on rough surfaces of the Mo underlayer. Then the selective growth was achieved by Ni fine particles formed only at the edges of the metal pattern. The results of PECVD suggest that the plasma promoted the Ni catalysts to become fine particles on smooth surfaces of Mo. Conclusively a position-controlling method of CNTs was demonstrated in the optimum conditions of the TCVD.

© 2006 Elsevier B.V. All rights reserved.

PACS: 81.05.Uw; 81.07.De; 81.15.Gh

Keywords: Carbon nanotube; Selective growth; Chemical vapor deposition; Vertical alignment

1. Introduction

Carbon nanotubes (CNTs) have been intensively studied because of many featured characteristics such as high electric conductivity [1], high permissible current density [2] and high mechanical strength in spite of high flexibility [3]. These characteristics are available to prepare various kinds of nanostructured devices such as scanning probe microscopy tip [4–6], field emitter [7–9] and so on. We are aiming at realizing a novel nanoprobe with CNTs that enables to approach it toward contact points on specimen easily without an accurate control for measuring of electric transport properties. In order to prepare such nanoscaled CNT devices, the controlling position and direction of CNTs is necessary. CNTs grow selectively from catalyst

particles by using chemical vapor deposition (CVD) [10]. A growth direction of CNTs is controlled by applying electric field during CVD growth [11].

The position-selective growth of CNTs is achieved by using the two characteristics as follows. One is that the CNTs grow selectively from fine particle catalysts. The other is that we can control the synthesis of the fine particle catalysts by noticing wettability on metal interfaces. Since wettability of metal interface is high, it is hard to form fine particles as overlayers on smooth underlayers. When the surfaces of underlayers are rough, overlayers form fine particles. In this paper, we propose newly a position-controlling method of CNTs by controlling not only the position of catalysts but also the surface morphology of metal underlayers. And we tried to prepare position-selective growth of CNTs and vertically aligned CNTs (VACNTs) on patterned metal electrodes for realization of the novel electronic measuring nanoprobe.

*Corresponding author. Tel./fax: +81 47 469 5457.

E-mail address: okuyama@yamanoya.ecs.cst.nihon-u.ac.jp (H. Okuyama).

2. Experimental

Patterned metals of Ni catalysts and Mo underlayers were deposited on quartz substrates through a metal mask (thickness: 30 μm , pattern width: 200 μm , gap: 100 μm) by RF magnetron sputtering. A background pressure of the chamber was 3.0×10^{-3} Pa, and the pressure during deposition was fixed at 2.0 Pa by feeding Ar gas. The growth conditions were 120 $^{\circ}\text{C}$ of substrate temperature, 50 W of sputtering power, 1 min of sputtering time for Mo underlayers, and 70 $^{\circ}\text{C}$, 20 W, 1 min for Ni catalysts, respectively. The deposition rates of the films were 10 nm/min for Mo, and 1 nm/min for Ni. In order to control incident angles of sputtered atoms, aligned fins were placed above substrates during deposition. A schematic configuration of the fins and the metal mask is shown in Fig. 1. Here, “shady side” represents the edges of the patterns that hide behind the mask. And “sunny side” represents the edges that do not hide behind the mask.

CNTs were grown by thermal chemical vapor deposition (TCVD) and DC plasma enhanced chemical vapor deposition (PECVD) method. The reactor tube of the CVD equipment was heated up to 600 $^{\circ}\text{C}$. The background pressure was 0.1 Pa. The flow of H_2 :Ar (10:200 ccm) was introduced into the reactor tube while heating. In the case of a TCVD method, mixture gas of ethylene (C_2H_4): H_2 :Ar (20:10:200 ccm) was introduced into the reactor tube for 30 min for the CNT growth. The total pressure was maintained at 100 kPa. In the case of the PECVD method, the CNT growth was performed by inducing a DC glow discharge and feeding mixture gas of C_2H_4 : H_2 :Ar (5:50:50 ccm). The total pressure was maintained at 2 kPa. The DC plasma was produced by applying bias voltage of -250 V between a substrate holder and grounded anodes apart from the substrates by approximately 5 mm.

The morphology of patterned metals was investigated by an atomic force microscopy (AFM, SII Nanotechnology

Inc. NanoNavi Station). The structure of CNTs was observed by a field emission scanning electron microscope (SEM, Hitachi S-4500) operated at 15 kV.

3. Results and discussion

Fig. 2 shows AFM images ($5 \times 5 \mu\text{m}^2$) of the patterned metal layers just prior to CNT growth. Figs. 2(a) and (b) show the pattern edges of patterned metal layers and the mid areas of the patterned metal, respectively. Fig. 2(c) shows scan areas of Figs. 2(a) and (b). The left of Fig. 2(a) image is the substrate surfaces; the right is the patterned metal layers. At the pattern edges, large Ni particles with a height of ca. 30 nm were observed on small Mo particles with a height of ca. 3 nm. At the mid areas of the pattern (Fig. 2(b)), only a few particles were observed on smooth surfaces.

Fig. 3 shows SEM images of the pattern edges of the patterned metal layers after TCVD varying sputtering conditions. The patterned metal layers of Fig. 3(a) were prepared without aligned fins, Figs. 3(c) and (d) were prepared by installing aligned fins. The optical microscopy (OM) image of the patterned metal, which was sputtered through the fins, is shown in Fig. 3(b). The array of 12 patterns was labeled points A to L as shown in Figs. 1 and 3(b). Figs. 3(c) and (d) show the results on the pattern edges of point D. The images of Fig. 3(c) are the shady side, Fig. 3(d) are the sunny side as shown in Fig. 1. All SEM images revealed that CNTs grew selectively at the region of just inside from the pattern edges which appeared as the white contrast. The diameter of individual CNT was approximately 30 nm. On the contrary CNTs did not grow on the mid areas of the pattern. The position selective growth width of CNTs (W_{CNT}) were (a) 30, (c) 17 and (d) 2.6 μm , respectively. The diameter of the CNTs was similar to that of the Ni particles, which was observed by AFM. At the pattern edges, many small Mo particles were observed under the CNTs. When the fins were installed

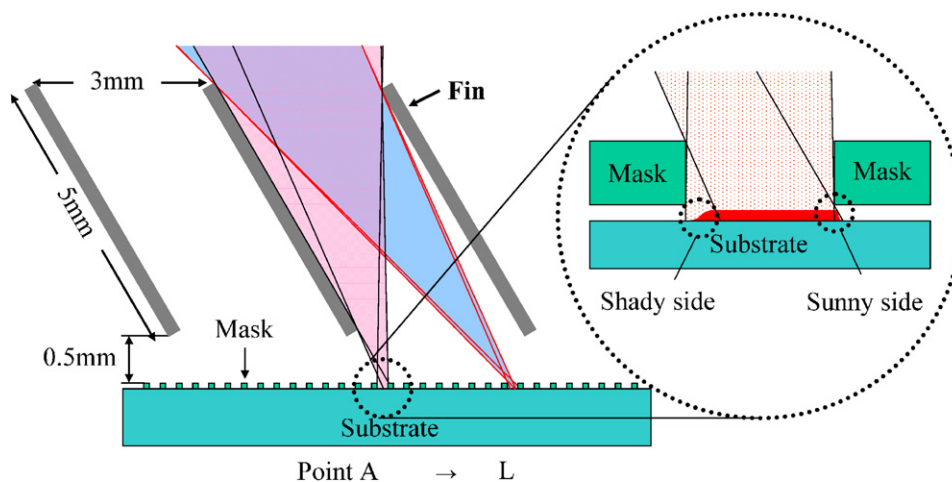


Fig. 1. A schematic configuration of the fins and the metal mask.

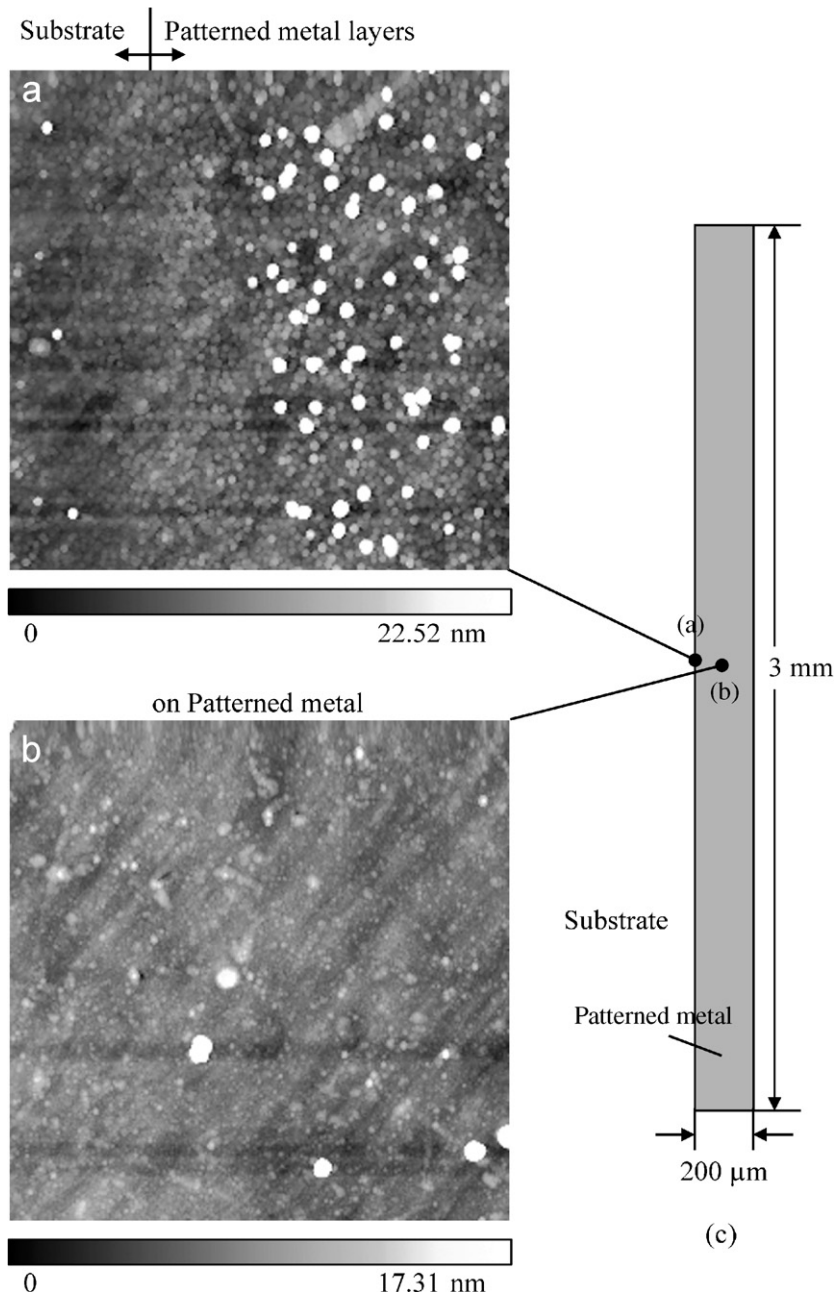


Fig. 2. AFM images ($5 \times 5 \mu\text{m}^2$) of patterned metal layers (a) and (b). The scanning area of the AFM images (c). (a) The pattern edges of patterned metal layers. The left of the AFM image shows the substrate surfaces; the right shows the patterned metal layers. (b) The middle areas of the patterned metal.

(Fig. 3(b)), the contrast of the pattern was not uniform because the thickness of metal pattern was not uniform. Therefore, various thicknesses of metal patterns were appeared simultaneously on this sample. The W_{CNT} in every pattern is summarized in Fig. 4. The gray belts correspond to metal mask patterns, and white belts to the pattern gaps. The results show that the W_{CNT} was narrower in the sunny side than in the shady side. In addition, the W_{CNT} depended on the position of the pattern. The minimum W_{CNT} was $2.6 \mu\text{m}$. This width was approximately one-eightieth of the pattern width.

The position-selective growth of CNTs at the pattern edges was achieved because CNTs grow from only fine particle catalysts. On the smooth surface of Mo underlayers, it is hard for Ni catalysts to become fine particles due to the high wettability. The rough morphology of Mo underlayers resulted in fine particles of Ni catalysts. The rough morphology was observed in very thin Mo regions due to “shadow effect” of a sputtering method. A schematic shadow effect is illustrated in Fig. 5. Sputtered atoms arrive at substrates with various incident angles because of scattering by atmospheric gasses. Then the

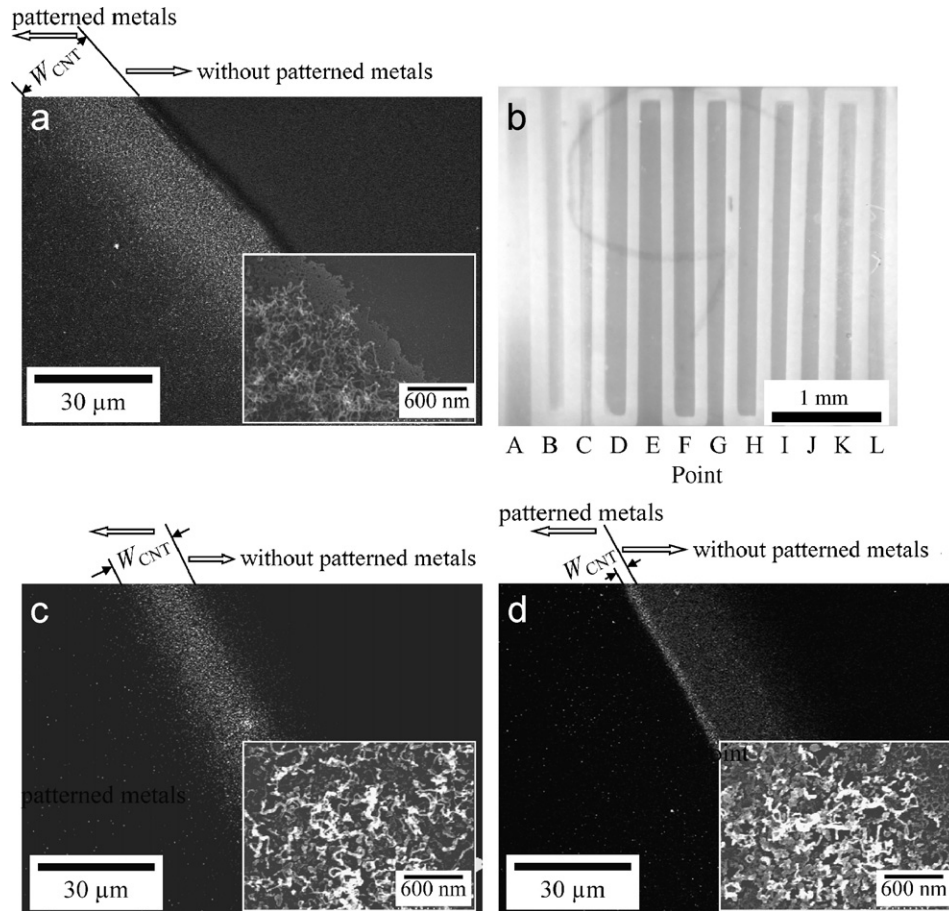


Fig. 3. SEM images of the pattern edges of patterned metal layers after the TCVD at varying sputtering conditions: (a) without aligned fins, (c) “shady side” by aligned fins, and (d) “sunny side” by aligned fins. (b) OM image of the patterned metal. CNTs grew in the narrow region which appeared as the white contrast. The W_{CNT} was about (a) 30, (c) 17 and (d) 2.6 μm . The insets are each the magnified image.

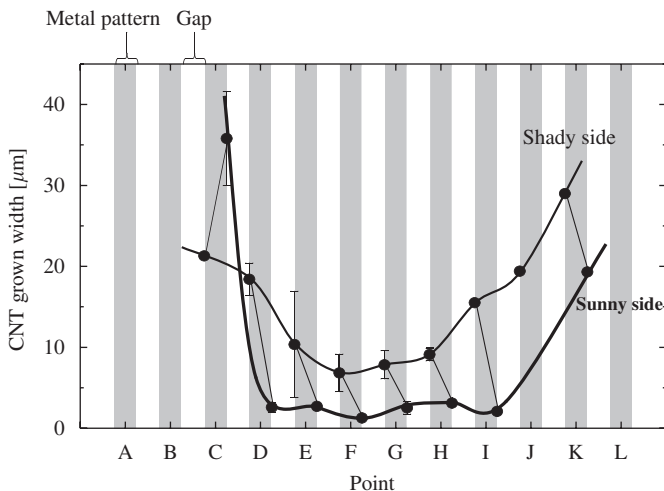


Fig. 4. The W_{CNT} observed at each point in every pattern prepared. The gray belts correspond to the metal mask patterns, and white belts to the pattern gaps.

pattern edges thin down by deposition of particles shaded from the mask pattern. The W_{CNT} depended on the position of the pattern because the thickness of metal pattern was not uniform as shown in Fig. 3(b). By

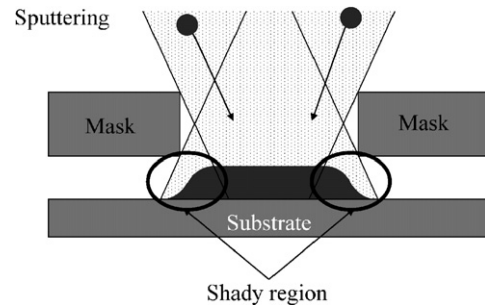


Fig. 5. Schematic “shadow effect” appeared through the mask pattern. The pattern edges thin down by deposition of shaded sputtered atoms under the mask edges (indicated by the oval).

increasing the thickness of the metal pattern, the W_{CNT} decreased because thin regions of Mo decreased. Since the effective widths of the shadow effect depended on the incident angle of sputtered atoms, the W_{CNT} obtained in the sunny side was quite different from that in the shady side. An estimated mean free path of sputtered atoms was ca. 6 mm, and was slightly longer than the fin–substrate distance, 5 mm. The installing of the fins was effective for controlling the incident angles of sputtered atoms and resulted in reducing the W_{CNT} .

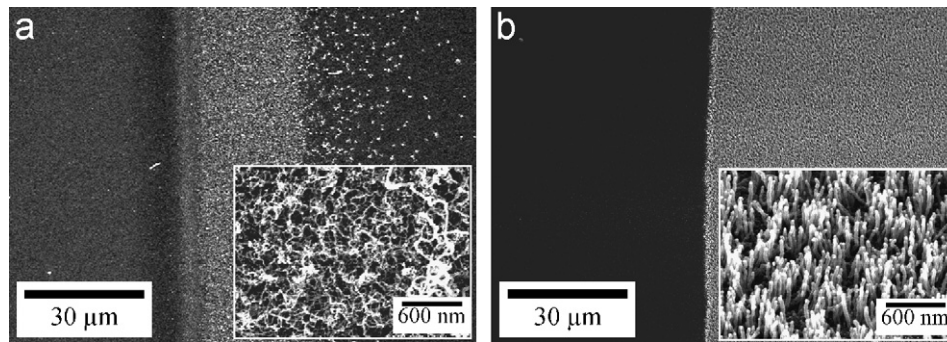


Fig. 6. SEM images of CNTs grown by (a) TCVD only applying bias without a discharge and (b) PECVD with a glow discharge. An applied bias voltage was (a) -300 V (discharge current of about 5 mA) and (b) -250 V (discharge current of about 300 mA). The images of (b) were taken at 45° tilt angle. The insets show magnified images.

In order to obtain VACNTs, electric field was applied during CVD. Fig. 6 shows SEM images of CNTs grown by (a) TCVD only applying bias without a glow discharge and (b) PECVD with a glow discharge accompanied with discharge current. CNTs with a diameter of ca. 15 nm grew in random directions by the TCVD method. The CNTs grew selectively near the boundary of the metal pattern. The effects of the applied bias during TCVD were not observed. In the case of PECVD method, CNTs with a diameter of ca. 30 nm grew up perpendicular to the surfaces. The VACNTs were observed all over the pattern.

The VACNTs were achieved only by PECVD method. When a glow discharge is induced, the voltage drop takes place mostly in the cathode dark space of which the thickness is a few hundreds micrometers. On the other hand, the electric field distributes uniformly in the space between the cathode and the anode in the case of a nondischarge. The gap of electrodes–substrates was about 5 mm. Therefore the electric field applied in the case of PECVD is approximately ten times as large as that in TCVD. CNTs grew up all over the pattern by PECVD whereas the selective growth was observed by TCVD. This result suggests that the Ni catalysts were changed into fine particles by bombardments of ions accelerated in large electric field. As a result CNTs were able to grow even on the smooth metal patterns.

4. Conclusions

We tried to prepare position-selective growth of CNTs and VACNTs on patterned metal. The position-selective growth of CNTs was observed at the edges of the patterned metal by the TCVD. By controlling not only the position of catalysts but also the surface morphology of underlayers, the position selective growth width of CNTs was minimized, approximately $2.6\ \mu\text{m}$. This width was approximately one-eightieth of the patterned metal, $200\ \mu\text{m}$. In

order to prepare VACNTs, DC negative bias voltage was applied to the substrates. When the glow discharge took place in the PECVD, VACNTs were successfully synthesized. The VACNTs grew up, however, all over the patterned metal. Conclusively the selective growth of CNTs was achieved in the optimum conditions of the TCVD by controlling the morphology of the Mo underlayers for Ni catalysts.

Acknowledgments

The authors are grateful for the financial support of the Grant-in-Aid for the Futaba Foundation. This work was supported by the Ministry of Education, Culture, Sports, Science and Technology through a Scientific Grant-in-Aid (no. 15360173).

References

- [1] J. Kong, E. Yenilmez, T.W. Tomblor, W. Kim, H. Dai, R.B. Laughlin, L. Liu, C.S. Jayanthi, S.Y. Wu, *Phys. Rev. Lett.* 87 (2001) 106801.
- [2] Z. Yao, C.L. Kane, C. Dekker, *Phys. Rev. Lett.* 84 (2000) 2941.
- [3] E.W. Wong, P.E. Sheehan, C.M. Lieber, *Science* 277 (1997) 1971.
- [4] J.H. Hafner, C.L. Cheung, C.M. Lieber, *Nature* 398 (1999) 761.
- [5] R. Stevens, C. Nguyen, A. Cassell, L. Delzeit, M. Meyyappan, J. Han, *Appl. Phys. Lett.* 77 (2000) 3453.
- [6] T. Arie, H. Nishijima, S. Akita, Y. Nakayama, *J. Vac. Sci. Technol. B* 18 (2000) 104.
- [7] S. Fan, M.G. Chapline, N.R. Franklin, T.W. Tomblor, A.M. Cassell, H. Dai, *Science* 283 (1999) 512.
- [8] N. Saurakhiya, Y.W. Zhu, F.C. Cheong, C.K. Ong, A.T.S. Wee, J.Y. Lin, C.H. Sow, *Carbon* 43 (2005) 2128.
- [9] W.I. Milne, K.B.K. Teo, G.A.J. Amaratunga, R. Lacerda, P. Legagneux, G. Pirio, V. Semet, V.T. Binh, *Curr. Appl. Phys.* 4 (2004) 513.
- [10] A.C. Dupuis, *Prog. Mater. Sci.* 50 (2005) 929.
- [11] V.I. Merkulov, A.V. Melechko, M.A. Guillorn, D.H. Lowndes, M.L. Simpson, *Appl. Phys. Lett.* 79 (2001) 2970.

Selective Chemical Vapor Growth of Carbon Nanotubes for Application of Electronic-Measuring Nano-Probes

Hiroki Okuyama, Nobuyuki Iwata and Hiroshi Yamamoto
College of Science and Technology, Nihon University, Chiba, Japan

ABSTRACT

Selectively grown carbon nanotubes (CNTs) and/or vertically aligned CNTs (VACNTs) on patterned metal electrodes have been prepared for applications to a novel electronic-measuring nano-probe. We propose newly a position-controlling method of CNTs by controlling not only a position of catalysts but also the thickness of metal underlayers for the catalysts. The selective growth of CNTs was achieved at edges of the metal pattern by thermal chemical vapor deposition. The width of selectively grown CNTs was minimized, about 2.6 μm . The width was about 80 times as small as that of the metal pattern. VACNTs were synthesized by a plasma enhanced CVD method in which the high electric field in a cathode dark space was applied to the substrates. The VACNTs grew up, however, all over the metal pattern.

INTRODUCTION

Carbon nanotubes (CNTs) have attracted much attention because of many featured characteristics. High electric conductivity [1] and high permissible current density [2] are suitable for electronic devices. CNTs grow selectively from catalyst particles by using chemical vapor deposition (CVD) [3]. CNTs have a high aspect ratio and their growth direction is controllable by applying electric field during CVD growth [4]. These characteristics are available to fabricate various kinds of nanostructures. CNTs reveal high mechanical strength in spite of high flexibility [5]. Therefore we are aiming at realizing a novel nano-probe with CNTs which enables to approach it toward contact points on specimen easily without an accurate control for measuring of electric transport properties. The control for position and direction of CNTs is necessary in order to prepare the nanoscaled CNTs electronic devices. Furthermore electrically and mechanically firm contacts between CNTs and metal electrodes are needed.

In this work, we tried to prepare selectively grown CNTs and vertically aligned CNTs (VACNTs) on patterned metal electrodes for realization of the novel electronic measuring nano-probe. The selectively grown CNTs are prepared by using the two characteristics as follows. One is that the CNTs grow selectively from fine particle catalysts. The other is that

we can control the synthesis of the fine particle catalysts by noticing wettability between metal interfaces. Since wettability of metal interface is high, it is hard to form fine particles as overlayers on smooth underlayers. When the surfaces of underlayers are rough, overlayered metals form fine particles. Therefore we propose newly a position-controlling method of CNTs by controlling not only a position of catalysts but also a surface morphology of metal underlayers.

EXPERIMENTAL

In the first place Ni catalysts and Mo underlayers were deposited on quartz substrates through a metal mask (thickness: 30 μm , pattern width: 200 μm , gap: 100 μm) by RF magnetron sputtering. A background pressure of the chamber was 1.0×10^{-2} Pa, and the pressure during deposition was fixed at 2.0 Pa by feeding Ar gas. The growth conditions were 120 $^{\circ}\text{C}$ of substrate temperature, 50 W of sputtering power, 1 min of sputtering time for Mo underlayers, and 70 $^{\circ}\text{C}$, 20 W, 1 min for Ni catalysts, respectively.

CNTs were grown by thermal chemical vapor deposition (TCVD) and dc plasma enhanced chemical vapor deposition (PECVD) method. The reactor tube of the CVD equipment was heated up to 600 $^{\circ}\text{C}$. The flow of H_2 : Ar (10 : 200 ccm) was introduced into the reactor tube while heating. The background pressure was 0.1 Pa. In the case of a TCVD method, mixture gas of ethylene (C_2H_4) : H_2 : Ar (20 : 10 : 200 ccm) was introduced into the reactor tube for 30 min for the CNT growth. The total pressure was maintained at 100 kPa. In the case of a PECVD method, the CNT growth was performed by inducing a dc glow discharge and feeding mixture gas of C_2H_4 : H_2 : Ar (5 : 50 : 50 ccm). The total pressure was maintained at 2 kPa. The dc plasma was produced by applying bias voltage of -250 V between a substrate holder and grounded anodes which apart from the substrates by about 5 mm. The patterned metal electrodes were connected electrically to the substrate holder.

RESULTS AND DISCUSSION

Figure 1 shows SEM images of the edge boundary of the patterned metal layers after TCVD deposition. CNTs grew selectively on just insides from the pattern edges where thickness of Mo underlayers varied gradually. In the CNT grown region the surfaces of Mo layers were rough and porous. On the contrary CNTs didn't grow on the mid areas of the pattern where the surfaces of Mo layers were smooth. By increasing Mo deposition time from 1 min to 3 min, the

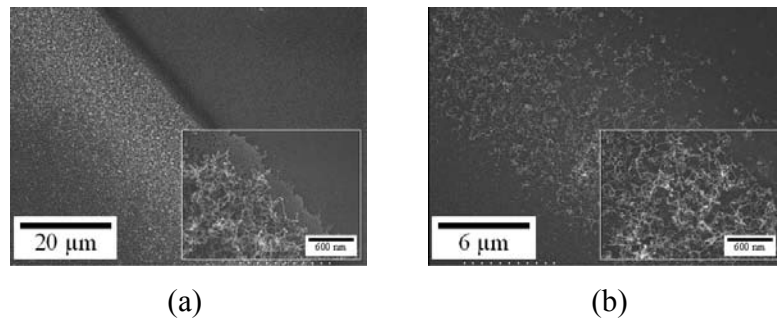


Figure 1. SEM images of the edge boundary of patterned metal layers after the TCVD deposition. Sputtering time of the Mo layers was (a) 1 min and (b) 3 min. The upper-right of the image is the substrate surfaces, the lower-left is the patterned metal layers. CNTs grew in the narrow region which appeared as the white contrast. The W_{CNT} was about (a) 30 μm and (b) 6.3 μm . The insets are each the magnified image.

widths of selectively grown CNTs, W_{CNT} decreased from 30 μm to 6.3 μm .

The selective growth of CNTs at the pattern edges was achieved because CNTs grow from only fine particle catalysts. On the smooth surface of Mo underlayers, Ni catalysts don't become fine particles due to the high wettability. The rough morphology of Mo underlayers resulted in fine particles of Ni catalysts. The rough morphology was appeared in very thin regions of Mo due to "shadow effect" of a sputtering method. A schematic shadow effect is illustrated in figure 2. Sputtered atoms arrive at substrates with various incident angles because of scattering by atmospheric gasses. Then the pattern edges thin down by deposition of particles shaded from the mask pattern. Since the rough regions of thicker Mo underlayers became narrow, the W_{CNT} decreased by increasing Mo thickness.

Aligned fins were installed during deposition to control incident angles of sputtered atoms. A schematic configuration of the fins and the metal mask is shown in figure 3 (a). And optical microscopy image of the specimen, which was prepared by installing the fins, is shown in figure 3 (b). The contrast of the pattern was not uniform. Figure 4 shows SEM images of the pattern boundary after TCVD by installing the fins during Mo deposition. The W_{CNT} in every pattern is summarized in figure 5. The gray belts correspond to metal mask patterns, and white belts to the pattern gaps. The results show that the W_{CNT} was narrower in "sunny side" than in "shady

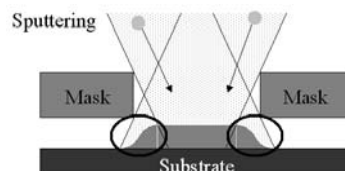


Figure 2. Schematic "shadow effect" appeared through the mask pattern. The pattern edges thin down by deposition of shaded sputtered atoms under the mask edges (indicated by the oval).

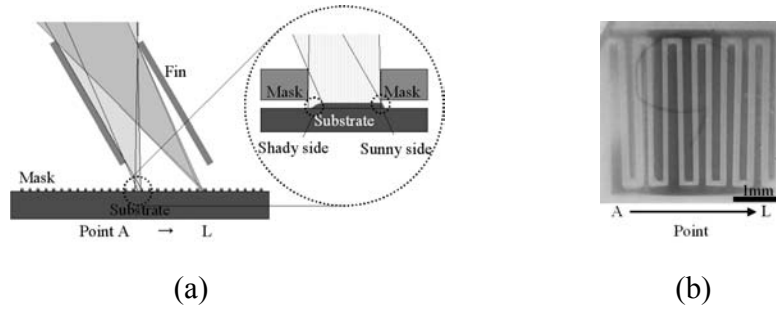


Figure 3. A schematic configuration of the aligned fins and the mask (a). An optical microscopy image of the specimen prepared by installing the fins (b).

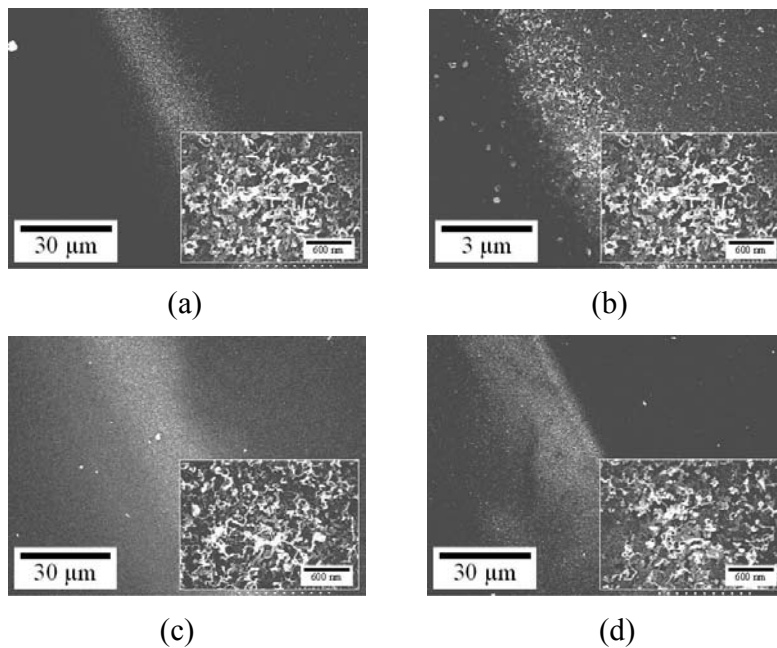


Figure 4. Typical SEM images of the pattern boundary after TCVD by installing the fins: (a) and (b) show the results on the edges of point D, (c) and (d) on point K. The images of (a) and (c) are the “shady side” and the upper-right of the image is the metal pattern. The images of (b) and (d) are the “sunny side” and the lower-left of the image is the metal pattern. CNTs grew in the narrow region which appeared as the white contrast. The W_{CNT} was (a) 17 μm , (b) 2.6 μm , (c) 29 μm and (d) 19 μm . The inset shows each the magnified images.

side”. In addition, the W_{CNT} depended on the position of the pattern. The minimum W_{CNT} was 2.6 μm . This width was about 80 times as small as the pattern width.

The W_{CNT} depended on the position of the pattern because the thickness of metal pattern was not uniform as shown in figure 3 (b). By increasing the thickness of the metal pattern, the W_{CNT} decreased as discussed above. Since the effective widths of the shadow effect depended on the incident angle of sputtered atoms, the W_{CNT} obtained in “sunny side” was quite different from

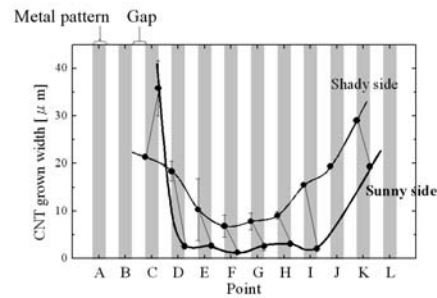


Figure 5. The W_{CNT} observed at each the points in every patterns prepared. The gray belts correspond to the metal mask patterns, and white belts to the pattern gaps.

that in “shade side”. An estimated mean free path of sputtered atoms was 6 mm, and was slightly longer than the fin-substrate distance, 5 mm. The installing of the fins was effective for controlling the incident angles of sputtered atoms and resulted in reducing of the W_{CNT} .

Figure 6 shows SEM images of CNTs grown by (a) TCVD only applying bias without a glow discharge and (b) PECVD with a glow discharge accompanying with discharge current. CNTs with a diameter of *ca.* 15 nm grew in random directions by the TCVD method. The CNTs grew selectively at near the boundary of the metal pattern. The effects of the applied bias during TCVD were not observed. In the case of PECVD method, CNTs with a diameter of *ca.* 30 nm grew up perpendicular to the surfaces. The VACNTs were observed all over the pattern.

The VACNTs were achieved only by PECVD method. When a glow discharge is induced, the voltage drop takes place mostly in the cathode dark space of which the thickness is few hundreds μm . On the other hand, the electric field distributes uniformly in the space between the cathode and the anode in the case of a non-discharge. The gap of electrodes-substrates was about 5 mm. Therefore the electric field applied in the case of PECVD is approximately ten times as large as that in TCVD. CNTs grew up all over the pattern by PECVD whereas the

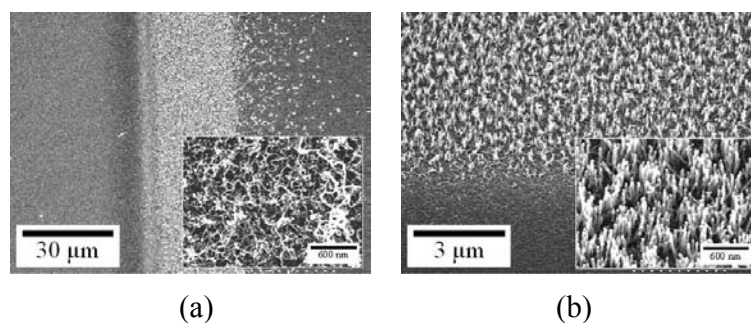


Figure 6. SEM images of CNTs grown by (a) TCVD only applying bias without a discharge and (b) PECVD with a glow discharge. An applied bias voltage was (a) -300 V (discharge current of about 0.005A) and (b) -250 V (discharge current of about 0.3A). The images of (b) were taken at 45° tilt angle. The inset shows magnified images.

selectively growth was observed by TCVD. This result may suggest that the Ni catalysts were changed into fine particles by bombardment of ions accelerated in large electric field. As a result CNTs were able to grow even on the smooth metal patterns.

CONCLUSIONS

We tried to prepare CNTs and VACNTs grown selectively on patterned metal electrodes. The selectively grown CNTs were observed at the edges of the patterned metal by the thermal CVD. By controlling not only a position of catalysts but also a surface morphology of underlayers, the width of selectively grown CNTs was minimized, about 2.6 μm . The width of the CNTs was about 80 times as small as that of the pattern metal. In order to prepare VACNTs, dc negative bias voltage was applied to the substrates. When the glow discharge took place in the plasma enhanced CVD, VACNTs were successfully synthesized due to the high electric field in the cathode dark space. The VACNTs grew up, however, all over the metal pattern. Conclusively a selective growth of CNTs was achieved in the optimum conditions of the thermal CVD by controlling the thickness of the Mo underlayers for Ni catalysts. It is the future subject to obtain selectively grown VACNTs on the designated region of metal patterns.

ACKNOWLEDGMENTS

The authors are grateful for the financial support of the Grant-in-Aid for the Futaba Foundation. This work was supported by the Ministry of Education, Culture, Sports, Science and Technology through a Scientific Grant-In-Aid (No.15360173).

REFERENCES

1. J. Kong, E. Yenilmez, T. W. Tombler, W. Kim, H. Dai, R. B. Laughlin, L. Liu, C. S. Jayanthi and S. Y. Wu, *Phys. Rev. Lett.* **87**, 106801 (2001)
2. Z. Yao, C. L. Kane and C. Dekker, *Phys. Rev. Lett.* **84**, 2941 (2000)
3. A. C. Dupuis, *Prog. Mater. Sci.* **50**, 929 (2005)
4. V. I. Merkulov, A. V. Melechko, M. A. Guillorn, D. H. Lowndes and M. L. Simpson, *Appl. Phys. Lett.* **79**, 2970 (2001)
5. E. W. Wong, P. E. Sheehan and C. M. Lieber, *Science*, **277**, 1971 (1997)

Synthesis of C₆₀ Polymer by Free Electron Laser Irradiation with Hole-Doping Effect

Shingo Ando, Ryo Nokariya, Reou Koyaizu, Nobuyuki Iwata, and Hiroshi Yamamoto
College of Science & Technology, Nihon University, 7-24-1 Narashinodai, Funabashi-shi, Chiba, 274-8501, Japan.
Tel & Fax: 81-047-469-5457, e-mail: 2005_ando@yamamoya.eccs.cst.nihon-u.ac.jp

A free electron laser (FEL) with wavelength of 450nm and 345nm and YAG laser with wavelength of 532nm were irradiated to surfaces of moderately compressed pure C₆₀ and a mixture of C₆₀ and I₂ in vacuum. After laser irradiation the Raman peak of Ag(2)-derived vibration mode of C₆₀ sifted to the lower energy side. By 450nm FEL irradiation the Raman shift of a mixture C₆₀+I₂ was as large as *ca.* 8cm⁻¹ and was definitely larger than that of pure C₆₀. By 450nm FEL irradiation the decreased in (111) lattice spacing of C₆₀ in the mixture sample was by *ca.* 8x10⁻³ nm. The obtained results strongly suggest that 3-dimensional polymerization of C₆₀ was effectively induced by laser irradiation and/or addition of iodine.

Key words: C₆₀, polymerization, free electron laser (FEL), Raman spectrum, Ag(2)-mode, hole doping

1. INTRODUCTION

Since the polymerization of C₆₀ films was successfully done first by a phototransformation [1], many studies have been carried out for fullerene polymerization processes using such as electron-beam irradiation [2], high-pressure [3], plasma-induced excitation [4], and so on. By adequate chemical or physical excitations a carbon double bond in a hexagon of a C₆₀ cage breaks and transforms into an inter-molecular four-bond ring with a neighbor molecule. As the result two C₆₀ molecules are combined and changed into a dimmer or some higher order of polymers. This is the fundamental process for fullerene polymerization.

The polymerized fullerite structures based on a "2+2 cycloaddition" bonding [1] have been observed experimentally and theoretically [5-7]. It was known about the polymer structure that one-dimensional (1D) chains are in an orthorhombic phase and two-dimensional (2D) planes include a tetragonal and a rhombohedral phase. Only a few experiments [3] have been reported about the possibility of a three-dimensional (3D) polymerized phase. The 3D fullerene polymers are expected, however, to become extremely hard, with lower density and less brittleness than diamond.

The conventional polymerization proceed by high compression at the order of GPa or heating up to higher than a thousands degrees [3]. But these polymerization processes are unsuitable to supply sufficiently large 3D polymers for applications. Furthermore the C₆₀ cages are partially collapsed under extremely high-pressure conditions and the processes are not well-controlled.

The purpose of this work is to develop a novel photon-assisted process for synthesis of 3D C₆₀ polymers by Free Electron Laser (FEL) or YAG laser irradiation under moderately high pressure. The absorption spectrum of C₆₀ revealed large absorption peaks in 221nm, 271nm and 347nm, or small absorption peaks in neighborhood 400~500nm [8]. Then the wavelength of laser irradiated was changed in the range

350~600nm. Especially we studied FEL with wavelength of 450nm and 345nm, and also YAG with wavelength of 532nm. Furthermore, we have noticed a hole-doping effect which was demonstrated in the synthesis of diamond from graphite [9]. A mixture of C₆₀ and I₂ was also studied in comparison with the case of pure C₆₀ as pristine powder was irradiated.

Hereinafter, the developed photon-assisted process is introduced and the possibility of synthesis of 3D C₆₀ polymers by laser irradiation will be demonstrated.

2. EXPERIMENTAL

Figure 1 shows the schematic apparatus for the synthesis of C₆₀ polymers. The vacuum chamber was evacuated to *ca.* 10⁻⁴ Pa by a turbo molecular pump and was pre-annealed at *ca.* 400K for 3h. The two kinds of pristine powder were studied. The pure C₆₀ (99.95%) was a commercial product. The C₆₀ was also mixed with I₂ in the mole ration, 1:4. Iodine was adopted for the enhancement of polymerization reactions expected from the hole doping effect as stated before. The effect is expected to be applicable to polymerization reactions of C₆₀ molecules because of the mutually similar structures of carbon networks in graphite and C₆₀. Here we aimed to promote electron transfers from C₆₀ to iodine atoms by the photon-excitation because the electron affinity of the C₆₀ is high.

The powder was set in an anvil which was placed in the vacuum and was pressed via a bellows by a hydraulic press. The pressure, the maximum of *ca.* 600MPa, was applied to the sample powder by the quartz window.

Laser was introduced to the surfaces of the compressed powder by aluminum cold mirrors which reflect only lights with the wavelength less than, *ca.* 700nm. When the wavelength of FEL was chosen by changing the fundamental wavelength, laser was guided to specimen surfaces through the band pass filter (BPF).

Infrared (wavelength of few tens μm) FEL has been developed and applied to many researches of the

laser-solid interaction [10]. On the other hand we adopted here a newly developed FEL system which generated a tunable near-infrared laser and the higher harmonics with comparatively high power. The details of the FEL system used appeared in the elsewhere [11]. A few tens microsecond macro-pulse, which included few hundreds picosecond micro-pulses, was repeated in 2Hz. The power of the fundamental macro-pulse was *ca.* 0.5mJ/pulse. Since the FEL can supply a laser with a tunable wavelength, the fundamental wavelength was changed arbitrarily in this work. The laser mainly used was the third harmonics (*ca.*450nm) of *ca.* 1350nm fundamental FEL or the fifth harmonics (*ca.*345nm) of *ca.* 1700nm. The wavelength of about 450nm of which the value is evaluated from the difference of the bonding energy of C=C double bond and C-C bond. The irradiation time was 60~180 min.

Furthermore, YAG laser (*ca.*532nm) was irradiated as the second harmonics of *ca.*1064nm fundamental laser. The irradiation power was 1.6mJ/pulse and the irradiation time was 60min.

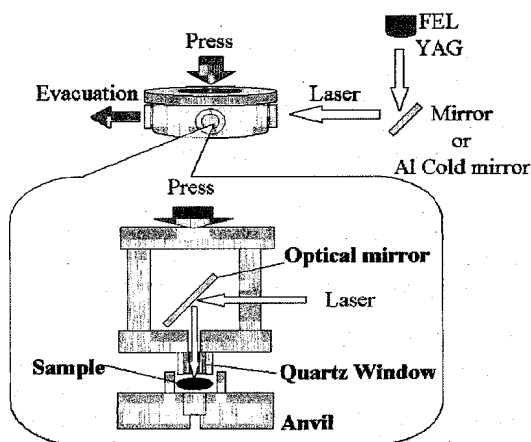


Figure 1. Schematic apparatus constructed for synthesis of C_{60} polymers. The compressed surfaces of the sample were irradiated using a laser by the quartz window. Aluminum cold mirrors were used for high reflectance of visible laser (wavelength less than *ca.*700nm) and for cutting near-infrared lights. The quartz ensures high transmittance of greater than 95% of visible light.

The obtained samples were 5-mm-diameter disks with thickness of less than 0.5mm. They were brought in a vacuum case to prevent contamination from air. Raman microscopic spectroscopy (Renishaw plc. SYSTEM1000) was used to study molecular vibration spectra. The light source for excitation was Ar ion laser with wavelength of 514.5nm. Crystalline

structures were studied using reflective X-ray diffraction (XRD) (Rigaku Corp. RAD-C) with $CuK\alpha 1$ x-rays.

3. RESULT & DISCUSSION

Figure 2 shows the change of the lattice parameter of (111) planes of samples irradiated by 350~600nm FEL through the BPF under atmospheric pressure. The lattice parameter of C_{60} and $C_{60}+I_2$ samples irradiated by 500nm FEL decreased by *ca.* 1.1×10^{-2} nm and *ca.* 1.2×10^{-2} nm, respectively. These results revealed that the polymerization reactions were effectively induced by irradiation of FEL with wavelength of about 500nm. Then covalent binding between C_{60} molecules took place and the decline of the crystal structure proceeded.

Figure 3 shows Raman peaks of the $Ag(2)$ -derived mode in the case of 532nm YAG laser irradiation. The wave number of the peak of the non-irradiated pristine C_{60} was 1466.1cm^{-1} , whereas that of the irradiated C_{60} changed to 1462.9cm^{-1} with decrement by *ca.* 3cm^{-1} . On the other hand, the irradiated mixture of $C_{60}+I_2$ revealed the peak wave number of 1460.0cm^{-1} . The Raman shift was as large as *ca.* 6cm^{-1} . The half-width of the Raman peak also increased in correspondence to the amount of the peak shift.

Figure 4 shows typical Raman peaks of the $Ag(2)$ -derived mode in the case of 450nm FEL irradiation. The wave number of the peak of the non-irradiated pristine C_{60} was 1463cm^{-1} . The irradiated C_{60} showed the wave number of 1460cm^{-1} with a decrement by *ca.* 3cm^{-1} . The irradiated mixture of $C_{60}+I_2$ revealed the larger Raman shift as large as *ca.* 8cm^{-1} . The half-width of the Raman peak increased by irradiation.

The ultraviolet laser caused somewhat different changes of the Raman spectrum. Figure 5 shows Raman peaks of the $Ag(2)$ -derived mode in the case of 345nm FEL irradiation. Double splitting of the peak was observed. Since the optical absorption of C_{60} at 345nm is about three times higher than that at 450nm, polymerization reactions proceeded better in the thinner region of sample surfaces by 345nm irradiation than by 450nm. Consequently, the Raman peak from non-polymerized C_{60} also remained in this case. The maximum amount of the Raman shift attained up to *ca.* 10cm^{-1} in the $C_{60}+I_2$ sample. Then the large decrease and broadening of the peak were also observed.

The results of these Raman shifts were summarized in Table 1. As well known the Raman peak broadens and shifts to the lower-energy side according to the progress of polymerization. Then the $Ag(2)$ -derived mode is noted as an index of the polymerization reaction progress. It is suggestive that the change of the Raman peak of the $C_{60}+I_2$ sample was definitely larger than that of pure C_{60} . This result indicates that some additional

Table 1. The conditions of laser irradiation and observed the Raman peak shift.

Pristine Powder	Laser	Wavelength [nm]	Laser Power [mJ/Pulse]	Irradiation Time [min]	$Ag(2)$ peak shift [cm^{-1}]
C_{60}	FEL	450 (3rd)	0.5	300	3.0
$C_{60}+I_2$	FEL	450 (3rd)	0.5	300	7.6
C_{60}	FEL	345 (5th)	2	120	7.6
$C_{60}+I_2$	FEL	345 (5th)	2	120	9.7
C_{60}	YAG	532 (2nd)	1.6	60	3.2
$C_{60}+I_2$	YAG	532 (2nd)	1.6	60	6.0

mechanisms work for promotion of polymerization by addition of I₂. It can be interpreted that photo-excited electrons of C₆₀ molecules transfer to iodine atoms: hole doping into C₆₀ molecules takes place.

The hole-doping effect was also confirmed through crystalline structure analyses. Figure 6 shows typical XRD patterns of samples irradiated using 450nm FEL. After the irradiation the main diffraction peak (111) markedly decreased and broadened in the case of the C₆₀+I₂ sample. Especially the lattice spacing of (111) planes of the irradiated C₆₀ and C₆₀+I₂ sample were smaller by *ca.*7×10⁻³nm and *ca.*8×10⁻³nm, respectively, than that of the non-irradiated C₆₀. The results suggest that covalent bondings between C₆₀ molecules took place and the decline of the crystalline structure progressed according to polymerization reactions induced by laser irradiation and/or addition of iodine.

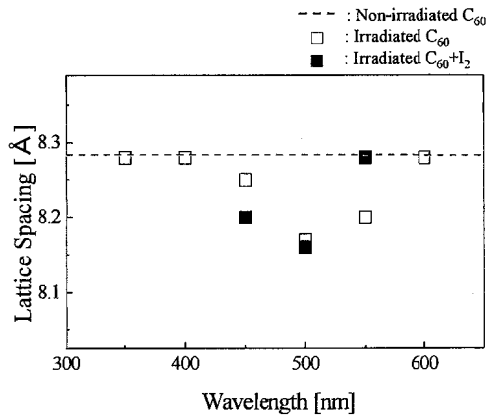


Figure 2. Observed lattice spacing of C₆₀ (111) of the sample after 350–600nm FEL irradiation under atmospheric pressure in vacuum. The open square and closed one show the results of C₆₀ and C₆₀+I₂ sample, respectively.

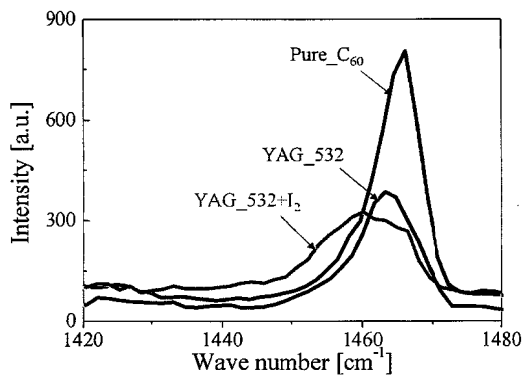


Figure 3. Raman peaks of the Ag(2)-derived vibration modes observed in the three samples: non-irradiated pristine C₆₀, C₆₀, and C₆₀+I₂ irradiated by 532nm YAG laser.

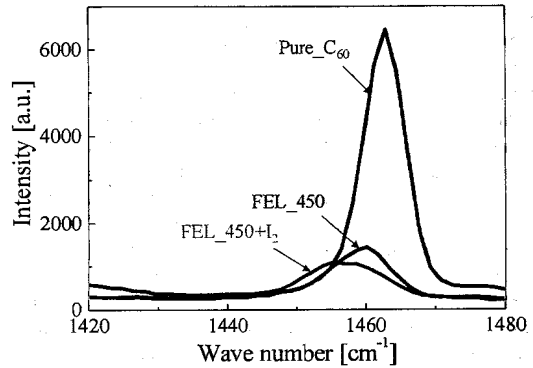


Figure 4. Raman peaks of the Ag(2)-derived vibration modes observed in the three samples: non-irradiated pristine C₆₀, C₆₀, and C₆₀+I₂ irradiated by 450nm FEL.

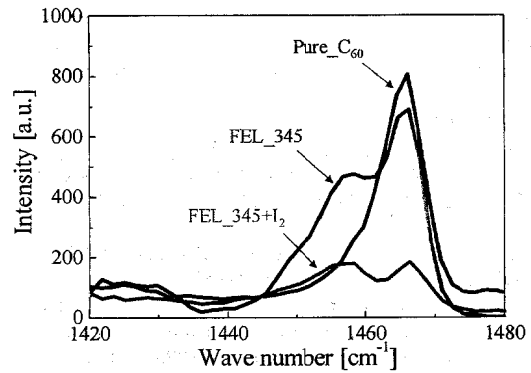


Figure 5. Raman peaks of the Ag(2)-derived vibration modes observed in the three samples: non-irradiated pristine C₆₀, C₆₀, and C₆₀+I₂ irradiated by 345nm FEL.

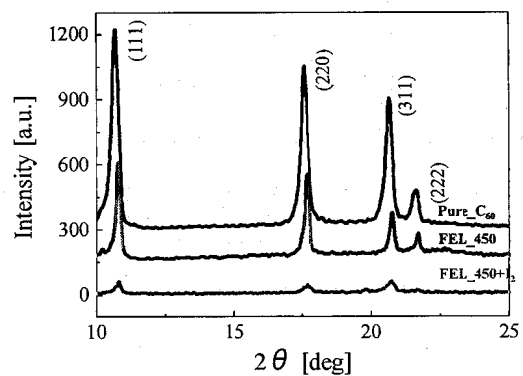


Figure 6. XRD patterns of the three samples: non-irradiated pristine C₆₀, C₆₀, and C₆₀+I₂ irradiated by 450nm FEL. The inset index corresponds to each fcc plane of C₆₀. The (111) peak intensity of the irradiated C₆₀+I₂ decreased remarkably.

4. CONCLUSION

The 450nm or 345nm FEL and 532nm YAG laser were irradiated to surfaces of compressed C_{60} or $C_{60}+I_2$ powder in vacuum. After laser irradiation the C_{60} Raman peak of the $A_g(2)$ -derived mode clearly shifted to the lower energy side and/or the half-width of the peak became broad. Also the lattice parameter of C_{60} decreased and the crystalline structure was declined by 450nm FEL irradiation. These characteristic changes in the $C_{60}+I_2$ sample were more distinct than those in C_{60} powder. Conclusively the obtained results suggest that the 3D polymerization of C_{60} was effectively promoted using laser irradiation and/or the effect of the photon-assisted hole-doping from iodine to C_{60} molecules. The detailed characterization of the obtained samples is a subsequent work.

ACKNOWLEDGEMENTS

This work is partly supported by "Academic Frontier" Project for Private Universities: matching fund subsidy from MEXT, 200-2007.

The authors would like to thank the staff members of Laboratory for Electron Beam Research and Application of Nihon University for their helps of FEL operations.

REFERENCE

- [1] A. M. Rao, Ping Zhou, Kai-An Wang, G. T. Hager, Yang Wang, W-T. Lee, Xiang-Xin Bi, P. C. Eklund, D. S. Crnett, M. A. Duncan and I. J. Amster: *Science* 259 (1993) 955.
- [2] Y. B. Zhao, D. M. Poirier, R. J. Pechman and J. H. Weaver: *Appl. Phys. Lett.* 64 (1994) 577.
- [3] H. Yamawaki, M. Yoshida, Y. Kakudate, S. Usuba, H. Yokoi, S. Fujiwara, K. Aoki, R. Ruoff, R. Malhotra and D. C. Lorents: *J. Phys. Chem.* 97 (1993) 11161.
- [4] N. Takahashi, H. Dock, N. Matsuzawa and M. Ata: *J. Appl. Phys.* 74 (1993) 5790.
- [5] A. M. Rao, P. C. Eklund, J-L. Hodeau, L. Marques and M. Nunez-Regueiro: *Phys. Rev. B* 55 (1997) 4766.
- [6] V. A. Davydov, L. S. Kashevarova, A. V. Rakhmanina, V. Agafonov, H. Allouchi, R. Ceolin, A. V. Dzyabchenko, V. M. Senvavin and H. Szwarc: *Phys. Rev. B* 58 (1998) 14786.
- [7] X. Chen, S. Yamanaka, K. Sako, Y. Inoue and M. Yasukawa: *Chem. Phys. Lett.* 356 (2002) 291.
- [8] S. Kazaoui, R. Ross and N. Minami: *Solid State Commun.* 90 (1994) 623.
- [9] H. Nakayama, H. Katayama and H. Yoshida: *Jpn. J. Appl. Phys.* 41 (2002) 817.
- [10] H. P. Freund and J. T. M. Antonsen: *Principle of Free-Electron Lasers*, Chapman & Hall, London, 1992.
- [11] Y. Hayakawa, I. Sato, K. Hayakawa, T. Tanaka, K. Yokoyama, T. Sakai, K. Kanno, K. Ishiwata and E. Hashimoto: *Nucl Instr And Meth*, A507 (2003) 404.

(Received January 10, 2007; Accepted August 23, 2007)

Preparations of magnetoelectric thin films for superconducting devices

N. Iwata *, T. Asada, K. Nagase, T. Yamada, H. Yamamoto

Department of Electronics and Computer Science, College of Science and Technology, Nihon University, 7-24-1 Narashinodai, Funabashi-shi, Chiba 274-8501, Japan

Received 30 October 2006; accepted 9 February 2007
Available online 26 May 2007

Abstract

Representative magnetoelectric (ME) Cr_2O_3 thin films were grown on *R*-cut sapphire and $\text{SrTiO}_3(100)$ substrate in order to integrate with high temperature superconductor oxides. The replacement of a base current and stabilization of I_C spread for single flux quantum device is expected. Highly oriented Cr_2O_3 thin film grew on sapphire at 550 °C by off-axis DC–RF hybrid magnetron sputtering method with two-in. Cr metal target. The surface was composed of coalesced rectangular grains, the surface roughness R_a of which was 1.9 nm. Estimated induced magnetic field with electric field applied of 0.24 MV/cm was 1.0 G around 40 K.

© 2007 Elsevier B.V. All rights reserved.

PACS: 68.55.–a; 81.15.–z; 81.15.Cd

Keywords: Magnetoelectric effect; Cr_2O_3 ; Single flux quantum; Thin film

1. Introduction

We pay attention to apply the magnetoelectric (ME) materials of single phase compounds to single flux quantum (SFQ) device integrated by high critical temperature (high- T_c) superconductors [1–4]. The ME effect is defined as the dielectric polarization of a material in an applied magnetic field or an induced magnetization in an external electric field [1–4]. The performance of the SFQ device is featured as a high-speed (over 100 GHz) and low consumption (less than 100 nW/gate) following Si digital devices. However, increasing integration degree, large amount of base current is required, which give rise to uncontrollable operation due to accompanying magnetic field. In addition, to reduce the fluctuation of critical current (I_C) and to stabilize the device operation, working temperature is limited less than 40 K.

As shown in the Fig. 1, we propose a novel element how the ME material is embedded in a SFQ device. Since the ME material is grown to generate a base current, the base current is localized and then error operations could be reduced. It is expected that a base current in a SFQ device is replaced by the ME materials. The electric power loss from a current source is excluded. Furthermore, considering critical current I_C of the Josephson junction is modulated by the magnetic field penetrating the junction area, I_C spread of the junctions could be reduced by the induced magnetic field from the ME film. We expect that a larger-scale circuit is achievable by the induced and localized magnetic field from ME materials integrated with SFQ devices.

In this paper, we have focused on an antiferromagnetic insulator Cr_2O_3 which is a representative oxide among ME single phase compounds. Cr_2O_3 has the linear ME susceptibility of α_{xx} , α_{yy} and α_{zz} and the others are zero [1–4]. Magnetic field is induced along the direction of electric field applied. Since the ME effect is derived from a magnetic superexchange interaction, highly oriented ME films are claimed on SrTiO_3 (STO), MgO, sapphire, etc., to integrate with high- T_c superconductors.

* Corresponding author. Tel./fax: +81 47 469 5457.
E-mail address: iwata@ecs.cst.nihon-u.ac.jp (N. Iwata).

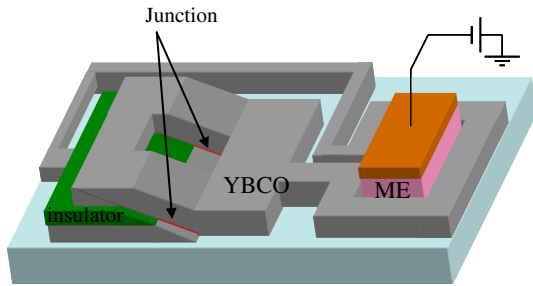


Fig. 1. Schematic image of a part of the SFQ device with ME material we propose. Induced magnetic field from the ME film generates the shielding current along the high- T_c superconductor. Shielding current could be a base current for operation of SFQ device.

2. Experimental

Cr_2O_3 films were grown by off-axis DC–RF hybrid magnetron sputtering method with two-in. Cr metal target on the substrates of R -cut sapphire and STO with CeO_2 buffer layer. Substrates surface of sapphire was etched by HF acid for 10 s ($\text{HF}:\text{H}_2\text{O} = 1:7$) and then annealed at 1000 °C for 12 h in air in advance. For Cr_2O_3 growth substrate temperatures, DC current, RF power and sputtering gas were 300–630 °C, 0.04 A, 100 W and 0.26 Pa ($\text{Ar}:\text{O}_2 = 4:1$), respectively. CeO_2 buffer layer was deposited by on-axis RF magnetron sputtering method with pressed CeO_2 powder at 380 °C. The substrate was 0.5 wt.% Nb-doped STO(100). A post-annealing was carried out at 1000 °C for 4 h in air prior to growth of Cr_2O_3 .

The X-ray diffraction (XRD) 2θ – θ scans from 5° to 90°, using Rigaku RAD-C system with $\text{Cu K}_{\alpha 1}$ and $\text{K}_{\alpha 2}$ radiation generated with a tube power of 40 kV and 30 mA, examined the grown films. The diffraction area was always same with divergence slit of $1/2^\circ$ and sample size of $5 \times 10 \text{ mm}^2$. The surface morphology was observed in a dynamic force mode by an atomic force microscopy (DFM, Seiko Instruments Inc. SII: NanoNavi Station).

3. Results and discussion

Fig. 2a shows a XRD pattern of Cr_2O_3 film grown on R -cut sapphire substrate at 500 °C and Fig. 2b is the magnified pattern around $\text{Cr}_2\text{O}_3(1-102)$ Bragg reflection at various substrate temperatures from 300 °C to 600 °C. Bragg reflections from R -plane of Cr_2O_3 were clearly observed just below those of sapphire substrate in 2θ . The peak indicated by open-triangle was probably due to oxygen deficient of substrate. Any other peaks did not appear in XRD patterns. The lattice spacing was 0.363 nm similar to that of substrate. As shown in Fig. 2b, peak intensity was the highest at 500 °C with shoulder at right hand side of the peak indicated by arrow. Peaks became decreasing in intensity and broader in films grown 300 °C, 400 °C and 600 °C. Fig. 3 shows the full width at half maximum (FWHM) of rocking curve for $\text{Cr}_2\text{O}_3(1-102)$ as a function of substrate temper-

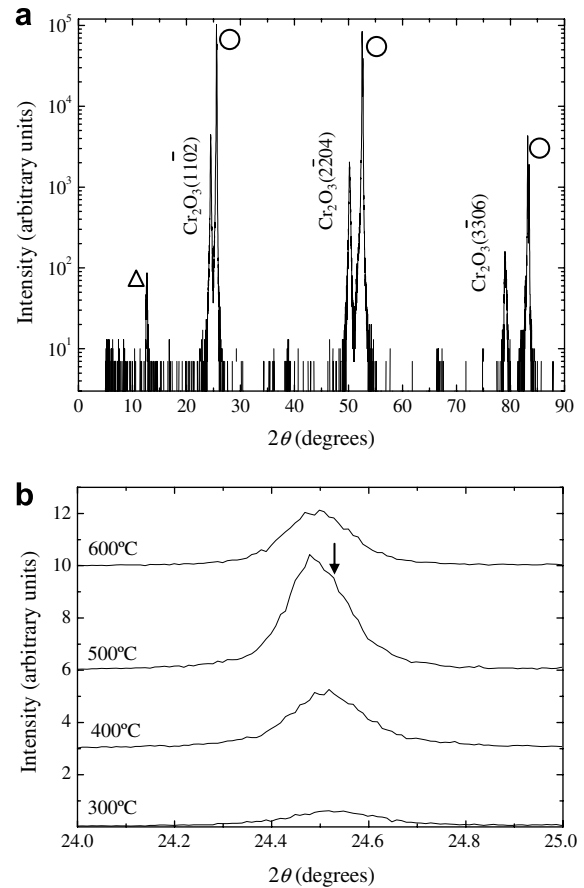


Fig. 2. XRD patterns of Cr_2O_3 film grown at (a) 500 °C on R -cut sapphire and (b) magnified images around $\text{Cr}_2\text{O}_3(1-102)$ Bragg reflection at various substrate temperature. Open circles and triangle are come from the substrate. Bragg reflections of Cr_2O_3 thin film were clearly observed.

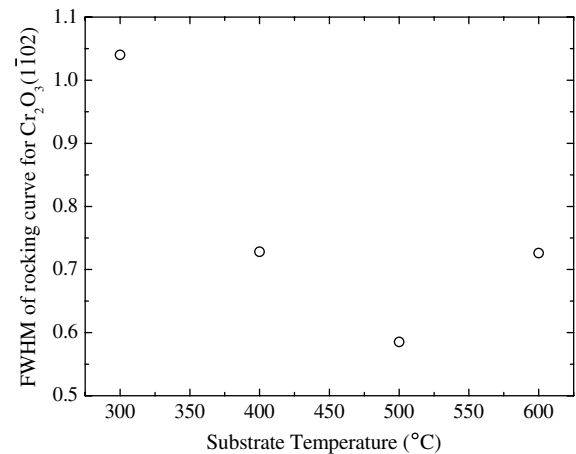


Fig. 3. The FWHM of rocking curve for $\text{Cr}_2\text{O}_3(1-102)$ as a function of substrate temperature. At 500 °C the sharpest peak was obtained.

ature. At 500 °C the rocking curve was 0.58° and the sharpest.

Generally the FWHM of Bragg reflections in 2θ – θ examination depends on a film thickness in particular less than 500 nm and a fluctuation of a lattice spacing. Since

the thickness of the grown film was constant approximately 190 nm in these experiments, the FWHM is a function of only the fluctuation of the $\text{Cr}_2\text{O}_3(1-102)$ lattice spacing. Considering the appearance of the shoulder at the right hand side of the $\text{Cr}_2\text{O}_3(1-102)$ Bragg reflection for the film grown at 500 °C, which was derived from the separation of the peak by $K_{\alpha 1}$ and $K_{\alpha 2}$ of different X-ray wave lengths, the fluctuation of the lattice spacing was reduced and then highly oriented film was obtained. Although a lattice mismatch is +4.01% along the $[11-20]$ direction and is +4.34% along the $[-1101]$ direction, an expected compressive stress in-plane is seemed to be released from the result of the same lattice spacing to the bulk value.

Figs. 4 and 5 show the surface images of the Cr_2O_3 films with the size of $2\ \mu\text{m} \times 2\ \mu\text{m}$ and line profiles of those images. In Table 1, grain sizes as a function of substrate

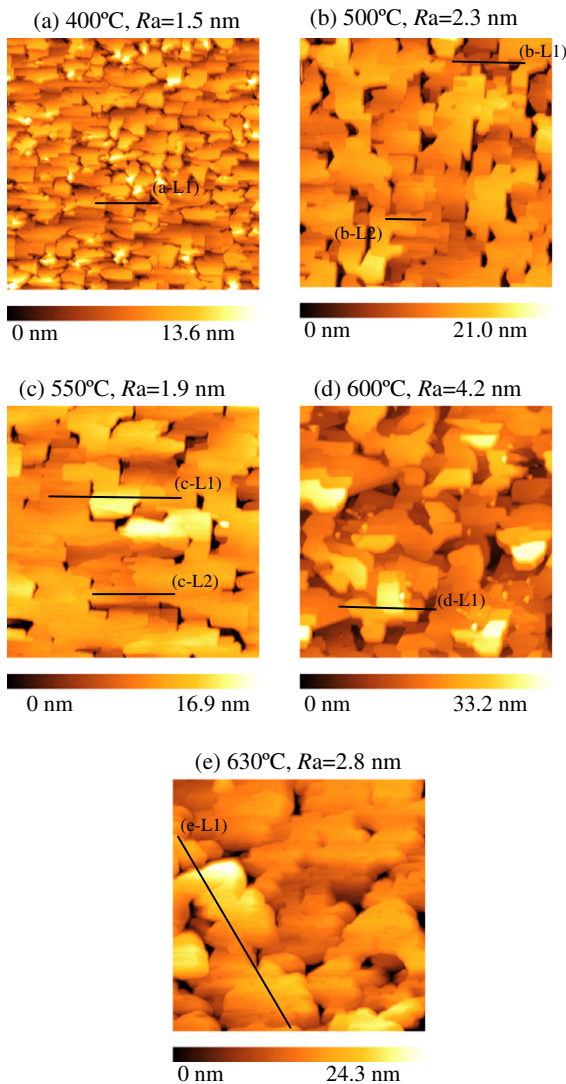


Fig. 4. Surface images with $2 \times 2\ \mu\text{m}^2$ of Cr_2O_3 thin films grown at (a) 400 °C, (b) 500 °C, (c) 550 °C, (d) 600 °C and (e) 630 °C. Scale bars were attached below each image. The film grown at (c) 550 °C showed the smoothest surface, the roughness R_a of which was 1.9 nm. Rectangular grains with the size of $200 \times 200\text{--}600\ \text{nm}^2$ coalesced throughout the surface except for the grains separated by deep grain boundaries.

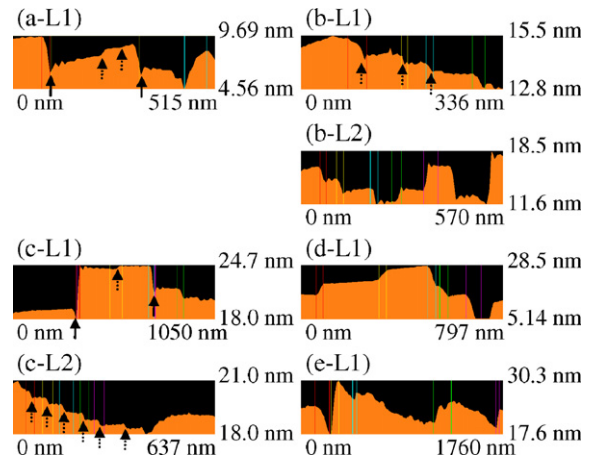


Fig. 5. Line profiles related to the index of the surface images of Fig. 4. Solid arrows indicate the difference in height at the grain boundary where coalescence did not take place. Dotted arrows indicate the steps composed of multiples of 1/3 unit cell along the $[1-102]$ direction inside one grain.

Table 1
Substrate temperature vs. grain size

Sub. temp. (°C)	Grain size (nm × nm)
400	100 × 100–200
500	100 × 100–500
550	200 × 200–600
600	400 × 400

temperature are summarized. Rectangular grains were mainly observed with the size of $100 \times 100\text{--}200\ \text{nm}^2$ at 400 °C in Fig. 4a. The difference in height between grains was approximately 3.5 nm indicated by solid arrows in Fig. 5a-L1. One grain contained 2 or 3 steps at the surface, indicated by dotted arrows, with the height of 0.3–0.9 nm, which was integer multiple of 1/3 unit cell along the $[1-102]$ direction, 0.363 nm. At 500 °C larger square grains with the size of $100 \times 100\text{--}500\ \text{nm}^2$ were observed and those grains were coalesced in Fig. 4b. In one grain the steps of 1–3 integer multiples of 1/3 unit cell was also observed as shown in Fig. 5b-L1 indicated by arrows. The grains growing from different nucleus sites, where coalescence did not occur, had a difference of 2–10 nm in height as shown in Fig. 5b-L2 and sometimes deep grain boundaries were formed. The deepest depth of the boundaries was 34 nm. At 550 °C as shown in Fig. 4c rectangular grains became larger and longer along a particular direction and the smoothest surface with the surface roughness R_a of 1.9 nm. Almost all of the grains coalesced except for the grains separated by deep grain boundaries as shown in Fig. 5c-L1 indicated by arrows. The density of deep boundaries decreased compared with that of Fig. 4b. As indicated by dotted arrows in Fig. 5c-L1 and c-L2, steps of 1/3 unit cell were clearly observed in one grain. Film growth looked like 2-dimensional island. At 600 °C although the largest grains were obtained, bunching steps, the value of which was approximately 5 nm, were observed as shown in Figs. 4d and 5d-L1.

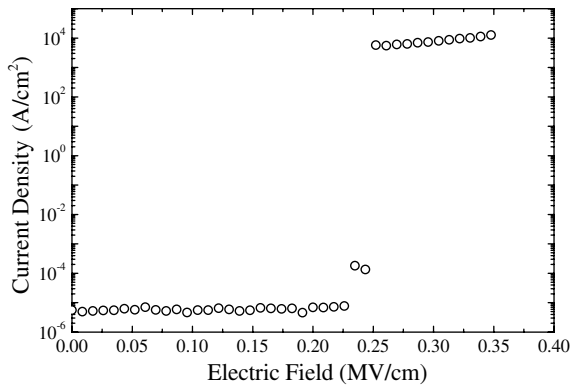


Fig. 6. I - V characteristic of $\text{Cr}_2\text{O}_3/\text{CeO}_2$ bilayered film on STO substrate. Below 0.24 MV/cm the film was insulating.

The surface smoothness was degraded down to the R_a of 4.2 nm due to the bunching steps. The surface of the terrace was so flat that even steps of $1/3$ unit cell did not appear. In addition, spherical grains were also observed with the size of $\varnothing 40 \mu\text{m}$. At 630°C as shown in Figs. 4e and 5e-L1 film 3-dimensionally grew without a regularity in grains.

As the substrate temperature is increased, the migration length increases and the density of nucleus sites as well as of grains decrease. At 400°C where coalescence did not take place, the surface was covered by many grains and boundaries with the height of 3.5 nm due to the short migration length. However at 500°C where start to coalesce but not to obtain sufficient migration length to be large grain, the deep grain boundary was expected to be introduced. As increasing substrate temperature up to 550°C , increased migration length led to larger grain and then the density of deep grain boundary was reduced. At 500 – 550°C , the terrace in one grain was composed of several steps of $1/3$ unit cell at most, indicating the 2-dimensional island growth. The unit of $-\text{O}-\text{Cr}-\text{O}-\text{Cr}-\text{O}-$, corresponding to the height of $1/3$ unit cell, stacks along the $[1-102]$ direction in Cr_2O_3 single crystal with rhombohedral structure. In the highly oriented Cr_2O_3 films, it is reasonable that the integer multiples of $1/3$ unit cell appear because of the repulsive force between O^{2-} ions at the interface of stacked $1/3$ unit cell. Above 600°C despite sufficient migration length to be large grain, Cr_2O_3 is expected to be decomposed due to deficient of oxygen, demonstrated by the results of XRD and the present of spherical grains.

Fig. 6 is a leakage current density as a function of electric field (I - V) of a bilayered film of $\text{Cr}_2\text{O}_3/\text{CeO}_2//$

STO(100) observed at room temperature. The thickness of Cr_2O_3 and CeO_2 was 220 nm and approximately 10 nm, respectively. The diameter of measurement area was $\varnothing 0.45 \text{ mm}$. From the XRD result Cr_2O_3 film was oriented along the c -direction normal to the substrate surface. Leakage current rapidly increased above 0.24 MV/cm indicating that the Cr_2O_3 film works as a ME material below the electric field.

We estimated the induced magnetic field tentatively with the obtained data. Assuming that the ME coefficient of Cr_2O_3 along the c -direction around 40 K α_{zz} is 10^{-4} (in CGS – gauss unit) and the demagnetizing field is neglected, induced magnetic field is estimated at 1.0 G [1–4]. For example, to obtain 0.5 mA by a shielding current, which is representative for base current in SFQ device, with $100 \mu\text{m}^2$ and 100 pH superconducting loop, 5 G is required. We expect to achieve such the value by optimizing the growth condition of CeO_2 for epitaxial growth of Cr_2O_3 on it.

4. Conclusion

We propose to apply the ME materials of single phase compounds to the SFQ device as the replacement of a base current and stabilization of I_c spread. The ME material generates induced magnetic field with electric field applied. As a representative ME material, Cr_2O_3 thin films were grown on R -cut sapphire and STO substrates in order to integrate with high- T_c superconductors. At 550°C , 0.26 Pa and a flow rate of $\text{Ar}:\text{O}_2 = 4:1$, highly oriented Cr_2O_3 thin films grew on sapphire substrate, the surface of which was composed of coalesced rectangular grains with the size of 200×200 – 600 nm^2 . The surface roughness R_a was 1.9 nm. Estimated induced magnetic field from the result of $\text{Cr}_2\text{O}_3/\text{CeO}_2//\text{STO}$ was 1.0 G around 40 K. To eliminate the induced magnetic flux, shielding current is expect to flow superconducting circuit, which is substituted for a base current of SFQ device by a current source.

References

- [1] K.K. Likharev, K. Semenov, IEEE Trans. Appl. Supercond. 1 (1991) 3.
- [2] M. Fiebig, J. Phys. D: Appl. Phys. 38 (2005) R123.
- [3] H. Wigelmann, A.G.M. Jansen, P. Wyder, J.P. Rivera, H. Schmid, Ferroelectrics 162 (1994) 141.
- [4] N. Iwata, K. Matsuo, N. Ootsuka, H. Yamamoto, Mat. Res. Soc. Symp. Proc. 811 (2004) 425.